Imperial College London

# Seismic reverse-time migration in viscoelastic media

*by*

Qiang Xu

Resource Geophysics Academy
Department of Earth Science and Engineering
Imperial College London

A dissertation submitted in fulfilment of the requirements for the degree of Doctor of Philosophy

November 2022

# Declaration of Originality

I hereby declare that, except where express reference is made to the work of others, the contents of this dissertation are original and have not been submitted in whole or in part for any other degree or qualification at this or any other university. This dissertation is my own work and contains nothing that is the result of collaboration with others, except as indicated in the text and acknowledgements.

Qiang Xu

November 2022

# Copyright Declaration



Qiang Xu

November 2022

# Acknowledgements

First and foremost, I would like to express my heartfelt gratitude to my PhD supervisor, Prof. Yanghua Wang, for his patient guidance and professional supervision. He introduced me to the world of geophysics and showed me the excitement of scientific research. His profound knowledge and diligence in scientific research have always inspired me during my PhD. Moreover, he is my eternal role model for positive attitude towards people and difficulties in life. I wholeheartedly wish him a fruitful working and health life. I would also like to thank Prof. Stephen Neethling and Dr Gareth Robert for their constructive comments during my PhD. In addition, I would also like to thank the reviewers and referees for their valuable suggestions during the review and viva.

I am grateful to the Resource Geophysics Academy for providing financial support for this study. I would also like to thank my colleagues in the RGA for fruitful discussions during my PhD. I would like to express my special thanks to Dr Jiashun Yao and Dr Zhencong Zhao. They are always patient and helpful when I encounter problems, which gives me hope and confidence on the path of research. My special thanks go to my friends, Yuxin Hao, Xiao Hu and Haoyu Zuo, who have accompanied me in happy and difficult times.

Many thanks to the Department of Earth Science and Engineering, Imperial College London. Imperial College has provided me with a wonderful platform to launch my career and think creatively. Imperial College has witnessed my development from a shy, innocent boy to a dependent, ambitious man. I sincerely wish that Imperial College maintains its diversity and produces more excellent researchers from whom the world can benefit.

Finally, I would like to thank my beloved parents. Their constant and unceasing love and support is always the greatest source of strength in my life.

# Abstract


Seismic images are key to exploration seismology. They help identify structures in the subsurface and locate potential reservoirs. However, seismic images suffer from the problem of low resolution caused by the viscoelasticity of the medium. The viscoelasticity of the media is caused by the combination of fractured solid rock and fluids, such as water, oil and gas. This viscoelasticity of the medium causes attenuation of seismic waves, which includes energy absorption and velocity dispersion. These two attenuation effects significantly change the seismic data, and thus the seismic imaging.

The aim of this thesis is to deepen the understanding of seismic wave propagation in attenuating media and to further investigate the method for high-resolution seismic imaging. My work, presented in this dissertation, comprises the following three parts.

First, the determination of the viscoelastic parameters in the generalised viscoelastic wave equation. The viscoelasticity of subsurface media is succinctly represented in the generalised wave equation by a fractional temporal derivative. This generalised viscoelastic wave equation is characterised by the viscoelastic parameter and the viscoelastic velocity, but these parameters are not well formulated and therefore unfavourable for seismic implementation. The causality and stability of the generalised wave equation are proved by deriving the rate-of-relaxation function. On this basis, the viscoelastic parameter is formulated based on the constant $Q$ model, and the viscoelastic velocity is formulated in terms of the reference velocity and the viscoelastic parameter. These two formulations adequately represent the viscoelastic effect in seismic wave propagation.

Second, the development of a fractional spatial derivatives wave equation with a spatial filter. This development aims to effectively and efficiently solve the generalised viscoelastic

wave equation with fractional temporal derivative, which is numerically challenging. I have transferred the fractional temporal derivative into fractional spatial derivatives, which can be solved using the pseudo-spectral implementation. However, this method is inaccurate in heterogeneous media. I introduced a spatial filter to correct the simulation error caused by the averaging in this implementation. The numerical test shows that the proposed spatial filter can significantly improve the accuracy of the seismic simulation and maintain high efficiency. Moreover, the proposed wave equation with fractional spatial derivatives is applied to compensate for the attenuation effects in reverse-time migration. This allows the dispersion correction and energy compensation to be performed simultaneously, which improves the resolution of the migration results.

Finally, the development of reverse-time migration using biaxial wavefield decomposition to reduce migration artefacts and further improve the resolution of seismic images. In reverse-time migration, the cross-correlation of unphysical waves leads to large artefacts. By decomposing the wavefield both horizontally and vertically, and selecting only the causal waves for cross-correlation, the artefacts are greatly reduced, and the delicate structures can be identified. This decomposition method is also suitable for reverse-time migration with attenuation compensation. The migration results show that the resolution of the final seismic image is significantly improved, compared to conventional reverse-time migration.

# Table of contents

# List of Figures

# List of Tables

# Chapter 1

# Background

## 1.1 Motivation

Seismic exploration is the main method of locating and exploring oil and gas reservoirs. Generally, seismic exploration includes three major steps, seismic data acquisition, processing, and interpretation. In the processing of the seismic data, migration is an essential method to generate the subsurface image based on the acquired data, and to clearly present the spatial patterns of subsurface structures. High-resolution seismic images are normally required for detailed descriptions of oil and gas reservoirs, and for the determination of the heterogeneities of the rocks, such as the variation of fluid content and porosity. Additionally, the quality of migration images directly influences the reliability and accuracy of the subsequent seismic interpretation. Therefore, the resolution and fidelity of migration images are of great importance in the seismic exploration industry. Although the development of new acquisition methods for high-resolution seismic data is important, significant benefits can be obtained by developing methods that can improve the resolution of the existing seismic dataset or the new dataset acquired by the existing systems. This thesis discusses one of the aspects of resolution enhancement, reverse time migration with attenuation compensation.

Viscoelasticity is an intrinsic property of earth media, which is due to the presence of fractured rocks, fluids, and gases. The viscoelasticity of earth media attracts a lot of research attention because this property is regarded as an indicator of hydrocarbons, such as potential oil and gas reservoirs, which provide crucial energy for the development of modern society. This property alters the phase and amplitude information of the seismic data. Specifically, the amplitude of the seismic waves decreases, and the original wavelet is modified, delayed, and stretched during the propagation. Thus, the recorded data shows weak amplitudes and broadened wavelet, leading to a low signal-to-noise ratio, considering the noise from the acquisition and production cannot be effectively removed. This low signal-to-noise ratio subsequently has a great impact on seismic images. Inaccurate and low-resolution seismic images will greatly hinder the seismic interpretation and subsequently harm the exploration. Therefore, considering that seismic attenuating effects significantly change seismic data, accurate seismic simulation in viscoelastic media is of great theoretical importance. Further, improving the quality of seismic migration images for attenuation zones is practically valuable, which greatly benefits seismic interpretation and subsequent production.

The ultimate purpose of reverse time migration with attenuation compensation is to improve the signal-to-noise ratio and enhance the resolution of the migration images. There are two aspects involved. First, improving the useful information of the migration image, by compensating the attenuation effects. Second, reducing the noise during the migration process. With the development of these two aspects, the resolution of the migration images can be improved.

## 1.2 The viscoelasticity and the fractional derivative

When seismic waves propagate through the viscoelastic media, there are two fundamental attenuation effects associated: energy absorption and velocity dispersion. Energy absorption means the seismic wave energy losses, or converts to heat, irreversibly, due to the intrinsic fraction of the media particles. This energy loss is frequency-dependent, which denotes that the energy dissipation of a high-frequency wave component is stronger than that of a low-frequency one. Velocity dispersion means that different frequency waves propagate at different phase velocities, that is, the high frequencies travel faster than the low frequencies, and the phase of the wavelet varies during propagation. Therefore, a proper stress-strain relation should be used to describe this frequency-dependent attenuation.

The stress-strain relation of viscoelastic media can be mathematically described in a form of a fractional time derivative, which can be generalised from the well-established theories. For an ideal elastic media, the well-known Hooke's law describes a linear relationship between stress and strain as

$$\sigma(t) = E\varepsilon(t), \tag{1.1}$$

where $\sigma(t)$ is the stress, $\varepsilon(t)$ is the strain and $E$ is Young's modulus. Eq. (1.1) can be viewed as the stress is related to the zero order of the time derivative of the strain. For an ideal viscous media, the Newtonian fluid law states that the stress is linearly related to the first-order time derivative of the strain as:

$$\sigma(t) = \eta \frac{\mathrm{d}\varepsilon(t)}{\mathrm{d}t}, \tag{1.2}$$

where $\eta$ is the viscosity coefficient. The viscoelasticity should behave in an intermediate state between the elasticity and the viscosity. Therefore, the stress-strain relation is generalised in a form of a fractional time derivative as,

$$\sigma(t) = E^{1-\beta}\eta^{\beta} \frac{\mathrm{d}^{\beta}\varepsilon(t)}{\mathrm{d}t^{\beta}}, \tag{1.3}$$

where $\beta$ is an interpolation coefficient between zero and one. The order of the fractional time derivative, $\beta$, decides the magnitude of the attenuation.

The fractional-time-derivative form of the stress-strain relation was first introduced by Caputo (1967). which introduced a causal creep function that is proportional to the time power. The creep function describes the variation of strain when a unit step of stress is applied, and this time-dependent property is consistent with the viscous materials. In the frequency domain, this creep function produces a complex modulus that is proportional to the fractional power of the frequency, which accurately describes the frequency dependency of the attenuation. This complex modulus is consistent with the observations that stiffness and damping properties of viscoelastic materials are often proportional to fractional powers of frequency. Subsequently, the relaxation function, which represents the stress that results from a unit step in strain, can be derived, and this relaxation function is inversely proportional to the time power, which demonstrates that the material relaxation vanished along with the increasing time. Additionally, the causal form of these two functions indicates the causality of the viscoelastic material as well, which is a basic requirement for stress-strain relations. The causality, the time-dependent damping mechanism, and the frequency dependency of the complex modulus, demonstrate the rationales of the fractional-time-derivative stress-strain relation.

Physically, the stress-strain relation in the form of a fractional time derivative can be viewed as a complex system of the combination of basic elements, which are springs, that represent an elastic response, and dashpots, that represent a viscous response. Some early attempts only consider the combination of a single spring and a dashpot, such as the Kelvin-Voigt model (Figure1.1a) and the Maxwell body (Figure 1.1b). However, the attenuation of seismic waves in sedimentary rocks, such as in a hydrocarbon reservoir, is not likely to be caused by a single mechanism, which can be demonstrated by the fact that the attenuation dispersion curve exhibits several peaks (Liu & Greenhalgh 2019). Additionally, the sedimentary rocks have an obvious heterogeneous distribution of characteristic length scales

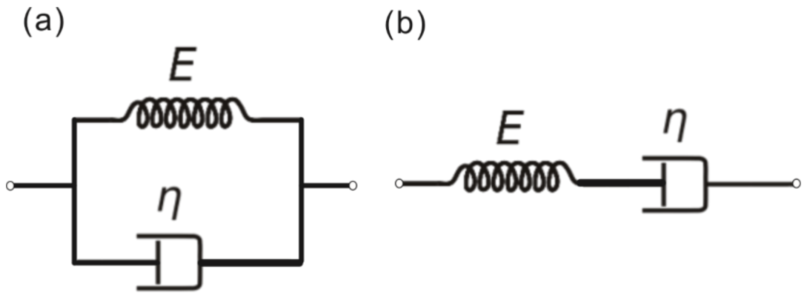


**Figure 1.1** The simple combination of the basic mechanical elements. (a) The Kelvin-Voigt Model; (b) the Maxwell Model. "$E$" represent an elastic spring and "$\eta$" represent a viscous dashpot. These models cannot properly represent the complex relaxation mechanism in fractured rock attenuation.

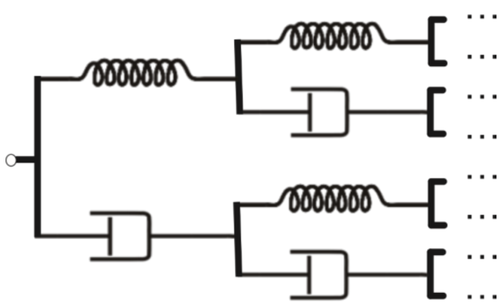

**Figure 1.2** One of the fractional models proposed by Xing & Zhu (2018). The fractional models can better describe the frequency-dependency of the relaxation mechanism.

that result in broader attenuation curves, even when only a single mechanism is considered, such as only the porous flow mechanism or patchy saturation mechanism. These complex behaviours cannot be represented by a single combination of the basic mechanical elements. Compared with the simple combination of the basic elements, this fractional-derivative system can be regarded as a complex combination of the basic mechanical elements. For example, Xing & Zhu (2018) introduced a fractal mechanical network (Figure 1.2) to describe rheological mechanisms and further proposed a corresponding fractional derivative wave equation. Thus, the fractional-derivative form of stress-strain relation can better describe the complex mechanisms of the rocks and present the reasonable frequency dependency of the attenuation.

Furthermore, the fractional-time-derivative stress-strain relation can produce an explicit form of the quality factor, which is a key variable to quantify attenuation. A detailed demonstration of the quality factor is introduced in the next section. For the fractional time derivative, its order represents the viscosity of the viscoelastic media, i.e., the attenuation magnitude, and this fractional order is a monotonic function of the quality factor. This explicit mapping relation between the fractional order and the quality factor leads to the convenience to evaluate the viscosity of the media, further allowing for the subsequent applications, such as seismic simulation, inverse $Q$ filtering, or attenuation compensation migration.

It should be noted that the fractional order and the inverse of the quality factor, $Q^{-1}$, which usually represents the magnitude of the attenuation, are not strictly linearly related, because the quality factor is theoretically frequency-dependent, while the fractional order is frequency-independent. The fractional order is more sensitive to the same quality factor perturbation in strong attenuative media than in weak attenuative media. This conclusion is also consistent with the field data measurements. On the other hand, the fractional order can be determined by the quality factor, which can be obtained by $Q$ analysis or laboratory measurements. Therefore, with an accurate quality factor model, the fractional-time-derivative stress-strain relation can represent the attenuation properties in viscoelastic media reasonably.

To briefly conclude, the fractional-time-derivative stress-strain relation can describe the frequency-dependent attenuation and produce an explicit quality factor. Therefore, the fractional time derivative is widely adopted in various viscoelastic models for theoretical analysis and numerical simulation, such as the constant $Q$ model (Kjartansson, 1979), the Strick-Azimi model (Y. Wang 2008), and the generalized viscoelastic model (Y. Wang, 2016).

Combining the fractional-time-derivative stress-strain relation, the strain-velocity-displacement equation, and Newton's second law, the viscoelastic wave equation may be derived in a form of a fractional time derivative accordingly. This viscoelastic wave equation can describe the seismic wave propagation in viscoelastic media accurately.

## 1.3 The quality factor

The viscoelasticity of the media causes the disturbance of the wavelets. For a plane sinusoidal scalar wave travelling through viscoelastic media, the attenuation is often quantitively described by quality factor $Q$, defined as

$$Q = 2\pi \frac{E_{\mathrm{p}}}{E_{\mathrm{d}}} \tag{1.4}$$

where $E_{\mathrm{p}}$ denotes the preserved wave energy and $E_{\mathrm{d}}$ denotes the dissipated energy in a single cycle of wave propagation. Therefore, its reciprocal, $Q^{-1}$, represents the magnitude of the attenuation. The $Q^{-1}$ factor may also be defined equivalently as the tangent of the stress and strain phase lag, which is related to the modulus.

There are two associated attenuation effects due to the quality factor, the energy absorption and the frequency dispersion. The energy absorption is measured by the attenuation coefficient, which shows a power discrepancy of the quality factor in general. Some laboratory experiments and field data measurements demonstrate an approximate linear dependency of the attenuation and quality factor. Considering this linear relation, the attenuation coefficient can be determined directly by the wavelength (Y. Wang 2008b):

$$\alpha = \frac{20\pi}{(\ln 10) Q} \quad (\mathrm{dB}/\lambda) \tag{1.5}$$

where $\alpha$ is the attenuation coefficient, $\lambda$ is the wavelength. Equation (1.5) demonstrates that the attenuation coefficient is approximately $27.3Q^{-1}$ per wavelength, which validates the frequency dependency of the attenuation.

The frequency dispersion is normally more obvious at high record times with deep reflectors, where there is an obvious inconsistency between the synthetic seismic trace and recorded data. The frequency dispersion is represented normally by the phase velocity, which physically means the velocity that the phase of a specific frequency component is transmitted at. In the viscoelastic media, the high-frequency components have larger phase velocities than the low frequencies, leading to the deformation and delay of the wavelet. The phase velocity is also related to the quality factor, as in strong attenuative media, where $Q$ is small, the variation in the targeted frequency band is more significant than in the weak attenuative media.

The attenuation and the dispersion should be present simultaneously, according to the principle of causality (Aki & Richards 1980). In other words, the dispersion must accompany absorption. The dispersion (phase velocity) and absorption (attenuation coefficient) should have an Hilbert transform relationship, which is referred as the Kramers-Kronig relation (Futterman 1962):

$$\frac{\omega}{v(\omega)} - \frac{\omega}{v_\infty} = -\mathscr{H}\left(\alpha(\omega)\right), \tag{1.6}$$

where $\mathscr{H}(\cdot)$ denotes the Hilbert transform, and $v_\infty$ is the unrelaxed velocity. This theoretical relation agrees well with the experimental data (Y. Wang 2008b), and this relation is often used to verified the viscoelastic models.

In the aspect of rock physics, this attenuation is mainly due to inner energy loss, including friction, fluid movement, and viscosity relaxation. There are several mechanisms for this energy loss, such as Biot theory, Gassmann theory, and patchy theory (Mavko *et al*. 1998). Generally, these theories both consider the fluid in rocks to have viscous and inertial properties, and the fluid and rock particles have different-phase movement when seismic waves propagate through the media, and this different-phase movement leads to dispersion and attenuation. Simultaneously, when seismic waves propagate in the fractured rock, the saturability and porosity vary, causing the redistribution of the fluid. This variation and the fluid redistribution also cause different attenuation property of the media.

Thus, due to the fact that the quality factor is closely dependent on the physical properties of the media, such as porosity, fluid viscosity, and stress state, it already has a number of applications in the exploration geophysics. For example, the variation of $Q$ can reflect the fluid property change, which can be used to evaluate the potential state for the fluid-filled rocks. Additionally, the potential fluid presence can be estimated by the quality factor, due to the quality factor of saturated rocks is much smaller than that of dry solid rocks, which is used to located the oil and gas reservoirs. In this thesis, I consider the attenuation property of the media as a whole while ignoring the detailed attenuation mechanism of the rock, to better understand the seismic wave propagation in viscoelastic media.

For subsurface media, the propagation of different frequency waves is related to the different mechanisms of internal fluid flow, and attenuation is usually frequency-dependent. Therefore, the quality factor is also frequency dependent, especially for the broad frequency band (e.g. Sams *et al*. 1997, Molyneux & Schmitt 2000, Adam *et al*. 2009, Borgomano *et al*. 2017). The mechanism of this frequency dependency can be described as when the solid skeleton is compressed by seismic waves, the viscous force occurs in the pores, and it diminishes exponentially along with the distance to the solid-fluid interfaces. This viscous force allows the different movement of the rock and fluid, and further leads to attenuation. And this viscous force is related to frequency. When the frequency of seismic waves is low, the viscous-force affected area is small compared with the pores' radius, leading to small attenuation and dispersion.

In seismic application, a small dissipation assumption is normally adopted, which is often referred as the weak attenuation assumption. This assumption states that the quality factor is normally large, and $Q^{-1} \ll 1$ in geophysical application. This small dissipation assumption is valid under the most condition of the interest in geophysics (Futterman 1962; Y. Wang 2008b). Under this assumption, the relation between the quality factor, the attenuation coefficient and phase velocity can be approximated as

$$Q(\omega) \approx \frac{|\omega|}{2\alpha(\omega)v(\omega)}, \tag{1.7}$$

where the absolute value is to keep a positive quality factor. Eq. (1.7) can be used to estimate the frequency-dependent quality factor.

However, some laboratory and field measurements prove that the earth materials exhibit a nearly constant $Q$ behaviour over a limited frequency band (e.g., McDonal *et al.* 1958), which means the quality factor $Q$ can be regarded as a frequency-independent variable. This frequency-independent $Q$ model is rational for the seismic application, because the frequency band of the seismic waves is relatively low and limited, usually no more than 500 Hz, and the quality factor $Q$ in the targeted frequency band is generally stable. In this thesis, only this frequency-independent $Q$ is considered because it has been proven that this frequency-independent $Q$ is practically useful in seismological modelling and imaging applications.

It should be noted that the quality factor $Q$ is also related to the wave property, which means that different waves will have different quality factors when propagating through the same viscoelastic media. For example, the quality factor of the S wave is normally less than its P-wave counterpart. In this thesis, I only consider the acoustic case, as it is very common in marine seismic surveys, where only the pressure can be propagated and the shear stress cannot be conveyed. Theoretically, the acoustic wavefield is scalar, which can be viewed as the basis to investigate the seismic wave propagation law. Additionally, the media is assumed to be isotropic, which is also a common simplification. With a deep understanding of the wave propagation law in attenuative acoustic and isotropic media, it can benefit the future expansion of anisotropic and vector wavefields. I only consider the intrinsic $Q$, instead of scattering $Q$, as the scattering waves are not considered.

The discussion in this thesis is model-based, which assumes that the quality factor model is accurate. The establishment of the accurate $Q$ model is a prerequisite of seismic simulation and subsequent imaging.

## 1.4 Overview

This thesis aims to develop the viscoelastic theory for seismic wave propagation in attenuating media and to further investigate the method for high-resolution seismic migration imaging. This thesis is organized as follows:

Chapter 2 gives a literature review regarding this thesis and demonstrates the current research gaps. Firstly, the development of viscoelastic theories is reviewed, which leads to the conclusion that the generalised viscoelastic wave equation is accurate to represent viscoelasticity. Then, considering the implementation, the numerical methods are reviewed to introduce the issue that the original generalised wave equation is unsuitable for seismic simulation. Also, the subsequent techniques for attenuation compensation in reverse-time migration are reviewed. Finally, to improve the signal-to-noise ratio of migration images, the artefacts elimination methods are briefly introduced, which leads to the validity and the superiority of wavefield decomposition in reverse-time migration.

Chapter 3 focuses on the determination of physical parameters in the generalised viscoelastic wave equation. This generalised viscoelastic wave equation is characterized by the viscoelastic parameter and the viscoelastic velocity, but these parameters are not well formulated and therefore unfavourable for seismic implementation. Here, the generalised wave equation is proven to be causal and stable by deriving the explicit form of the rate-of-relaxation function. Causality and stability are two necessary conditions for the applicability of the wave equation in seismic simulations. On this basis, the physical parameters are established for the application of the generalised wave equation. First, the relationship between the viscoelastic parameter and the well-developed constant $Q$ model is formulated. The proposed frequency-independent relationship agrees with the theoretical solution and fits the field data. Then, the viscoelastic velocity in terms of the reference velocity and the viscoelastic parameter is formulated. These two formulations adequately represent the viscoelastic effect in seismic wave propagation and lead to an improvement in the accuracy of the numerical simulation of the generalised viscoelastic wave equation.

Chapter 4 aims to investigate the method for efficiently and accurately simulating the generalised viscoelastic wave equation. The viscoelasticity can be represented concisely by a wave equation in the form of a fractional temporal derivative, which is numerically inefficient. An efficient implementation strategy for seismic waves propagated through a heterogeneous viscoelastic model is proposed in this chapter. The fractional temporal derivative is transferred to fractional spatial derivatives, and is implemented through fast Fourier transforms, for improving computational efficiency. However, the FFT implementation is not rigorously applicable to the heterogeneous model. Thus, a spatial-position-dependent filter is introduced. This spatial filter corrects the error that is caused by the assumption of non-heterogeneity in the FFT implementation. This filtered wave equation represents the viscoelastic effects appropriately in seismic wave propagation, leading to the improvement of the accuracy of numerical simulation. With an efficient and effective solver for the viscoelastic wave equation, the proposed wave equation is applied to compensate for the viscoelastic effects in attenuating media. The phase correction and the energy compensation can be implemented separately based on the proposed decoupled wave equation. Numerical results demonstrate that this compensation in reverse-time migration greatly improves the signal-to-noise ratio and enhance the resolution of migration images.

Chapter 5 seeks to improve the signal-to-noise ratio in the reverse-time migration by reducing the artefacts, which is due to the cross-correlation of irrelevant waves. Only performing the wavefield decomposition along the vertical axis is not sufficient to eliminate the artefacts. Thus, the biaxial wavefield decomposition based on the analytical wavefield via the Hilbert transform is introduced, which decomposes seismic wavefields in both lateral and vertical directions. After decomposition, the up-going source wavefield and down-going receiver wavefield are discarded to eliminate the strong shallow artefact, and the remaining four cross-correlation terms contribute to imaging the flat layers and the tilted interfaces separately. The remaining artefacts can be easily identified and reduced as the four terms are decoupled. Also, since the tilted interfaces are separated from the nearly flat layers, the resolution can be improved by adjusting the weights of the four terms. This Hilbert transform method is proven to be suitable for the viscoelastic wave equation with fractional spatial derivatives. Thus, this biaxial wavefield decomposition method is applicable to attenuation compensation reverse time migration. Numerical experiments demonstrate that the decomposed four images a can assist in the better presentation of the complex subsurface structure, and the resolution of the final migration images are greatly improved, compared with the conventional methods.

Chapter 6 presents an integrated field data example of previous methods. The data processing method is first introduced. The dataset is interpolated for a finer time interval and transferred to 2D, and the migration wavelet is extracted. Subsequently, the reverse-time migration with the biaxial wavefield decomposition is applied to the processed dataset. This field data example demonstrates the proposed method is suitable for practical application.

Chapter 7 summarizes the main conclusion of this work and provides some relevant future work. In future work, the proposed viscoelastic theory is expanded to the 2D vector wavefield and anisotropic media, although part of the content requires further verification. Finally, some suggestions are provided regarding the potential future work.

# Chapter 2

# Literature review

In the previous chapter, the background of this thesis is presented. The main objective of this thesis is to deepen the understanding of seismic wave propagation in attenuating media and to further investigate the method for high-resolution seismic imaging. This chapter briefly reviews the related studies, including the development of mathematical viscoelastic models, the numerical solvers of the equation, and the artefacts elimination methods for reverse-time migration. Also, the relevant research gaps are identified, and the main contributions of the thesis are outlined.

## 2.1 The physical and mathematical description of viscoelasticity

The viscoelasticity is an intrinsic property of the subsurface media, which brings energy absorption and frequency dispersion of seismic waves. The viscoelasticity is mathematically described by the quality factor $Q$, which is defined as $2\pi$ multiplied by the ratio of the preserved wave energy to the dissipated energy in a single cycle of wave propagation. Theoretically, for the broad frequency band, the quality factor should be frequency dependent, (e.g. Sams *et al*. 1997, Molyneux & Schmitt 2000, Adam *et al*. 2009, Borgomano *et al*. 2017). However, some laboratory and field measurements prove that the earth materials exhibit a nearly constant $Q$ behaviour over a limited frequency band (e.g., McDonal *et al.* 1958), which demonstrates that the quality factor $Q$ can be regarded as frequency-independent in seismic applications, due to the fact that the seismic frequency band is relatively low and limited. This frequency-independent $Q$ significantly reduced the difficulty of evaluating the seismic attenuation, and it fits well with the field measurements. Therefore, it is widely used in seismic simulation and subsequent imaging process.

The quality factor $Q$ is naturally characterized by introducing the complex velocity in the frequency domain (Aki & Richards 1980). The quality factor may be determined by the ratio of the real and imaginary parts of the complex modulus as

$$Q^{-1} = \frac{\tilde{M}_{\mathrm{Im}}(\omega)}{\tilde{M}_{\mathrm{Re}}(\omega)} \tag{2.1}$$

where $\tilde{M}$ is the complex modulus, the subscripts 'Re' and 'Im' denotes the real and imaginary parts, and $\omega$ is the angular frequency. The complex modulus is the operator between the stress and strain in the frequency domain. In the time domain, the stress-strain relation in the viscoelastic wave equation is represented by a convolution with the kernel of the rate-of-relaxation function. This convolution often requires the storage of the entire history of the previous wavefields, which is numerically challenging, especially for large scale or 3D problems. A number of studies have attempted to investigate the time-domain methods, and the memory problem has been alleviated to various extents. The state-of-the-art techniques can be categorized into two major groups as follows.

One group attempts to use the combination of the spring (elasticity) and dashpots (viscosity) to physically describe the viscoelastic behaviour of subsurface materials, such as the Maxwell model, the Kelvin-Voigt model, and the standard linear solid (SLS) model (Zener 1948). Although a single mechanical element presents frequency-dependent attenuation, a distribution with different relaxation parameters and a combination of different patterns may approximately describe the frequency-independent quality factor within a limited frequency band (H.P. Liu *et* *al.* 1976). However, these simple models cannot describe the complex mechanism inside of the fractured rocks, such as the uneven distribution of the cracks and fluid. Based on this idea, some generalised models are proposed, such as the generalised standard linear solid (GSLS) and the generalised Maxwell body (GMB) (Moczo 2005). They exhibit exponential relaxation functions, which may alleviate the computational issue by introducing the memory variables, which are normally combinations of the previous states (e.g., Carcione, 2014; Emmerich & Korn, 1987; Robertsson *et al*., 1994). Nonetheless, the memory variables require additional computational memory and time (Zhu *et al.* 2013), especially for 3D problems. Also, the quality factor $Q$ is implicitly expressed by a series of relaxation parameters, which makes it practically difficult to inverse problems (Fichtner & van Driel 2014).

Another group of methods is based on mathematical derivation to capture the analytical frequency-independent $Q$ behaviour. For a purely elastic media, there is a linear relationship between stress and strain (Hooke's law), and for an ideal viscous media, the stress is linearly related to the first-order time derivative of the strain (the Newtonian fluid law). The viscoelasticity should behave in an intermediate state between the elasticity and the viscosity. Thus, the fractional temporal derivative of the strain was introduced to represent this viscoelasticity (Caputo 1967). Based on this, Kjartansson (1979) derived a power-law relaxation function and proposed a frequency-independent $Q$ model, known as the constant $Q$ model. This constant $Q$ model was proved to agree well with the field and laboratory attenuation coefficient, thus widely used in practical applications. This theory was soon expanded to wave propagation in viscoelastic (Carcione 2009) and viscoelastic-anisotropic media (Zhu 2017). However, this constant $Q$ model exhibits an unrealistic phase velocity, that the phase velocity of the low-frequency components, where most of the seismic waves are concentrated, is significantly less than the high-frequency components, and the phase velocity for the zero frequency, i.e., direct current component, is zero.

Y. Wang (2016) proposed a more realistic model, which demonstrates that the subsurface media should be a mixture of elasticity and viscoelasticity, so it is named the generalised viscoelasticity model. This generalised model unifies the pure elasticity (Hooke's law) and viscoelasticity (a fractional temporal derivative) into a compact form and follows the basic power-law attenuation. Compared with Kjartansson's constant $Q$ model (Kjartansson 1979) this generalised model not only has a similar linear-like attenuation coefficient, but more importantly, has a more realistic phase velocity at low frequency, even for the zero-frequency component. Following this, Y. Wang (2019) proposed a frequency-independent $Q$ expression for better application in the narrow and low frequency band in reflection seismology, based on the small dissipation assumption. This model is newly developed, and some key parameters are not determined yet. Thus, this generalised model has not been successfully applied to seismic simulation and imaging. However, its attractive traits draw more and more attention. Thus, in this study, I focus on the development of this generalised model for seismic simulation and migration.

## 2.2 Seismic simulation in attenuating media

The generalised viscoelastic model describes viscoelasticity of the subsurface media appropriately, but the fractional time derivative is numerically challenging in practical application. Straightforwardly, the fractional time derivative can be evaluated in the frequency domain, where it can be transferred as the power of the angular frequency (e.g., Operto *et al.* 2007). However, this method is equivalent to solving numerous Helmholtz equations, which are computationally formidable, especially in 3D cases. Therefore, the frequency domain solver is no longer favourable in practical application.

In the time domain, the fractional temporal derivative is often solved by Grünwald-Letnikov expansion, which is a linear combination of the previous states with the gamma function as the coefficient. However, this Grünwald-Letnikov approximation still requires substantial memory space to store the wavefield history, even if it is partially truncated. An alternative solution is to transfer the fractional temporal derivative to an infinite integral, and approximated by Laguerre quadrature (Lu & Hanyga 2004). Even though this method satisfies the ordinary differential equations, it still requires considerable additional computational resources.

The large computational memory and low-efficiency issues considerably hinder the wave equation with a fractional temporal derivative from practical applications. For example, reverse-time migration (RTM) images are generally based on the superposition of multi-shot migration images, and every single-shot migration is highly dependent on the simulated seismic wavefields of thousands of time steps. If simulating a single-step wavefield requires tremendous computational resources, it would be almost impractical to generate multi-shot migration images, especially for large geological models or 3D problems. Therefore, it is crucial to improve the efficiency of solving the fractional temporal derivative.

This numerical problem for solving the fractional temporal derivative may be solved by transferring it to fractional spatial derivatives, or fractional Laplacian operators (W. Chen & Holm 2004, J. M. Carcione 2010). The fractional spatial derivatives can be efficiently solved by the pseudo-spectral method in the wavenumber domain as

$$(-\nabla^2)^{\beta/2} u(\mathbf{x}) = \mathcal{F}_{\mathrm{x}}^{-1}\left\{k^{\beta}\mathcal{F}_{\mathrm{x}}[u(\mathbf{x})]\right\}, \tag{2.2}$$

where $\beta$ is a fractional order between zero and one, $\mathcal{F}_{\mathrm{x}}$ is the Fourier transform with respect to vector **x**, $\mathcal{F}_{\mathrm{x}}^{-1}$ is the inverse of $\mathcal{F}_{\mathrm{x}}$, and $k$ is the angular wavenumber. In this way, the fractional derivatives may be calculated only based on the current wavefield, and storing the entire wavefield history is no longer necessary. Based on this transformation, Zhu & Harris (2014) derived the constant-$Q$ wave equation with two fractional spatial derivatives. It proved that this wave equation with fractional spatial derivatives owns great accuracy with the original constant-$Q$ wave equation with a fractional time derivative. Additionally, the two fractional terms in this wave equation represent the energy absorption and velocity dispersion, separately. Decoupling the attenuation effects makes it possible to analyse these two effects separately and in turn, accurately compensate for the attenuation in the imaging process, such as reverse-time migration (Zhu 2014).

The remaining problem for the fractional spatial derivatives is to calculate them in the heterogeneous media where the order of the fractional derivatives is a spatial-dependent variable. The order of the fractional derivative is often a function of the viscous parameters, which is related to the quality factor $Q$. It is admitted that the accurate $Q$ value distribution is not easy to estimate in practice, as it is influenced by not only the media itself, but also its physical conditions, such as filling materials, stress state, or even temperature (Ning 2016). Nevertheless, there are many empirical conclusions that can be used to estimate the $Q$ value based on the depth, velocity, or media materials (e.g. Y. Wang 2004). The spatially varied $Q$ model leads to the varied-order fractional spatial derivatives. However, these varied-order derivatives cannot be directly solved by the pseudo-spectral method, theoretically, as it requires a constant order to implement the Fourier transform. As in Eq. (2.2), if the fractional order is spatial dependent $\beta(\mathbf{x})$, it contains a mix-domain operator $k^{\beta(\mathbf{x})}$, and the Fourier transform cannot be implemented directly.

A common way to approximately evaluate the varied-order fractional derivative is to use the average-valued order of the model to replace the varied order (Zhu & Harris 2014), with the assumption that the order of the derivatives varied little and smoothly, i.e. the media with little $Q$ variation. This method has shown great applicability in weak attenuative areas, as the attenuation is not sensitive for large $Q$ cases. Nonetheless, this averaging scheme causes simulation errors. This simulation error can be significant in strong attenuation areas, for example, the presence of oil or gas reservoirs, which are normally the areas of interest in geophysical applications.

Therefore, the investigation of the seismic wavefield simulation in inhomogeneous $Q$ media drew more and more research attention. A straightforward way is that, based on the locality principle, the wavefield of every time step can be obtained by interpolation of a number of solutions with every single constant $Q$ value in the model (Zhu & Harris 2014). Although this scheme is relatively accurate, the computational time is proportional to the model size, which would be computationally inefficient for large complex models or 3D cases. Further, some studies show improved accuracy by transferring the spatial-varying order fractional wave equation to a constant order wave equation via Taylor expansion or a polynomial approximation (Chen *et al.*2016; Xing & Zhu 2019). These constant order wave equations can be evaluated via spatial pseudo-spectral method directly without the averaging assumption. There are also some other attempts to calculate the fractional spatial derivatives without the FFT implementation. For example, the Hermite distributed approximation is applied to transfer the spatial-varying fractional spatial derivative to an integral of the fractional derivative of the delta function, and this fractional derivative can be solved locally (Yao *et al*. 2017). Although these works improve the accuracy of the varied-order fractional spatial derivatives, the computational efficiency is reduced during the process. This inefficiency will greatly hinder the development of reverse-time migration as numerous seismic simulations are involved during the process. Taking Xing & Zhu (2019) as an example, the resultant polynomial-approximation wave equation includes six fractional Laplacian operators, which at least triples the computational time, if compared with the original two-operator equation. Therefore, it is still necessary to investigate efficient simulation methods for seismic wave propagation in viscoelastic media. In this thesis, a strategy is proposed that maintains the efficiency of the original pseudo-spectral method but improves the accuracy in the heterogeneous *Q* model. This efficient strategy will benefit the implementation of reverse-time migration.

Due to the viscoelastic effect of earth media, conventional migration images suffer from weakened amplitude and distorted phase. Thus, how to appropriately compensate for the viscoelastic effects is an important topic. For any ray-path method, it is extremely difficult to determine correct weighting functions along the ray path, and they are only applicable to simple geological models (Ning 2016). Considering the frequency-dependency of the attenuation, it is more reasonable to compensate for the attenuation in the implementation of the wave equation. Early studies replaced the real-valued velocity with complex, frequency-dependent velocity in the one-way wave equation, and then compensate for the attenuation effects (Mittet *et al.* 1995, Y. Wang & Guo 2004a). Among those studies, inverse *Q* filtering migration (Y. Wang 2008b) is shown to be an effective method, which proposes two operators for compensation: the unconditionally stable phase operator, and the stabilized amplitude operator. However, this method is derived based on the 1D velocity model, and is not accurate enough for complicated geological models.

In order to better illuminate the subsurface structures, compensation of the attenuation in reverse-time migration (RTM), which is based on a two-way wave equation, is proven to be more theoretically accurate and effective (Dutta & Schuster 2014, Sun *et al.* 2015). By means of the decoupled viscoelastic wave equation, the accurate compensation in RTM is implemented, which enables the amplitude and phase to be separately compensated (Zhu 2014). Although the phase compensator is unconditionally stable, the amplitude compensation exhibits numerical instability, as it is an exponential amplification. Such numerical instability is original from the artificial compensation of the ambient noise, especially the high frequency noise in seismic data, or the machine errors relative to the precision. Thus, appropriate stabilization should be incorporated in the frequency or wavenumber domain, to avoid this frequency/wavenumber dependent instability. Straightforwardly, a low-pass filter can be applied, and the cur-off frequency can be determined by the noise level and the targeted frequency band of seismic data. Recently, some other strategies are investigated to solve this numerical instability, and some of them are directly referred to the inverse *Q* stabilization techniques. For example, Y. Wang *et al*. (2018) proposed an adaptive stabilization strategy, which incorporate the time variance and *Q* dependence, and it shows superiority over the conventional low-pass filtering.

The attenuation compensation is shown be effective for correcting the phase and compensating for the amplitude in reverse-time migration, thus improving the signal-to-noise ratio, and enhancing the resolution of the migration images.

## 2.3 Artefact elimination in reverse-time migration

The attenuation compensation enhances the useful seismic signals of the migration results. To improve the signal-to-noise ratio, the noise, which is also referred as the artefact, should be reduced. RTM results are severely deteriorated by the artefact issue. Another important aspect of this thesis to improve the resolution of the migration results is the elimination of the artefacts.

The migration artefact is caused by the cross-correlation of the unphysical waves, because RTM uses a two-way wave equation to simulate both source and receiver wavefields, and the cross-correlation between the irrelevant directional waves causes the undesirable high-amplitude, low-spatial frequency false images. Especially for fine layers, faults, and small-scale structures where the seismic reflection is relatively weak or complex, the images of these structures are greatly contaminated by the migration artefacts. Therefore, in recent years, reducing artefacts and improving the resolution of the migration images have drawn more attention.

Theoretically, there are three approaches to eliminate the artefacts: direct filtering the dataset, muting unphysical waves during propagation, and processing the final migration images. There are few studies focusing on filtering the dataset, as it is difficult to distinguish the useful data with the noise. Also, the useful data will again cause the artefacts in final images due to the two-way propagation. For processing the final migration images, a straightforward and practical approach is to apply Laplacian filters to the final image. However, this approach is only an image processing technique, and cannot eliminate the migration noise, and it damages the true image of structures (Guitton *et al.* 2007). Nowadays, the Laplacian filter often applied as a supplement.

Therefore, more and more studies are focusing on reducing the artefacts during the wave propagation and migration process. The directional damping method is introduced to suppress the inner reflection, and further reduce the low-frequency noise (Fletcher *et al.* 2006). It is proposed to mute the far angle waves by using the angle domain common gathers, to achieve the removal of the artefacts (Zhang & Sun 2009). These early attempts did remove some artefacts; however, their results were limited.

Performing the wavefield decomposition during simulating the source and receiver wavefield is a practical way to reduce the artefacts, as only the selected physical waves are used in the imaging condition. The cross correlation of the unphysical waves produces the artefacts. The commonest method is up-/ down-going wave decomposition, which only retains the down-going source wavefield and up-going receiver wavefield in the cross-correlation. Specifically, the cross-correlation imaging condition can be mathematically partitioned in a discrete form after the up-/ down- decomposition as:

$$I = \sum_t S_d R_d + S_d R_u + S_u R_d + S_u R_u \,, \tag{2.3}$$

where $I$ is the migration image, $S$ and $R$ represent the source and receiver wavefield and subscript '*d*, *u*' denote the down-going and up-going, respectively. In Eq. (2.3), $S_d R_d$ and $S_u R_u$

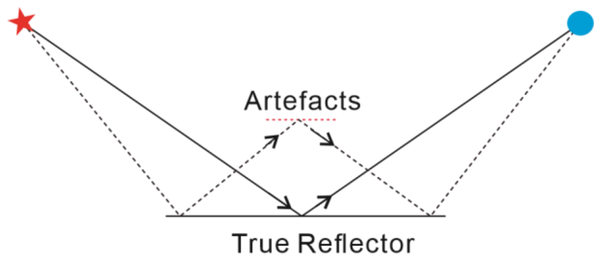


**Figure 2.2** The upward-folded ray-path artefacts in reverse time migration. The red star and the blue circle represent the source and the receiver, respectively. The black solid line is the true ray-path which the black dotted line is the artefacts ray-path. The red dotted line denotes the upfolded artefacts of the true reflector. The cross-correlation of the up-going source and down-going receiver wavefields causes upfolded artefacts.

produce high-amplitude and low-frequency artefacts in the shallow part, while $S_uR_d$ is the upward-folded ray-path result that has the same travel time of the true physical ray path, which generate incorrect RTM images (F. Liu *et al.* 2011, W. Wang *et al.* 2016), as shown in Figure 2.1. The true-reflector image is produced by the cross-correlation of the down-going source and up-going receivers, $S_dR_u$, which is consistent with the true ray path of the seismic wave propagation. Therefore, a causal imaging condition was proposed to only containing the physical term, $S_dR_u$.

Theoretically, this up-/down- going wavefield decomposition can be achieved by the Poynting vector, which is the product of the spatial and temporal derivatives of the wavefield. This Poynting vector is regarded as an indicator for the propagation direction of the seismic waves, as it presents the direction of wave energy propagation (Yoon & Marfurt 2006). This method can achieve artefact elimination in simple models, where the ray-path is relatively direct. However, in complex models with various reflectors, due to the overlap and superposition of the waveforms, the Poynting-vector decomposed wavefield is scattered, and the waveform is discontinuous, which introduces noise to the image, and the migration results are unsatisfactory.

To overcome the discontinuous waveform issue in decomposition, it is more achievable to decompose the wavefield in the frequency-wavenumber domain. The propagation velocity is introduced to identify the propagation direction. The vertical propagation velocity $v_z$ is defined as

$$v_z = \frac{\omega}{k_z} \tag{2.4}$$

where $k_z$ is the vertical wavenumber. When $v_z \geq 0$, the wave goes downwards, and when $v_z < 0$, the wave goes upwards (the $z$ axis is vertically going downward). This method can achieve continuous waveform, and subsequently, generate satisfying migration images when eliminating the up-going source and down-going receiver wavefield. However, the computational cost is extremely large, as the calculation of frequency requires the storage of the entire wavefield history to implement Fourier transforms. For a small model with $500 \times 500$ grids and 6000 timesteps, it needs at least 5.59 Gb to store the wavefield at every time step to calculate the frequency. The memory issue can be formidable for large geological models or 3D cases.

This memory problem can be solved by constructing the analytical wavefield (Fei *et al.* 2015), which can realize the explicit wavefield separation, however, dismissing the requirement of the storage of the entire wavefield history. As shown in Eq. (2.4), the sign of the propagation velocity is determined by the signs of the frequency and the wavenumber component. The analytical wavefield is based on the Hilbert transform, and the negative frequencies are eliminated. The Hilbert transform is to impart a $\pm\pi/2$ phase shift for each frequency component, based on the sign of the frequency. The analytical wavefield is established by the original wavefield as the real part and its Hilbert-transformed wavefield as the imaginary part. The spectrum of the analytical wavefield only contains non-negative half, with double amplitude, compared with the original wavefield.

With the analytical wavefield, the propagation direction of seismic waves can be determined by the sign of the wavenumber only, which can be conveniently obtained via a spatial FFT, and the frequency sign in Eq. (2.4) is always positive. Thus, the storage of the entire wavefield can be avoided, and the computational memory can be greatly released. The analytical wave equation can be established from the acoustic wave equation (Shen & Albertin 2015), with an analytical source function on the right-hand side. This analytical wave equation allows for the same propagation process as the conventional acoustic wave equation, and the analytical wavefield can be obtained in every time step, which greatly benefits the wavefield decomposition.

Current research on wavefield decomposition only focuses on the up-/down- going wavefield decomposition, and ignores the waves propagated along the vertical direction. The incorrect cross-correlation between irrelevant left- and right-going waves will also cause artefacts, especially in complex geological models with large-tilted interfaces. Thus, the higher-resolution migration images can be obtained by decomposing the wavefield both vertically and horizontally, and selecting the appropriate cross-correlation terms into the imaging condition.

Additionally, the method for establishing the analytical wavefield in viscoelastic media is not yet investigated, and the wavefield decomposition is not implemented in attenuation compensation reverse-time migration, as there is no attenuation compensation scheme for analytical wavefield. With both attenuation compensation and wavefield decomposition, the signal-to-noise ratio can be further improved and the quality of the migration images can be enhanced.

## 2.4 Contributions

Based on the review above, the key objective of this thesis is to deepen the understanding of the viscoelastic theory and generate high-resolution reverse-time migration images by improving the signal-to-noise ratio. The improvement of the reverse-time migration images is performed in two aspects: one is compensation for attenuation based on the development of the viscoelastic theory, and the other is the elimination of the artefacts generated during the reverse-time migration algorithm. Specifically, the following contributions are made:

1. The causality and stability of the generalised viscoelastic wave equation are proven, which is the necessary condition for wave equations. The viscoelastic parameters in the generalised wave equation are determined.
2. A fractional spatial derivatives wave equation with a spatial filter is developed, which is numerically efficient in seismic simulation. This equation is effectively implemented in attenuation compensation in reverse-time migration.
3. Reverse-time migration by biaxial wavefield decomposition is developed to improve the resolution by removing the artefacts. This method is proven to work well in a field dataset.

# Chapter 3

# Determination of the viscoelastic parameters for the generalised viscoelastic wave equation

The generalised viscoelastic wave equation combines pure elasticity and viscoelasticity in a compact form and follows the basic power-law attenuation, thereby accurately representing seismic wave propagation in attenuating media. Nevertheless, the key parameters of this generalised equation, the viscoelastic parameter and the viscoelastic velocity, are not well formulated. The aim of this chapter is to determine the viscoelastic parameters and apply this equation in seismic simulation. In this chapter, it is proven that the generalised wave equation satisfies the basic causality and stability requirements. Then the key parameters are established in terms of conventional viscoelastic parameters. The viscoelastic parameter is formulated based on the well-developed constant $Q$ model and the viscoelastic velocity is determined in terms of the reference velocity. These two formulations adequately represent the viscoelastic effects in seismic wave propagation and lead to an accurate simulation of the generalised viscoelastic wave equation.

## 3.1 Introduction

The viscoelasticity of the subsurface media causes a dissipation effect that includes energy absorption and velocity dispersion and has a significant impact on field seismic records and images. The dissipation effect is usually quantified by the quality factor $Q$, which is defined by the ratio of stored energy to lost energy per cycle. This quality factor should theoretically be frequency dependent, which is confirmed by some broadband seismological observations (Y. Wang 2008b, Adam *et al.* 2009, Borgomano *et al.* 2017) In some studies on $Q$ observations from field and laboratory data, the quality factor can be considered frequency-independent within a relatively low and narrow frequency band, which is called the constant-$Q$ model (Kjartansson 1979, Aki & Richards 1980). This frequency-independent $Q$ is practical for seismic modelling and imaging.

Conventional physical models to describe viscoelasticity use the combination of spring (elasticity) and dashpot (viscosity), such as the Maxwell model, the Kelvin–Voigt model, the standard linear solid model (Zener 1948). Among these models, the generalised Zener model and the generalised Maxwell model (Emmerich & Korn 1987, Moczo *et al.* 2014) are most commonly used and they are equivalent to each other (Moczo 2005) as they produce exponential relaxation functions. However, the quality factor is implicitly represented by several relaxation parameters, which makes the inverse problem quite challenging (Fichtner & van Driel 2014). Mathematically, the viscoelasticity of the Earth's media can be described using a fractional time-derivative (Caputo 1967) and the constant-$Q$ model was developed based on this fractional time-derivative (Kjartansson 1979). The form of fractional time-derivative is also used for the fractional Zener model to describe the mechanism of viscoelasticity (Liu & Greenhalgh 2019). Among these models, the Kjartansson's constant-$Q$ model is widely used in the exploration seismology because it matches well with the attenuation coefficients from field and laboratory data (Y. Wang 2008b). However, the phase velocity of this constant $Q$ model is erroneous at low frequencies because the phase velocity at zero frequency is zero.

A condensed form of the wave equation can be established by explicitly including a viscoelastic parameter $\beta$ in a stress-strain relationship (Y. Wang 2016). This wave equation combines the purely elastic and viscoelastic cases as follows:

$$\frac{\partial^2 u}{\partial t^2} = c^2(\beta)\nabla^2\left(1+\beta\tau^\beta \frac{\mathrm{d}^\beta}{\mathrm{d}t^\beta}\right)u, \tag{3.1}$$

where $u$ is the scalar wavefield, $\tau$ is the retardation time, and $c(\beta)$ is the viscoelastic velocity. While the purely elastic model has a linear stress-strain relationship, the viscoelastic model uses a fractional temporal derivative to accurately represent the stress-strain relationship. The generalised viscoelastic wave equation attempts to combine elasticity and viscoelasticity into a single form, and this equation follows the basic power-law attenuation.

When the viscoelastic parameter $\beta$ varies between 0 and 1, the generalised wave equation correctly represents the general viscoelastic model and thus the wave phenomena in seismic simulations. If $\beta = 1$, it is the classical Kelvin-Voigt model, which is a combination of an "elastic (Hooke's law) plus viscous (Newtonian fluid)" stress-strain behaviour. Although this model is acknowledged as a fundamental rheological model, it is incapable of incorporating realistic attenuation as it fails to describe an instantaneous nonzero strain response of a stress perturbation (Moczo *et al.* 2014). In this model, viscosity is represented by the first-order time-derivative. The integer-order time-derivative is generalised into a fractional time-derivative, to represent a general viscoelasticity, which is referred as 'anelasticity' in some work. Nevertheless, the terminology of viscoelasticity is often retained in the literature. Thus, the generalization is not only to unify the purely elastic and viscoelastic responses, but also to extend the linear viscosity to a general nonlinear viscosity to describe the realistic attenuation. In this paper, an explicit form of the rate-of-relaxation function is presented, which proves that the generalised viscoelastic wave equation is stable and causal, which is a necessary condition for the wave equation.

Viscoelasticity can be represented by three parameters conventionally: the reference velocity, the reference frequency, and the quality factor. In the generalised viscoelastic wave equation (Eq. 3.1), the three parameters controlling viscosity are: the viscoelastic velocity, the reference frequency, and the viscoelastic parameter $\beta$ (Y. Wang 2016). Therefore, there is a gap between the parameters in the generalised equation and their counterparts in conventional models. In this chapter, the viscoelastic parameter $\beta$ is formulated with the quality factor $Q$ by adopting Kjartansson's constant-$Q$ model, for an appropriate representation of viscoelasticity in the wave equation. The proposed $Q$–$\beta$ relationship exhibits the same pattern as the theoretical solution and agrees well with the field data. The viscoelastic velocity is also determined based on the reference velocity, and this viscoelastic velocity is a function of the viscoelastic parameter $\beta$. The numerical examples, using the Grünwald–Letnikov expansion method, show that the proposed viscoelastic wave equation can well represent the effect of energy absorption and velocity dispersion. This chapter has been published in *Geophysical Journal International* (Xu & Wang 2023).

## 3.2 Causality and stability of the generalised wave equation

A rigorous derivation of the rate-of-relaxation function will prove that the generalised viscoelastic wave equation satisfies the basic requirements of causality and stability.

The generalised stress-strain relation is a combination of Hooke's law and the fractional time derivatives (Y. Wang 2016),

$$\sigma(t) = E\left[\varepsilon(t) + \beta\tau^{\beta}\frac{\mathrm{d}^{\beta}\varepsilon(t)}{\mathrm{d}t^{\beta}}\right], \tag{3.2}$$

where $\sigma(t)$ is the time-dependent stress, $\varepsilon(t)$ is the corresponding strain, and $E$ is the Young's modulus describing the elasticity of the media. In Eq. (3.2), $\tau = \omega_0^{-1}$, where $\omega_0$ is the reference frequency.

The complex modulus is the modulus in the stress–strain relationship in the frequency domain. The complex modulus of the generalised viscoelastic wave equation can be calculated in the frequency domain as follows:

$$M(\omega) = E\left[1+\beta\left(\mathrm{i}\frac{\omega}{\omega_0}\right)^{\beta}\right] = E\left[1+\beta\left|\frac{\omega}{\omega_0}\right|^{\beta} e^{\mathrm{i}\,\mathrm{sgn}(\omega)\pi\beta/2}\right], \tag{3.3}$$

where $\mathrm{sgn}(\omega)$ is the signum function. The inverse Fourier transform of the complex modulus is the rate-of-relaxation function in the time domain, which is the kernel of a time convolution. This rate-of-relaxation function (time-dependent modulus) consists of two terms:

$$\Psi(t) = E\left[\Psi_e(t) + \Psi_v(t)\right], \tag{3.4}$$

where $\Psi_e(t)$ is the modulus-normalized rate-of relaxation function for the elastic component, and $\Psi_v(t)$ the modulus-normalized rate-of relaxation function for the viscoelastic component.

The rate-of relaxation function for the elastic component is obtained by taking the inverse Fourier transform to unity, i.e. $\Psi_e(t) = \delta(t)$, which is the delta function. The rate-of relaxation function for the viscoelastic component is related to the fractional power as

$$\begin{aligned}
\Psi_v(t) &= \frac{\beta}{2\pi\omega_0^{\beta}}\int_{-\infty}^{\infty}|\omega|^{\beta}\,\mathrm{e}^{\mathrm{i}\,\mathrm{sgn}(\omega)\pi\beta/2}\mathrm{e}^{i\omega t}\mathrm{d}\omega \\
&= \frac{\beta}{2\pi\omega_0^{\beta}}\left(\int_{-\infty}^{0}(-\omega)^{\beta}\,\mathrm{e}^{-\mathrm{i}\pi\beta/2}\mathrm{e}^{i\omega t}\mathrm{d}\omega + \int_{0}^{\infty}\omega^{\beta}\mathrm{e}^{\mathrm{i}\pi\beta/2}\mathrm{e}^{i\omega t}\mathrm{d}\omega\right) \\
&= \frac{\beta\mathrm{e}^{\mathrm{i}\pi\beta/2}}{2\pi\omega_0^{\beta}}\int_{0}^{\infty}\omega^{\beta}\mathrm{e}^{i\omega t}\mathrm{d}\omega + \frac{\beta\mathrm{e}^{-\mathrm{i}\pi\beta/2}}{2\pi\omega_0^{\beta}}\int_{-\infty}^{0}(-\omega)^{\beta}\,\mathrm{e}^{-\mathrm{i}\pi\beta/2}\mathrm{e}^{i\omega t}\mathrm{d}\omega.
\end{aligned} \tag{3.5}$$

Consider two cases separately, $t \geq 0$, and $t < 0$. When $t \geq 0$, Eq. (3.5) becomes

$$\begin{aligned}
\Psi_v(t) &= \frac{\beta \mathrm{e}^{\mathrm{i}\pi\beta/2}}{2\pi\omega_0^\beta}\int_0^\infty \omega^\beta \mathrm{e}^{\mathrm{i}\omega t}\mathrm{d}\omega + \frac{\beta \mathrm{e}^{-\mathrm{i}\pi\beta/2}}{2\pi\omega_0^\beta}\int_0^\infty x^\beta \mathrm{e}^{-\mathrm{i}\pi\beta/2}\mathrm{e}^{-\mathrm{i}xt}\mathrm{d}x \\
&= \frac{\beta \mathrm{e}^{\mathrm{i}\pi\beta/2}}{2\pi\omega_0^\beta}\frac{\Gamma(\beta+1)}{(-\mathrm{i}t)^{\beta+1}} + \frac{\beta \mathrm{e}^{-\mathrm{i}\pi\beta/2}}{2\pi\omega_0^\beta}\frac{\Gamma(\beta+1)}{(\mathrm{i}t)^{\beta+1}} \\
&= \frac{\beta\Gamma(\beta+1)}{2\pi\omega_0^\beta t^{\beta+1}}\left[\frac{\mathrm{e}^{\mathrm{i}\pi\beta/2}}{(-\mathrm{i})^{\beta+1}} + \frac{\mathrm{e}^{-\mathrm{i}\pi\beta/2}}{(\mathrm{i})^{\beta+1}}\right] \\
&= \frac{\beta\Gamma(\beta+1)}{2\pi\omega_0^\beta t^{\beta+1}}\left[\mathrm{e}^{\mathrm{i}(\pi\beta+\pi/2)} + \mathrm{e}^{-\mathrm{i}(\pi\beta+\pi/2)}\right] \\
&= -\frac{\beta\Gamma(\beta+1)}{\pi\omega_0^\beta t^{\beta+1}}\sin(\pi\beta),
\end{aligned} \tag{3.6}$$

where $\Gamma(\bullet)$ is the gamma function. When $t<0$, Eq. (3.5) is

$$\begin{aligned}
\Psi_v(t) &= \frac{\beta \mathrm{e}^{\mathrm{i}\pi\beta/2}}{2\pi\omega_0^\beta}\int_0^\infty \omega^\beta \mathrm{e}^{i\omega t}\mathrm{d}\omega + \frac{\beta \mathrm{e}^{-\mathrm{i}\pi\beta/2}}{2\pi\omega_0^\beta}\int_{-\infty}^0 (-\omega)^\beta\, \mathrm{e}^{-\mathrm{i}\pi\beta/2}\mathrm{e}^{i\omega t}\mathrm{d}\omega \\
&\xrightarrow{t=-\tau} \frac{\beta \mathrm{e}^{\mathrm{i}\pi\beta/2}}{2\pi\omega_0^\beta}\int_0^\infty \omega^\beta \mathrm{e}^{-i\omega\tau}\mathrm{d}\omega + \frac{\beta \mathrm{e}^{-\mathrm{i}\pi\beta/2}}{2\pi\omega_0^\beta}\int_{-\infty}^0 (-\omega)^\beta\, \mathrm{e}^{-\mathrm{i}\pi\beta/2}\mathrm{e}^{-i\omega\tau}\mathrm{d}\omega \\
&= \frac{\beta \mathrm{e}^{\mathrm{i}\pi\beta/2}}{2\pi\omega_0^\beta}\int_0^\infty \omega^\beta \mathrm{e}^{-i\omega\tau}\mathrm{d}\omega + \frac{\beta \mathrm{e}^{-\mathrm{i}\pi\beta/2}}{2\pi\omega_0^\beta}\int_0^\infty (x)^\beta\, \mathrm{e}^{-\mathrm{i}\pi\beta/2}\mathrm{e}^{+ix\tau}\mathrm{d}x \\
&= \frac{\beta \mathrm{e}^{\mathrm{i}\pi\beta/2}}{2\pi\omega_0^\beta}\frac{\Gamma(\beta+1)}{(\mathrm{i}\tau)^{\beta+1}} + \frac{\beta \mathrm{e}^{-\mathrm{i}\pi\beta/2}}{2\pi\omega_0^\beta}\frac{\Gamma(\beta+1)}{(-\mathrm{i}\tau)^{\beta+1}} \\
&= \frac{\beta\Gamma(\beta+1)}{2\pi\omega_0^\beta \tau^{\beta+1}}\left[\frac{\mathrm{e}^{\mathrm{i}\pi\beta/2}}{(\mathrm{i})^{\beta+1}} + \frac{\mathrm{e}^{-\mathrm{i}\pi\beta/2}}{(-\mathrm{i})^{\beta+1}}\right] \\
&= \frac{\beta\Gamma(\beta+1)}{2\pi\omega_0^\beta \tau^{\beta+1}}\left[\mathrm{e}^{-\mathrm{i}\pi/2} + \mathrm{e}^{\mathrm{i}\pi/2}\right] \\
&= 0.
\end{aligned} \tag{3.7}$$

In the inverse Fourier transform above, the following relationship is employed (Gradshteyn & Ryzhik 2000)

$$\int_0^{+\infty} x^{k-1}e^{\mathrm{i}\mu x}dx = \frac{\Gamma(k)}{(-\mathrm{i}\mu)^k} \quad \left(0<\mathrm{Re}(k)<1, \mu\neq 0\right). \tag{3.8}$$

Combining Eqs. (3.5 - 3.7), the rate-of relaxation function $\Psi(t)$ can be written explicitly as

$$\Psi(t) = H(t)\cdot E\left[\delta(t) - \frac{\beta\Gamma(\beta+1)}{\pi\omega_0^\beta t^{\beta+1}}\sin(\pi\beta)\right], \tag{3.9}$$

where $H(t)$ is the Heaviside function. In the rate-of-relaxation function Eq. (3.9), the first term in the parenthesis is a delta function, representing the purely elastic response. Significantly, the second term is proportional to $t^{-(\beta+1)}$.

The rate-of-relaxation function in Eq. (3.9) shows two important features of the system. One feature is causality, since $\Psi(t<0)=0$. The other is stability, since $\lim_{t\to+\infty}\Psi(t)=0$. The rate-of-relaxation function (Eq. 3.9), derived from the generalised stress–strain relation, is a summation of two minimum-phase filters, and satisfies the requirement of causality and stability, which are the necessary conditions of the wave equation (Tarantola 1988). Figure 3.1 shows the rate-of-relaxation function that corresponds to $\beta=\{0.01,\ 0.05,\ 0.1,\ 0.5\}$. The rate-of-relaxation function approaches zero slowly with a large $\beta$ value.

Eq. (3.9) is the summation of two minimum phase filters, and it can be proven that if $\beta=0$ and $\beta=1$, the rate-of-relaxation function of Eq. (3.9) is the minimum phase. However, if $0<\beta<1$, the phase property depends on $\beta$, and it is not guaranteed that the minimum delay is required for each $\beta$ value. The minimum phase requires that both the rate-of-relaxation function and its inverse are causal and stable (Kailath *et al.* 2000).

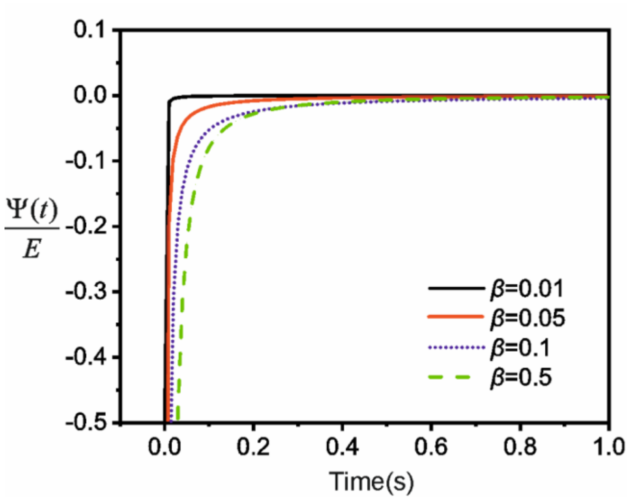


**Figure 3.3** The rate-of-relaxation function varying with time $t$ in the generalised viscoelastic wave equation.

Given the rate-of-relaxation function, the relaxation function itself can be obtained by taking the integral

$$\begin{aligned}\bar{\Psi}(t) &= E\int_0^t \left[ \delta(\tau) - \frac{\beta\Gamma(\beta+1)}{\pi\omega_0^\beta \tau^{\beta+1}} \sin\left(\pi\beta\right) \right] \mathrm{d}\tau \\ &= E\int_0^t \delta(\tau)\mathrm{d}\tau - \frac{E\beta\Gamma(\beta+1)}{\pi\omega_0^\beta} \sin\left(\pi\beta\right) \int_0^t \tau^{-(\beta+1)} \mathrm{d}\tau \\ &= \frac{E\Gamma(\beta+1)}{\pi\left(\omega_0 t\right)^\beta} \sin\left(\pi\beta\right).\end{aligned} \tag{3.10}$$

This form of the relaxation function is proportional to $t^{-\beta}$, which is consistent with the constant $Q$ model.

## 3.3 Formulation of the viscoelastic parameter

The objective of this section is to establish the relationship between the viscoelastic parameter $\beta$ and the quality factor $Q$ by using the well-developed Kjartansson's constant $Q$ model. This constant $Q$ model has been shown to agree well with the measured attenuation coefficient from field data. However, this constant $Q$ model has an unrealistic phase velocity at the end of the low frequencies. The phase velocity approaches zero as the frequency decreases from non-zero to zero. In contrast, Wang's generalised viscoelastic model (Y. Wang 2019) has a phase velocity function that gradually decreases as the frequency decreases from non-zero to zero, and it has a nonzero value of $c(\beta)$ at zero frequency.

The phase velocity $v(\omega)$ and the attenuation coefficient $\alpha(\omega)$ of the generalised viscoelastic model can be written analytically as (Y. Wang 2016)

$$v_g(\omega) = \sqrt{2}c(\beta) \frac{A(\omega)}{\sqrt{A(\omega)+B(\omega)}}, \tag{3.11}$$

$$\alpha_g(\omega) = \frac{|\omega|}{\sqrt{2}c(\beta)} \frac{\sqrt{A(\omega)-B(\omega)}}{A(\omega)}, \tag{3.12}$$

where

$$A(\omega)=\sqrt{1+2\beta\left|\frac{\omega}{\omega_0}\right|^{\beta}\cos(\beta\pi/2)+\beta^2\left|\frac{\omega}{\omega_0}\right|^{2\beta}},$$
$$B(\omega)=1+\beta\left|\frac{\omega}{\omega_0}\right|^{\beta}\cos(\beta\pi/2). \tag{3.13}$$

These formulae lead to the viscoelastic velocity $c(\beta)=v(\beta,\ \omega=0)$. The absolute value in Eq. (3.13) is used to satisfy the anti-Hermitian condition.

Y. Wang (2019) proposed an analytical relationship between $\beta$ and $Q$ based on a theoretical derivation as

$$Q^{-1}=\frac{(\beta/\sqrt{2})\sin(\beta\pi/2)}{1+\beta\cos(\beta\pi/2)}. \tag{3.14}$$

This frequency-independent relationship involves two basic assumptions. First, the frequency band is relatively narrow. Second, the frequencies in seismic exploration data are generally low (Futterman 1962, Morozov *et al.* 2020).

For Kjartansson's constant $Q$ model, the phase velocity is

$$v_c(\omega,Q)=c_0\left(\frac{\omega}{\omega_0}\right)^{\gamma}, \tag{3.15}$$

where $\gamma\approx 1/(\pi Q)$ is a parameter controlling the viscosity, $c_0$ is the reference velocity which can be set as a purely elastic velocity $c_0=c_\infty$. The attenuation coefficient is

$$\alpha_c(\omega)=\frac{\omega}{v_c(\omega)}\tan(\pi\gamma/2). \tag{3.16}$$

To show the difference between the phase velocity and the attenuation coefficient of the two models (Figures 3.2a and 3.2b), the reference velocity is set as 2500 m/s at a reference frequency of 1500 Hz. As shown in Figure 3.2(a), the phase velocity of the Kjartansson's constant $Q$ model decreases significantly for the low frequency wave components, where most of the seismic waves are concentrated. The attenuation coefficients of the two models have a similar linear property, but the slope is clearly different, especially for the case of a small $Q$,

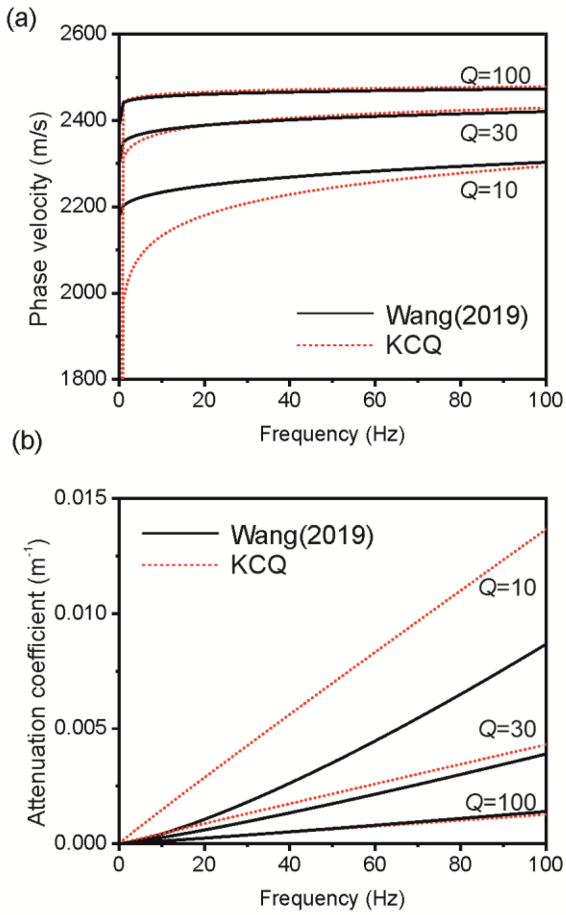


**Figure 3.4** (a) The comparison of the phase velocity between Kjartansson's constant $Q$ (KCQ) model (red dotted line) and the theoretical model of Y. Wang (2019) (black solid line). (b) The comparison of the attenuation between the KCQ model (red dotted line) and the theoretical model of Y. Wang (2019) (black solid line).

which corresponds to strongly attenuating media (Figure 3.2b). This difference is due to the fact that the $Q$- $\beta$ relation in Y. Wang (2019) is valid under the assumption of small dissipation.

To establish a new relationship between $Q$ and $\beta$, the attenuation coefficients of the two models is matched as $\alpha_c(\gamma,\omega)=\alpha_g(\beta,\omega)$, and solve them numerically:

$$\tan\left(\frac{\pi\gamma}{2}\right)\frac{1}{c_0}\left(\frac{\omega}{\omega_0}\right)^{\gamma}=\frac{1}{\sqrt{2}c(\beta)}\frac{\sqrt{A-B}}{A}. \tag{3.17}$$

Both attenuation coefficients are assumed to be linear and vanish at zero frequency, and $\alpha_c(\gamma,\omega_0)=\alpha_g(\beta,\omega_0)$ can be set, Eq. (3.17) becomes

$$\tan\left(\frac{\pi\gamma}{2}\right)\frac{1}{c_0}=\frac{1}{\sqrt{2}c(\beta)}\frac{\sqrt{A_0-B_0}}{A_0}, \tag{3.18}$$

where

$$\begin{aligned} A_0 &= A(\omega_0)=\sqrt{1+2\beta\cos(\beta\pi/2)+\beta^2}, \\ B_0 &= B(\omega_0)=1+\beta\cos(\beta\pi/2). \end{aligned} \tag{3.19}$$

This equation may be solved numerically as

$$\begin{aligned} &\gamma=\sum_{i=1}^{6}a_i\beta^i, \\ &a_i=\{0.00018,\ 0.50060,\ -0.51535,\ 0.41860,\ -0.20296,\ -0.04910\}. \end{aligned} \tag{3.20}$$

Taking into account the relationship $\gamma=(Q\pi)^{-1}$, Eq. (3.20) becomes

$$Q^{-1}=\pi\sum_{i=1}^{6}a_i\beta^i. \tag{3.21}$$

Although Eq. (3.18) is directly solvable, its nonlinearity causes computational inefficiency when implementation. Eq. (3.21) agrees very well with the solution of Eq. (3.18), as shown in Figure 3.3, and it can be efficiently implemented. Moreover, the proposed $Q-\beta$ relation shows the same variation pattern as the theoretical solution in Y. Wang (2019), but the proposed new relation Eq. (3.21) shows stronger attenuation than Y. Wang (2019).

The inverse relationship of Eq. (3.21) can also be obtained numerically as

$$\begin{aligned} &\beta=\sum_{i=1}^{6}b_iQ^{-i/2}, \\ &b_i=\{0.79788,\ 0.31831,\ 0.16787,\ -0.08260,\ -0.08730,\ -0.03774\}. \end{aligned} \tag{3.22}$$

The polynomial of $Q^{-1/2}$ shows that the proposed $Q-\beta$ relation is consistent with the basic power-law attenuation (Wang 2019).

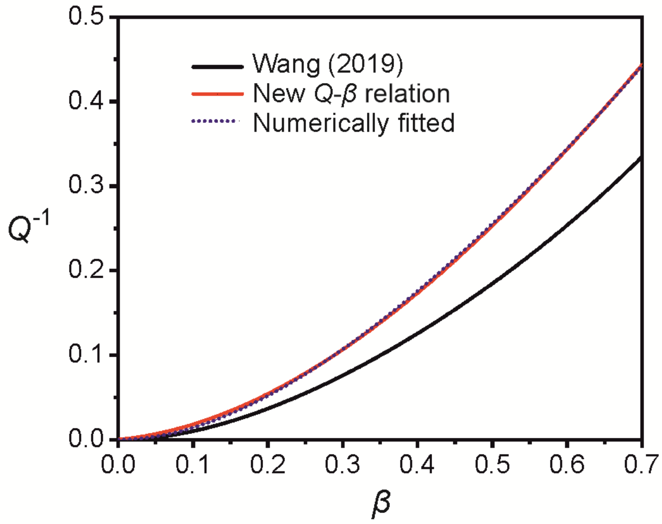


**Figure 3.5** The established $Q-\beta$ relationship, where the red solid line represents the proposed new relationship (Eq. 3.18), and the blue dotted line represents the numerically fitted solution (Eq. 3.21). It is also compared with the $Q$ model (the black solid line) of Y. Wang (2019).

To test the validity of the proposed $Q-\beta$ relation, the theoretical attenuation coefficient is compared with field data from the Pierre Shale (McDonal *et al.* 1958). The field data is measured by 5 detectors positioned in vertical boreholes, and the measured attenuation coefficients were evaluated through Fourier analysis. The quality factor of the Pierre Shale rock is $Q$=32 and the P-wave velocity is 2164 m/s at the reference frequency of 100 Hz. As shown in Figure 3.4, the measured data of McDonal *et al*. (1958) are plotted as diamond points, and the theoretical solution with the proposed $Q-\beta$ relation is plotted as a red solid line. The theoretical attenuation coefficient agrees well with the measured data, and the phase velocity does not decrease significantly ( $c(\beta)=2064.3$ m/s) as the frequency tends towards zero.

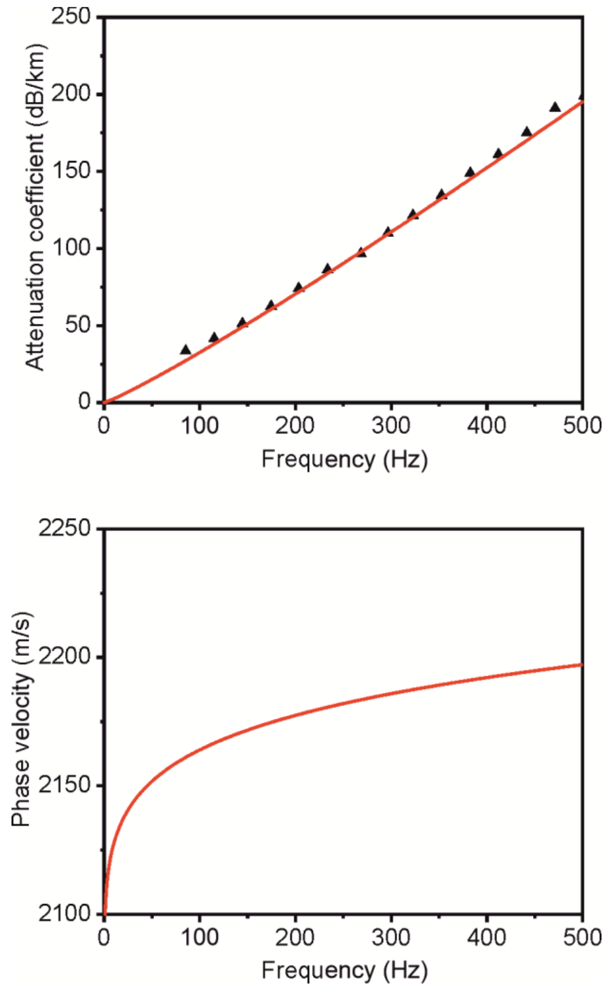


**Figure 3.6** The attenuation and phase velocity with frequency for Pierre Shale with $Q$=32. The red line is the theoretical solution with the proposed new $Q-\beta$ relationship, and the diamond points are the measured data from McDonal *et al*. (1958).

## 3.4 Formulation of the viscoelastic velocity

To solve the generalised viscoelastic wave equation (Eq. 3.1), a model of viscoelastic velocity $c(\beta)$ is required. The viscoelastic velocity $c(\beta)$ is defined by the phase velocity at zero frequency since the expression of the phase velocity of Eq. (3.11) leads to the viscoelastic velocity $c(\beta)=v(\beta,\ \omega=0)$ . The viscoelastic velocity originally results from Young's modulus in the generalised stress–strain relation (Y. Wang 2016), $E=\rho c^2(\beta)$, so the physical meaning of this viscoelastic velocity is the purely elastic contribution of the entire seismic response in attenuating media. In this section, the relationship is established between the viscoelastic velocity $c(\beta)$ and the purely elastic velocity $c_\infty$, which is the velocity at infinite frequency or ray velocity (Y. Wang 2008b). An elastic velocity model is often provided in practical engineering.

The reference velocity can be defined as the phase velocity at the reference frequency, which is

$$c_0 = \sqrt{2}c(\beta)\frac{A_0}{\sqrt{A_0 + B_0}}, \tag{3.23}$$

where $A_0$ and $B_0$ for the case $\omega/\omega_0 = 1$ are given by Eq. (3.19). Then, the viscoelastic velocity $c(\beta)$ can be expressed as follows:

$$c(\beta) = \frac{c_0\sqrt{A_0 + B_0}}{\sqrt{2}A_0} \approx c_0 \frac{1 + 1.80336\beta + 1.55954\beta^2}{1 + 2.30336\beta + 2.33622\beta^2}. \tag{3.24}$$

In this case, the second-order Padé approximation is calculated numerically, which agrees well with the true solution in the entire interval of $\beta \in [0,1]$. Figure 3.5 compares the $\beta$-dependence ($Q$-dependence) of the viscoelastic velocity $c$. The decrease of $c(\beta)/c_0$ corresponding to the increase in $\beta$ (decrease of $Q$) indicates a strong wavefront retardation when viscosity becomes important in the media. This phenomenon is consistent with laboratory and field measurements (McDonal *et al.* 1958, Sams *et al.* 1997b).

Figure 3.6 illustrates the importance of viscoelastic velocity in seismic wave simulations. When setting $c = c_0$ directly, the phase is obviously wrong (Figure 3.6a), as the waveform tends to advance further with stronger attenuation. This is because all the phase velocity is greater than the reference velocity and as the attenuation increases, the phase velocity increases

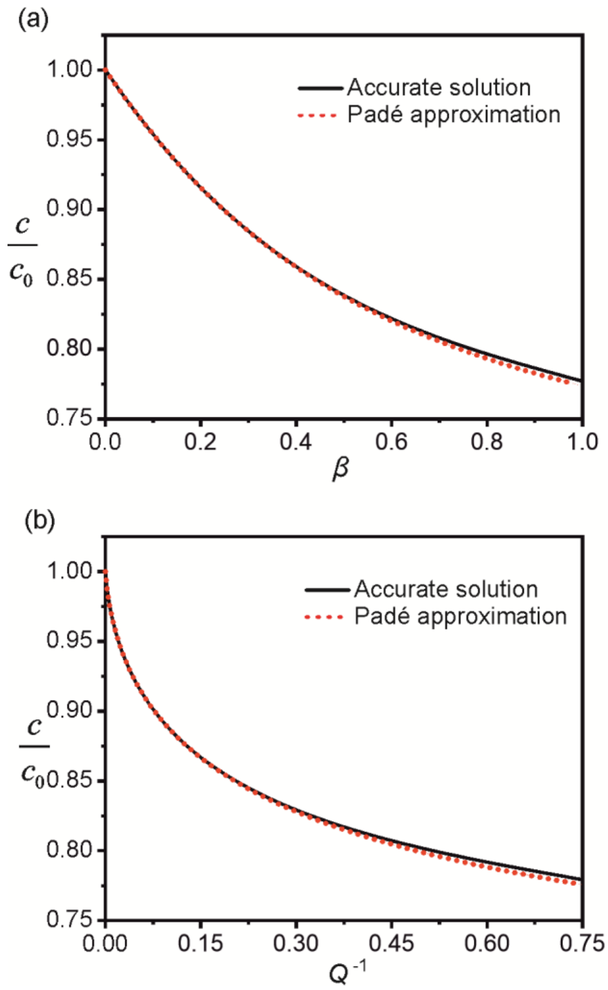


**Figure 3.7** The viscoelastic velocity. (a) The viscoelastic velocity versus the viscoelastic parameter. (b) The viscoelastic velocity versus. $Q^{-1}$. The black solid line is the exact solution, and the red dotted line is the Padé approximation.

accordingly, which is obviously inconsistent with field and laboratory measurements. By introducing the $\beta$-dependency, this velocity can adjust the phase delay in viscoelastic media. Applying the viscoelastic velocity $c(\beta)$ of Eq. (3.24), the waveform (Figure 3.6b) shows that a large $\beta$ value, corresponding to a small $Q$, leads to a strong attenuation in amplitude and a significant time delay in phase. The appropriate delay in the waveform is due to the fact that

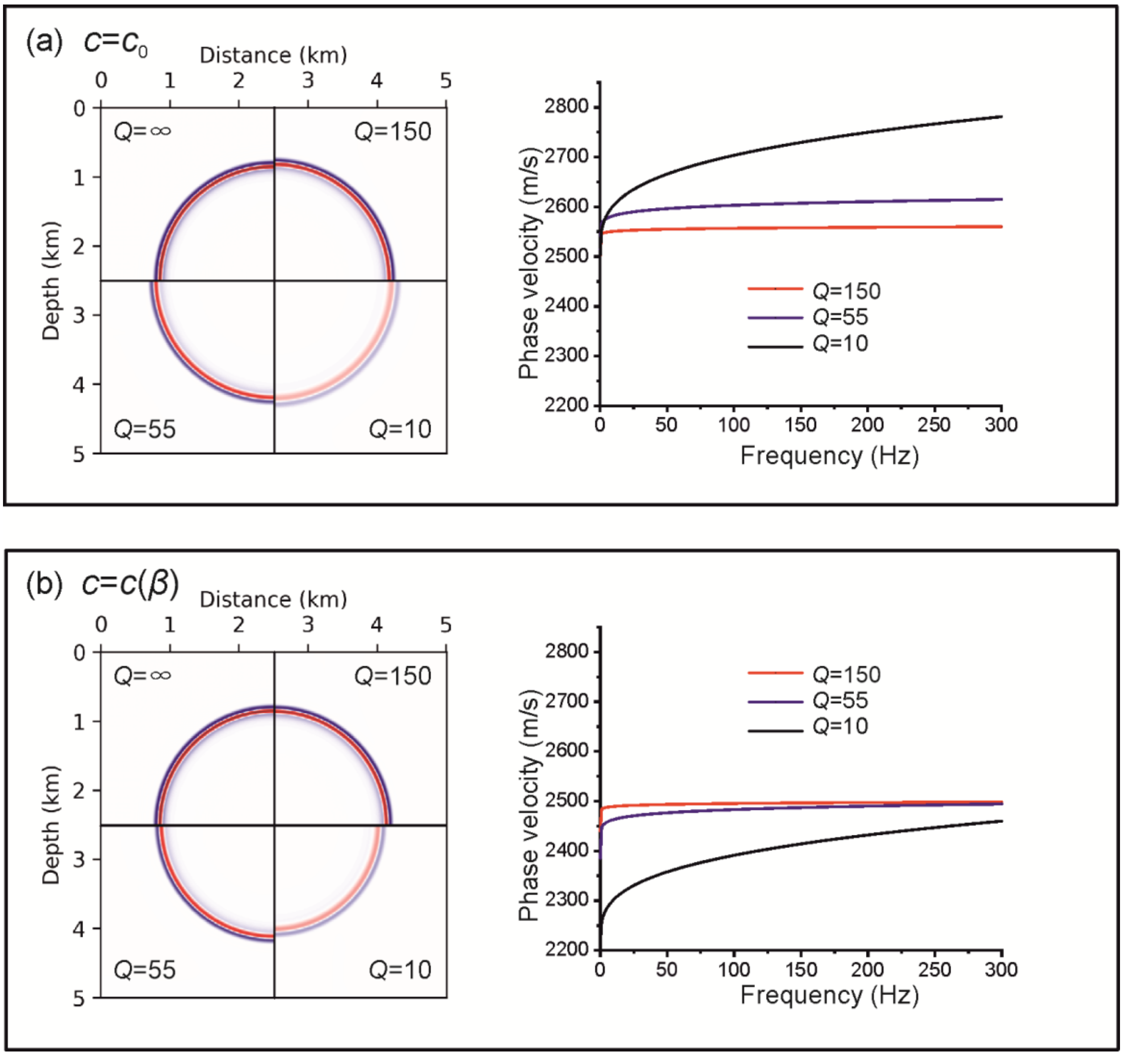


**Figure 3.8** The influence of viscoelastic velocity on the seismic wavefront. (a) The snapshots of the wavefield and the associated phase velocities, when $c = c_0 = 2500$ m/s. (b) The snapshots of the wavefield and the associated phase velocities, when $c = c(\beta)$.

associated phase velocity is greater than $c(\beta)$, but less than $c_0$, and when the attenuation becomes stronger, corresponding to a larger $\beta$, $c(\beta)$ decreases accordingly.

The Kramers-Kronig relationship can be used to verify the accuracy of viscoelastic velocity. The Kramers-Kronig relation has been shown to fit field and laboratory data (Futterman 1962). It represents a Hilbert-transform relationship between the attenuation coefficient and the phase velocity as (Y. Wang 2008b)

$$\frac{\omega}{v(\omega)} = -\mathcal{H}\left(\alpha(\omega)\right) + \frac{\omega}{v_\infty}, \tag{3.25}$$

where $\mathcal{H}(\cdot)$ denotes the Hilbert transform, and $v_\infty$ is the unrelaxed velocity. Two phase velocities are compared here: one is analytically obtained from Eq. (3.11) and the other numerically using Eq. (3.25). Three different $Q$ values, $Q = \{10,\ 30,\ 100\}$, are considered here to present strong, medium, and weak attenuation. From the comparison (Figure 3.7), the analytical phase velocity agrees well with the Kramers-Kronig solution, showing the validity of the viscoelastic velocity of Eq. (3.24).

The attenuation of seismic wave propagation is determined by the viscoelastic parameter, the reference velocity, and the reference frequency. The reference velocity is usually set as a purely elastic (acoustic) velocity. Using Taylor expansion in terms of $\beta$, the phase velocity can be approximated to

$$v_g(\omega) = \sqrt{2}c(\beta)\frac{A}{\sqrt{A+B}} \approx c(\beta)\left[1 + \left(-\frac{1}{8}\beta^2 + \frac{1}{2}\beta\right)\left(\frac{\omega}{\omega_0}\right)^{\beta}\right]. \tag{3.26}$$

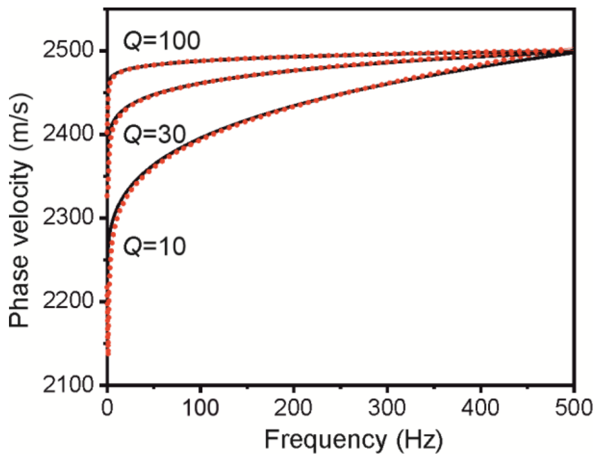


**Figure 3.9** The difference in phase velocities between the analytical phase velocity (black solid line) and the numerical phase velocity determined by Kramers-Kronig relation (red dotted line).

The linearity between the phase velocity and $\omega^{\beta}$ shows that the phase velocity approaches infinity at infinite frequency. However, the reference frequency cannot be set to infinity, otherwise, $(\omega/\omega_0)^{\beta} \to 0$. Thus, the reference velocity cannot be chosen arbitrarily. Therefore, a suitable reference frequency is chosen when the purely elastic (acoustic) velocity is chosen as the reference velocity.

The reference frequency should be large enough for a purely elastic velocity, so the attenuation in the targeted frequency band is insensitive to the variation of the reference frequency. To discuss the sensitivity with respect to the reference frequency, two attenuation coefficients is considered with two reference frequencies, $\omega_{01} = s\omega_{\max}$, and $\omega_{02} = (s+1)\omega_{\max}$, where $\omega_{\max}$ is the highest frequency in the frequency band, and the coefficient $s > 0$ can be considered as the sensitivity index of the reference frequency. A suitable reference frequency for the purely elastic velocity should satisfy approximately identical attenuation when these two different reference frequencies are set. A ratio of two attenuation coefficients is set under the different reference frequencies that are greater than 95%. This means that the variation of the reference frequency does not cause a drastic change in the attenuation. So, this ratio can be expressed as

$$r(s) = \frac{\alpha_g(\omega, \omega_0 = \omega_{02})}{\alpha_g(\omega, \omega_0 = \omega_{01})} = \frac{A_0}{\sqrt{A_0 - B_0}} \frac{\sqrt{A(\omega, \omega_{02}) - B(\omega, \omega_{02})}}{A(\omega, \omega_{02})} \geq 0.95 \cdot \tag{3.27}$$

The above inequality may be solved numerically, and its limit can be obtained as

$$s = 2.882\beta^3 - 9.885\beta^2 + 14.302\beta . \tag{3.28}$$

The increase in $s$ with increasing $\beta \in [0,1]$ shows that strongly attenuative media are more sensitive to the variation of the reference frequency, and therefore require a large reference frequency for the purely elastic velocity in order to keep $(\omega/\omega_0)^{\beta}$ relatively less variable. This conclusion is consistent with Y. Wang & Guo (2004b), which suggested using the highest frequency as the reference frequency. For most geophysical applications with $Q \geq 10$, $\beta \leq 0.3$ and $s \geq 3.424$ are appropriate. Considering the limited frequency band in seismic applications, the reference frequency is proposed to set to 500 Hz, when the purely elastic (acoustic) velocity is the reference velocity.

## 3.5 Seismic wave simulation

The goal of this section is to intuitively represent the viscoelastic effects in geological models and further verify the proposed relationships in complex geological models. The seismic simulation in the Marmousi model is performed. Figures 3.8(a) and 3.8(c) show the acoustic velocity of the Marmousi model, and the $Q$ model, based on the following empirical formula (Ning & Wang 2016):

$$Q = 11.49 \times (c_\infty \times 10^{-3})^{1.879} - 10.57\,. \tag{3.29}$$

This formula is derived from the $Q$ analysis of field 3D seismic data in the Tarim basin China. The corresponding viscoelastic velocity model (Figure 3.8b) is obtained from Eq. (3.24), which is slightly smaller than the purely acoustic velocity, and the viscoelastic parameter $\beta$ model (Figure 3.8d) is obtained from Eq. (3.22). The strongly attenuative media are in the shallow part of the model, while the deep part is the weakly attenuative media.

The wave equation is solved using the finite difference method with staggered-grid to maintain accuracy and eliminate potential numerical dispersion. The fractional time derivative in the wave equation is solved with the Grünwald–Letnikov expansion (Podlubny 1999) as follows:

$$\frac{\mathrm{d}^\beta u}{\mathrm{d}t^\beta} \approx \frac{1}{\Delta t^\beta} \sum_{m=0}^{t/\Delta t} (-1)^m \binom{\beta}{m} u(t - m\Delta t)\,, \tag{3.30}$$

where $\Delta t$ is the time interval. The model is discretized in 751 ×301 grid points with regular grid spacing of 10 m. A 20-Hz Ricker wavelet is emitted at (3800, 300) m. The time step is 0.1

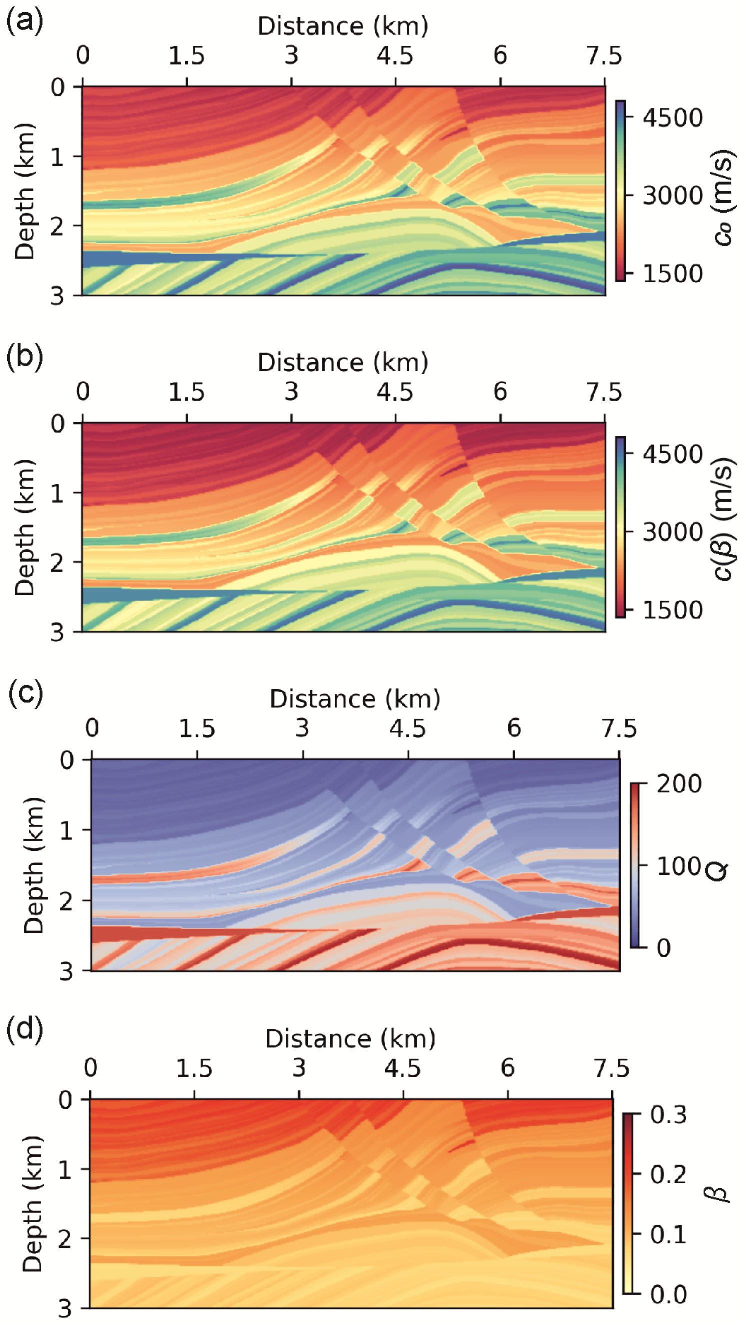


**Figure 3.10** The Marmousi model. (a) The P-wave velocity model. (b) The corresponding viscoelastic velocity model. (c) The $Q$ model, generated by an empirical formula. (d) The corresponding $\beta$ model.

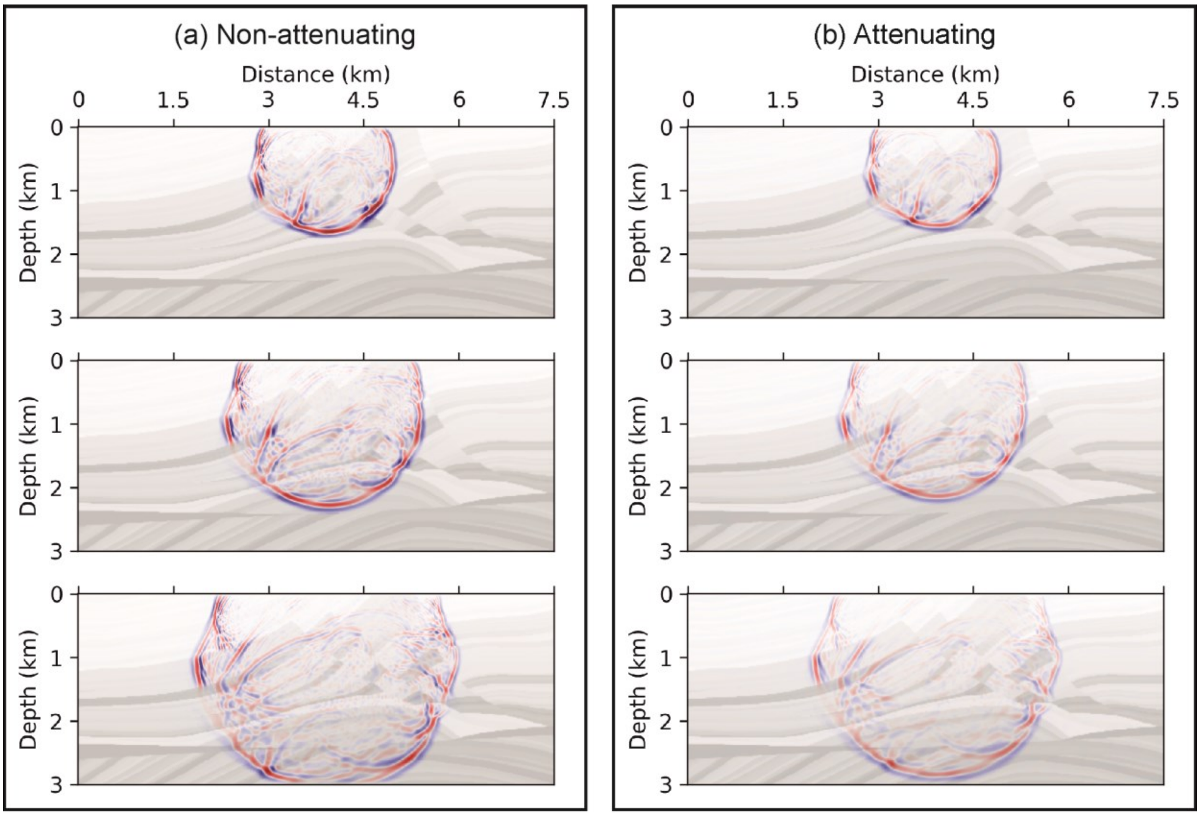


**Figure 3.11** Seismic wave simulations. (a) Snapshots of the non-attenuating wavefield at time 0.6s, 0.8s and 1.0 s. (b) Snapshots of the attenuating wavefield at 0.6s, 0.8s and 1.0 s.

ms. The convolutional perfectly matched layers (CPML) method (Komatitsch & Martin 2007) is applied to four model boundaries to absorb the waves reflected from the boundaries.

Figure 3.9 shows the wavefield snapshots at time 0.6 s, 0.8 s and 1.0 s, respectively, for the non-attenuating and attenuating cases. There are no reflections from the model boundaries, which demonstrates the significance of the convolutional perfectly matched layer. However, there are clear reflected waves from the inner interfaces of the model, in both cases. More importantly, the attenuating wavefields have a significantly delayed waveform and attenuated amplitude, compared with their non-attenuating counterparts.

To further verify the proposed relationships, two travel times are compared: one is estimated via ray-tracing method, and the other is numerical results by the generalised wave equation with the proposed relations. For the ray-tracing method, the delayed travel time $t^*$ is estimated as follows (Aki & Richards 1980, Matheney & Nowack 1995)

$$t^* = \int_S \frac{\mathrm{d}s}{c_r(s)Q(s)}, \tag{3.31}$$

where $t^*$ is the delayed travel time due to the $Q^{-1}$ effect, $c_r(s)$ is the reference ray velocity, $S$ is the travel distance along the ray path. In the viscoelastic case, the wave arriving time is the time travelling through an idealised elastic media plus the perturbation $t^*$ caused by the $Q^{-1}$ factor. It should be noted that this delayed travel time (Eq. 3.31) is frequency-independent, and it is only a reasonable estimation.

The delayed time $t^*$ for ray tracing-method is estimated directly from the ray path, using Eq. (3.31), and can be used as a benchmark for the seismic simulation with the proposed $Q$–$\beta$ relation and the corresponding phase velocity, which are related to the viscoelastic parameter $\beta$. In seismic simulation, the delayed travel time $t^*$ is the travel time difference between the purely acoustic and viscoacoustic cases. Here, the direct wave that propagating downwards is considered, and its ray-path is vertical and identifiable.

As can be seen from Figure 3.10, the maximum time delay is about 13 ms at a maximum distance of 2700 m. Moreover, the delayed travel time increases much faster in the shallow zone where the attenuation is strong than in the zone with low attenuation (deep zone). More importantly, the general consistency of the two delayed travel times shows that the numerical result (black dots) is consistent with the ray-tracing result (red solid line), the accumulated error is less than 5%. The non-smoothness of the numerical result after a depth of 1250 m may be caused by the influence of the reflected waves due to velocity difference. This example shows that the proposed relations reasonably represent the viscoelastic effects in complex geological models.

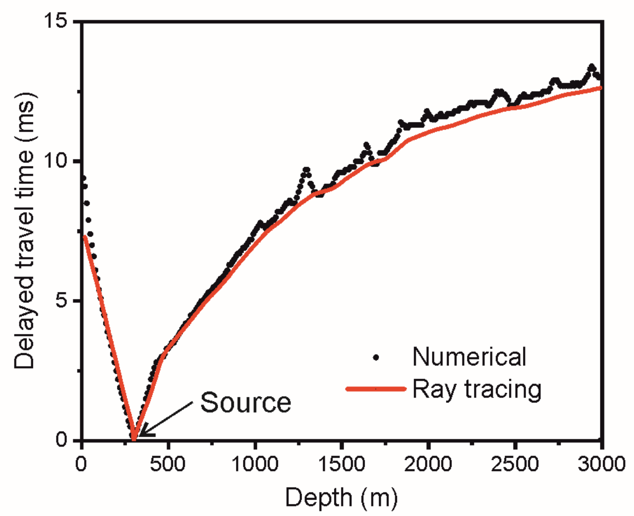


**Figure 3.12** The comparison of the delayed travel times. The red solid curve is the delay time estimated using the $t*$ ray-tracing method, and the black dots are the numerical results, which are the difference in arrival times from the seismic simulations of the viscoelastic and the pure elastic models.

## 3.6 Conclusion

The generalised viscoelastic wave equation can adequately represent the seismic wave propagation in viscoelastic media, as it unifies pure elasticity and viscoelasticity, and follows the basic power law attenuation. The generalised viscoelastic wave equation is characterized by the viscoelastic parameter $\beta$ and the viscoelastic velocity. This chapter closes the gap between the parameters of the generalised wave equation and the normal equation. First, it has been proved that this generalised wave equation satisfies the basic causality and stability conditions. Then, an explicit $Q$–$\beta$ relation based on Kjartansson's constant $Q$ model is proposed, which agrees with the field data. The proposed relation also agrees with the analytical solution. For wave simulation using the generalised viscoelastic wave equation, the relationship between the viscoelastic velocity and the reference velocity is established, which depends on the viscoelastic parameter. A numerical example has demonstrated that these formulae can correctly represent the dissipation effect of viscoelasticity on the waveforms and improve the accuracy of the seismic simulation.

# Chapter 4

# Wave equation formed with fractional spatial derivatives

In the previous chapter for seismic simulation, the generalised viscoelastic wave equation has the form of a fractional temporal derivative. However, the fractional time derivative is numerically inefficient because it requires a huge amount of memory to store the entire wavefield history. This inefficiency significantly hinders its practical implementation in migration. In this chapter, an efficient implementation strategy for solving the generalised wave equation with fractional temporal derivative is proposed. The fractional temporal derivative (FTD) is transferred into fractional spatial derivatives (FSD), implemented by fast Fourier transforms (FFT), which leads to a significant improvement in computational efficiency. However, a FFT implementation is not rigorously applicable to the heterogeneous model. Therefore, a spatial-position-dependent filter is proposed to correct the error caused by the assumption of non-heterogeneity. Moreover, the proposed wave equation is applied to compensate for the viscoelastic effects in attenuating media. This compensation in reverse-time migration significantly improves the resolution of the migration images.

## 4.1 Introduction

The viscoelasticity of subsurface media causes dissipation effect including the energy absorption and velocity dispersion, and has a significant impact on field seismic records and subsequent seismic images. Conventional models for describing viscoelasticity include Kjartansson's constant-$Q$ model (Kjartansson 1979), the Kolsky model (Kolsky 1953), the Kelvin-Voigt model, the standard linear solid model (Zener 1948), the Cole–Cole model (Cole & Cole 1941) etc. Recently, Y. Wang (2016, 2019) proposed the generalised viscoelastic wave equation, which reasonably represents the attenuation effects in viscoelastic media. In this equation, the viscosity is represented in the form of a fractional temporal derivative (FTD).

The FTD was introduced to describe the viscoelasticity of subsurface media by Caputo (1967). The FTD form is used also for the fractional Zener model to describe the mechanism of the viscoelasticity (X. Liu & Greenhalgh 2019). However, directly solving wave equation with FTD presents a numerical challenge in seismic wave simulation. The FTD might be solved in the frequency domain, but the computation is extremely intensive as it requires to solve numerous Helmholtz equations (Vasilyeva *et al.* 2019). An alternative, but still expensive, method is to solve a convolution equation in the time domain (Carcione *et al.* 2002). The Grünwald-Letnikov expansion can also be used to calculate the FTD but this expansion requires large computational memory to store the wavefield history, even if it is truncated (Podlubny 1999).

A practical way to reduce the computational cost of the FTD is that, when the attenuation is weak, one can transfer the FTD to fractional spatial derivatives (FSDs) (Chen & Holm 2004, Treeby & Cox 2010), and then solve FSDs by Fourier pseudo-spectral method, which greatly lowers the computation memory threshold (Carcione 2010). The FSDs in the wave equation can also be decoupled into velocity dispersion and energy dissipation respectively (Zhu & Harris 2014), and this decoupled wave equation can be further expanded to viscoelastic and tilted transversely isotropic (TTI) media (Zhu & Carcione 2014, Qiao *et al.* 2019, Zhu & Bai 2019). Further, Mu *et al.*. (2022)improved the accuracy of the FSDs in highly attenative media by Taylor series expansion.

When using the pseudo-spectral method to solve the FSDs in the wave equation, it requires that the viscoelastic parameter $\beta(\mathbf{x})$ is a constant in the space. In practice, the viscoelastic parameter $\beta(\mathbf{x})$ is averaged over the space $\mathbf{x}$, to generate a constant $\bar{\beta}$ for the purpose of the spatial Fourier transform. This averaging scheme will cause errors in numerical calculation. Based on the locality principle, Zhu & Harris (2014) propose to interpolate the constant-order solutions generated with each single parameter in whole model. The spatially varying order of FSD is a function of $\beta(\mathbf{x})$. Chen *et al.* (2016) and Xing & Zhu (2019) use either the Taylor expansion or a polynomial approximation to transfer the spatial-varying order FSD into the constant order FSDs, and then implement the pseudo-spectral method directly. Yao *et al.* (2017) apply the Hermite distributed approximation to transfer the spatial-varying FSD to an integral of the fractional derivative of the Delta function, and this fractional derivative can be solved locally. But all these schemes aforementioned sacrifice the efficiency for accuracy to some extent. For example, when using the polynomial approximation to derive the constant-order wave equation (Xing & Zhu 2019), the resultant wave equation includes six fractional Laplacian operators. This scheme greatly lowers the efficiency, compared to the original two-operator equation.

In this chapter, a strategy to solve the FSDs in heterogeneous media is proposed, which would be straightforward in philosophy and simpler in realization. This strategy is to build a spatially varying correction function, and to insert this spatial filter directly into the averaging scheme. Because this spatial filter is frequency-independent, it is efficiently implemented as a coefficient multiplied to the wave equation. Therefore, this filter improves the accuracy and maintains the high efficiency of FFT implementation. Further, the viscoelastic wave equation with the proposed strategy is implemented to attenuation compensated reverse-time migration, which greatly improves the resolution of the seismic images. This chapter has been published in *Pure and Applied Geophysics* (Xu & Wang 2022).

## 4.2 Wave equation formed with fractional spatial derivatives

The wave equation presented in terms of FTD may be transferred to a wave equation formed with FSDs. The ultimate purpose of this transformation is to have an efficient implementation of this wave equation.

The generalised viscoelastic wave equation with FTD (Y. Wang 2016) may be expressed explicitly as the following

$$\frac{\partial^2 u}{\partial t^2} = c^2(\beta)\nabla^2\left(1+\frac{\beta}{\omega_0^\beta}\frac{\mathrm{d}^\beta}{\mathrm{d}t^\beta}\right)u\,, \tag{4.1}$$

where $u$ is the scalar wavefield, $\omega_0$ is the reference frequency, $\beta$ is the viscoelastic parameter, and $c(\beta)$ is the viscoelastic velocity, which means the phase velocity at zero frequency. In the media where the medium parameters are spatially invariant, Eq. (4.1) can be rewritten in the frequency-wavenumber domain as

$$\left[\frac{\omega^2}{c^2} - k^2\left(1+\beta\left(\frac{\omega}{\omega_0}\right)^\beta \cos\frac{\beta\pi}{2} + \mathrm{i}\beta\left(\frac{\omega}{\omega_0}\right)^\beta \sin\frac{\beta\pi}{2}\right)\right]\hat{u} = 0\,, \tag{4.2}$$

where $k$ is the wavenumber, and $\hat{u}$ is the frequency-wavenumber domain wavefield. Now, making an approximation based on the weak attenuation assumption (Zhu & Harris 2014)

$$\frac{\omega}{c_0} \approx k\,, \tag{4.3}$$

where $c_0$ is the reference velocity, Eq. (4.2) is approximated to

$$\left(\frac{\omega^2}{c^2} - k^2 - k^{2+\beta}C_1(\beta) - \mathrm{i}\omega k^{1+\beta}C_2(\beta)\right)\hat{u} = 0\,, \tag{4.4}$$

where

$$C_1(\beta)=\beta\left(\frac{c_0}{\omega_0}\right)^{\beta}\cos\frac{\beta\pi}{2},$$
$$C_2(\beta)=\frac{\beta}{\omega_0}\left(\frac{c_0}{\omega_0}\right)^{\beta-1}\sin\frac{\beta\pi}{2}. \tag{4.5}$$

Applying an inverse Fourier transform to Eq. (4.4), the generalised wave equation in the temporal-spatial domain may be presented as FSDs:

$$\frac{1}{c^2}\frac{\partial^2 u}{\partial t^2}+\left((-\nabla^2)+C_1(\beta)(-\nabla^2)^{1+\beta/2}+C_2(\beta)(-\nabla^2)^{(1+\beta)/2}\frac{\partial}{\partial t}\right)u=0, \tag{4.6}$$

where $u$ is the time-space domain wavefield. Eq. (4.6) decouples the dissipation effect, as the $C_1$ term is from the real part of FTD, which represents the velocity dispersion and the $C_2$ term is from the imaginary part of the FTD, which represents the amplitude absorption (Zhu & Harris 2014). In this equation, $C_1(\beta)$ and $C_2(\beta)$ are assumed to be spatially independent. However, when forming the FSDs for a general viscoelastic case, both terms are spatially variable, because $\beta(\mathbf{x})$ is a spatial function.

For the derivation above, the approximation Eq. (4.3) is a key condition, so that the complex wavenumber $\tilde{k}$ could be replaced with the real wavenumber $k=\tilde{k}_{\mathrm{Re}}$. This approximation to the complex wavenumber is made based on the weak-attenuation assumption. For the complex wavenumber $\tilde{k}$, the real and imaginary part may be written analytically as (Y. Wang 2019)

$$\tilde{k}_{\mathrm{Re}}=\frac{\omega}{v(\beta,\ \omega)}=\frac{|\omega|}{\sqrt{2}c(\beta)}\frac{\sqrt{A+B}}{A}, \tag{4.7}$$

$$\tilde{k}_{\mathrm{Im}}=-\alpha(\beta,\ \omega)=-\frac{|\omega|}{\sqrt{2}c(\beta)}\frac{\sqrt{A-B}}{A}, \tag{4.8}$$

where $v(\beta,\omega)$ is the phase velocity, $\alpha(\beta,\omega)$ is the attenuation coefficient, and the absolute value is for satisficing the anti-Hermitian property of the complex wavenumber.

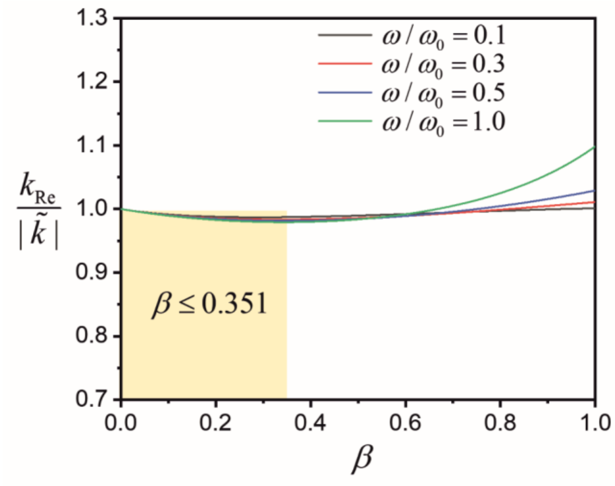


**Figure 4.1** Variation of the weak-attenuation assumption, illustrated by the ratio $R = k_{\mathrm{Re}}/|\tilde{k}|$ versus the viscoelastic parameter $\beta$. The upper side of the yellow square represent $R = 1.0$.

Figure 4.1 illustrates the accuracy of this weak-attenuation assumption with the ratio $R = k/|\tilde{k}|$. Following Y. Wang & Guo (2004b), the reference frequency is set as the highest frequency $\omega_0$ and then $\omega/\omega_0 \le 1$. Figure 4.1 shows that the ratio $R$ is close to 1, for $\beta \le 0.75$, and the relative error is less than 0.5%. When $\beta \le 0.351$, the ratio $R$ is approaching to 1 with decreasing $\beta$. But when $\beta > 0.351$, the ratio $R$ is increasing with an increasing $\beta$. Therefore, the weak-attenuation assumption is valid for $\beta \le 0.351$, for most area of interest to seismic application (Kolsky 1953, Mason 1956, Futterman 1962, Y. Wang 2019).

## 4.3 Accuracy validation

To evaluate the accuracy of FSDs of Eq. (4.6), the wavenumber domain Eq. (4.4) is treated as a non-linear equation $f(k) = 0$. The numerically solved wavenumber is compared to the exact wavenumber of FTD presented analytically in Eqs. (4.7) and (4.8).

Figure 4.2 demonstrates the accuracy evaluation using an arbitrarily chosen pure acoustic velocity $c_0 = 2500$ m/s, and considering cases of weak, median, and strong attenuation with $\beta = (0.010, 0.190, 0.351)$, which is corresponding to $Q = (100,30,10)$, respectively, according to Y. Wang (2019). The accuracy of the phase velocity is high in general, as the root-mean-square (RMS) error in three cases together is 4.169 m/s. The accuracy of the attenuation depends on the $\beta$ value. The RMS errors in the attenuation coefficient are $0.0501\times10^{-3}\mathrm{m}^{-1}$ for $\beta = 0.010$ and $0.3405\times10^{-3}\mathrm{m}^{-1}$ for $\beta = 0.190$. However, the RMS error in the attenuation coefficient is $6.769\times10^{-3}\mathrm{m}^{-1}$ for the extreme case with $\beta = 0.351$. This error existed in the most attenuating case is caused by the approximation $\omega / c_0 \approx k$ (Eq. 4.3) used in the transformation from FTD to FSDs.

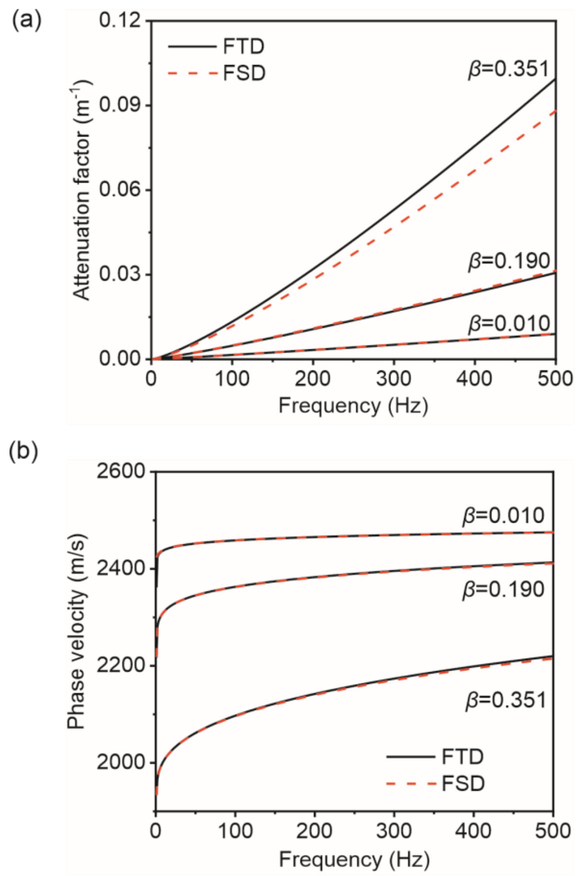


**Figure 4.2** Comparison between the wave equations formed with FTD (solid black curves) and with FSDs (dashed red curves). (a) The attenuation $\alpha(\omega)$. (b) The phase velocity $v(\omega)$.

To investigate the reliability of the FSDs, the analytical solutions of two types of wave equations presented as FTD and FSDs, respectively, are compared. Considering a homogeneous case with constant $\beta$, the one-dimensional analytical solution for FTD in frequency domain is derived as (see Appendix A)

$$\hat{u}(\omega,x) = -\frac{\mathrm{i}e^{\mathrm{i}\omega\Omega_1\|x-x_0\|}}{2\omega}\Omega_1\hat{f}(\omega), \tag{4.9}$$

with

$$\Omega_1 = \frac{1}{c}\left(1+\beta\left(\frac{\mathrm{i}\omega}{\omega_0}\right)^{\beta}\right)^{-1/2}, \tag{4.10}$$

where $\hat{u}(\omega,x)$ is the wavefield in the frequency domain, and $\hat{f}(\omega)$ is the source signature in the frequency domain. For FSDs, the corresponding analytical solution is formed using the Green's function $G(t,k,\tau)$ as (see Appendix B)

$$\hat{u}(t,k) = \int_0^t G(t,k,\tau)f(\tau)\mathrm{d}\tau, \tag{4.11}$$

where $\hat{u}(t,k)$ is the wavefield in the wavenumber domain. The Green's function is derived as

$$G(t,k,\tau) = \begin{cases} 0, & t \le \tau, \\ \dfrac{\sin\left[(t-\tau)\Omega_2\right]}{\Omega_2}e^{-\frac{1}{2}(t-\tau)c^2(\beta)k^{1+\beta}C_2}, & t > \tau, \end{cases} \tag{4.12}$$

where

$$\Omega_2 = ck\sqrt{1+k^{\beta}C_1-\frac{1}{4}c^2k^{2\beta}C_2^2}. \tag{4.13}$$

An inverse Fourier transform of $\hat{u}(t,k)$ with respect to the wavenumber $k$ produces the time-space domain wavefield $u(t,x)$. Note that the Green's function in Eq. (4.12) is presented in terms of a sinc function.

Considering a homogeneous model with the velocity of 2500 m/s, and assuming that the source signature is a Ricker wavelet with the peak frequency of 20 Hz (Y. Wang 2015), Figure 4.3 displays the waveform at travel distance 200 m, and demonstrates that two equations match very well in general, and only a minor discrepancy exists in the strong attenuation case. The RMS differences corresponding to the cases with $\beta$ =(0.010, 0.144, 0.190, 0.351) are ( $5.576\times10^{-2}$ , $6.538\times10^{-2}$ , $7.295\times10^{-2}$ , $22.878\times10^{-2}$ ), respectively. This observation is consistent with that shown in Figure 4.2, that only large error occurs in strongly attenuating media.

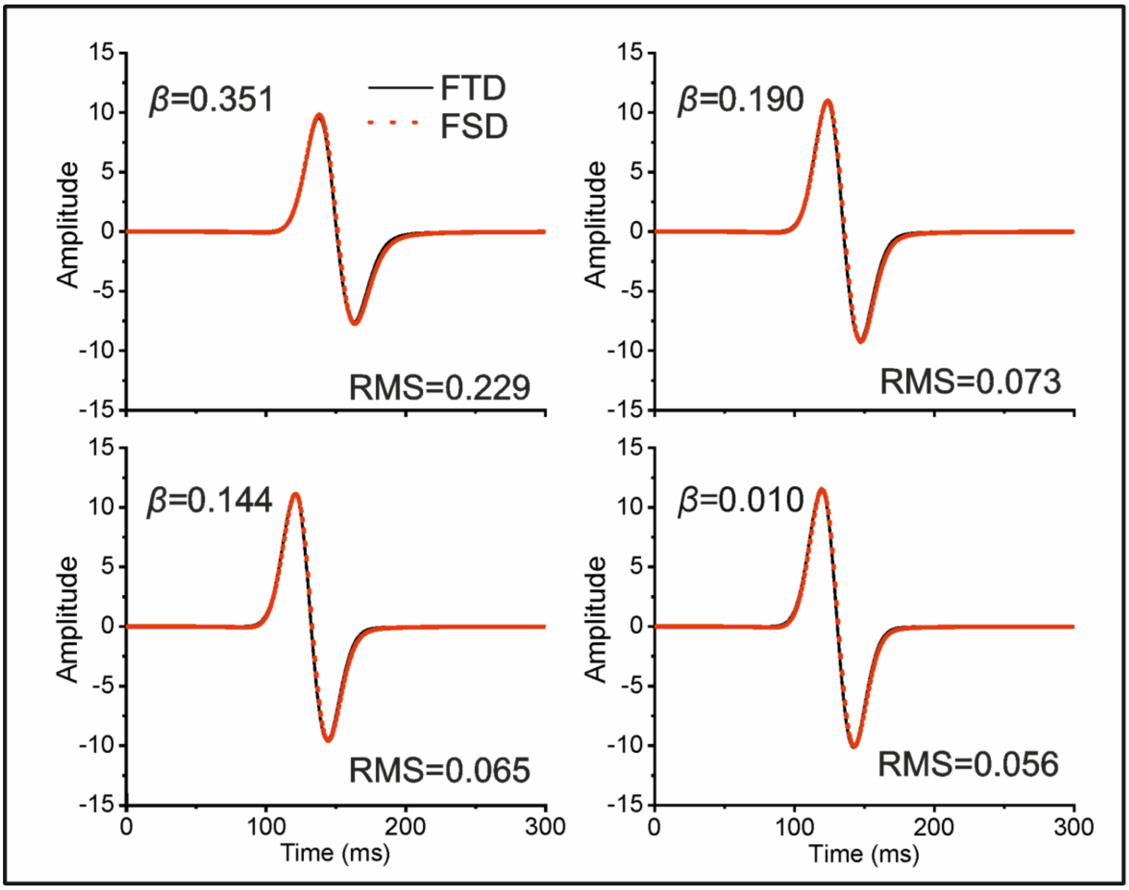


**Figure 4.3** Comparison between the wave equation formed with the FTD (solid red curves) and one with FSDs (dashed black curves). The travel distance is 200 m. The $\beta$ value and the corresponding RMS differences are listed in the plots.

Noted that the above equation with FSDs (Eq. 4.6) is derived based on homogeneous media where the viscoelastic parameter $\beta$ is constant. When forming the FSDs for a general viscoelastic case, $\beta(\mathbf{x})$ is a spatial function. Based on the small perturbation assumption, FSDs is still approximatedly valid for a general viscoelastic case (Zhu & Carcione 2014, Xing & Zhu 2019).

## 4.4 Spatial filter for implementation in heterogeneous media

For the numerical calculation of Eq. (4.6), the pseudo-spectral method is commonly applied to solve the FSD. In practice, the viscoelastic parameter $\beta(\mathbf{x})$ in the heterogeneous media is assumed to be smoothly varied and then the average parameter $\bar{\beta}$ is adopted for calculating the FSD:

$$(-\nabla^2)^{\bar{\beta}/2} u(\mathbf{x}) = \mathcal{F}_{\mathrm{x}}^{-1}\left\{k^{\bar{\beta}} \mathcal{F}_{\mathrm{x}}[u(\mathbf{x})]\right\}, \tag{4.14}$$

where $\mathcal{F}_{\mathrm{x}}$ is the Fourier transform with respect to vector $\mathbf{x}$, and $\mathcal{F}_{\mathrm{x}}^{-1}$ is the inverse of $\mathcal{F}_{\mathrm{x}}$. It should be noted that the smoothly varied heterogeneity assumption here is to employ the averaging method, which is not necessary in FTD wave equation as FTD can be directly solved by finite difference method without performing spatial Fourier transform. The wavefield in the space domain and in the wavenumber domain are listed in pairs as the following:

$$\begin{aligned} u(\mathbf{x}) &\leftrightarrow \mathcal{F}_{\mathrm{x}}[u(\mathbf{x})], \\ -\nabla^2 u(\mathbf{x}) &\leftrightarrow k^2 \mathcal{F}_{\mathrm{x}}[u(\mathbf{x})], \\ (-\nabla^2)^{\beta/2} u(\mathbf{x}) &\leftrightarrow k^{\beta} \mathcal{F}_{\mathrm{x}}[u(\mathbf{x})]. \end{aligned} \tag{4.15}$$

The pseudo-spectral method has been used widely in wave simulation (Carcione 2010). Therefore, the numerical advantage of the FSD is to overcome the memory issue related to the numerical calculation of the FTD in the original wave equation.

In order to correct the errors caused by the averaging scheme of the FFT implementation, a correction function $f(\beta(\mathbf{x}))$ may be introduced as a spatial filter to correct the wavenumber as

$$k^{\beta(\mathbf{x})} = k^{\bar{\beta}} f(\beta(\mathbf{x})). \tag{4.16}$$

Multiplying either $k$ or $k^2$ to both sides, $k^{1+\beta(\mathbf{x})} = f(\beta(\mathbf{x}))k^{1+\bar{\beta}}$ and $k^{2+\beta(\mathbf{x})} = f(\beta(\mathbf{x}))k^{2+\bar{\beta}}$. Therefore, a corrected wave equation which corresponds to Eq. (4.6) is

$$\frac{1}{c^2}\frac{\partial^2 u}{\partial t^2} + \left( (-\nabla^2) + (-\nabla^2)^{1+\bar{\beta}/2} C_1(\beta(\mathbf{x})) f(\beta(\mathbf{x})) + (-\nabla^2)^{(1+\bar{\beta})/2} C_2(\beta(\mathbf{x})) f(\beta(\mathbf{x})) \frac{\partial}{\partial t} \right) u = 0 \tag{4.17}$$

It should be noted that this spatial filter is applied to correct both phase and velocity.

In order to construct the spatial filter, the case of weak attenuation with $k_{\mathrm{Im}} / |\tilde{k}| \ll 1$ can be reasonably assumed and the approximation $\tilde{k} \approx k_{\mathrm{Re}}$ can be made. The real wavenumber $k_{\mathrm{Re}}$ in Eq. (4.7) can be expanded to the first order as

$$k_{\mathrm{Re}} \approx \frac{\omega}{c}\left( 1 + \frac{\bar{\beta}}{8}\cos\left(\frac{\pi\bar{\beta}}{2}\right)\right). \tag{4.18}$$

Then, the spatial filter $f(\beta(\mathbf{x}))$ is evaluated at each grid by

$$\begin{aligned} f(\beta(\mathbf{x})) &= k^{\beta(\mathbf{x})-\bar{\beta}} \\ &\approx k_{\mathrm{Re}}^{\beta(\mathbf{x})-\bar{\beta}} \\ &= \left(\frac{\omega}{c}\right)^{\beta(\mathbf{x})-\bar{\beta}} \left( 1 + \frac{\beta(\mathbf{x})}{8}\cos\left(\frac{\pi\beta(\mathbf{x})}{2}\right)\right)^{\beta(\mathbf{x})-\bar{\beta}} \\ &\approx \left(\frac{\omega_m}{c}\right)^{\beta(\mathbf{x})-\bar{\beta}} \left( 1 + \frac{\beta(\mathbf{x})}{8}\cos\left(\frac{\pi\beta(\mathbf{x})}{2}\right)\right)^{\beta(\mathbf{x})-\bar{\beta}}, \end{aligned} \tag{4.19}$$

where $\omega_m$ is the mean frequency of the seismic band. The central-frequency approximation in the last line is made based on an assumption $\left|\beta(\mathbf{x}) - \bar{\beta}\right| \ll 1$, so that the spatial filter $f(\beta(\mathbf{x}))$ is frequency independent and avoids any extra Fourier transform. Thus, this spatial filter does not affect the efficiency of the algorithm, but greatly improves the accuracy in heterogeneous media.

## 4.5 Numerical example

In this section, three numerical examples are presented. The main objective of the numerical examples is to demonstrate that the filtered averaging scheme produces higher numerical accuracy than the conventional averaging scheme The first example is for validating the effectiveness of the spatial filter.

A constant velocity is set to be 2500 m/s, and consider a model with the viscoelastic parameter values $\beta = (0.351, 0.190, 0.131)$, which is corresponding to *Q*= (10, 30, 60) based on Y. Wang (2019). The source signature is a 20-Hz Ricker wavelet, and the waveforms are recorded at distances of 500 m and 2000 m. These two accurate waveforms are plotted in a single trace in Figure 4.4 (black solid curves).

To mimic the approximation in the viscoelastic wave equation, a "heterogeneous" model with the average value of $\bar{\beta} = (0.237, 0.152, 0.112)$ is assumed, which is corresponding to *Q*= (20, 45, 80). The approximated solutions (in red dots) are overlaid with the accurate trace, as shown in Figure 4.4(a). Three cases have RMS differences of $23.95 \times 10^{-2}$, $9.09 \times 10^{-2}$, and 4.74 $\times 10^{-2}$. These differences are mainly due to the phase discrepancy but is also due to the amplitude difference at large $\beta$ values.

Adopting the correction with the spatial filter, calculated waveforms (in blue dots) are close to the true waveforms, as shown in Figure 4.4(b). The RMS differences are ($2.85 \times 10^{-2}$, $1.05 \times 10^{-2}$, $0.52 \times 10^{-2}$) for the three cases respectively. Both the phase and the amplitude are corrected remarkably. This example shows that the correction function can improve the accuracy of waveform simulation in heterogeneous media, especially in highly-attenuative areas.

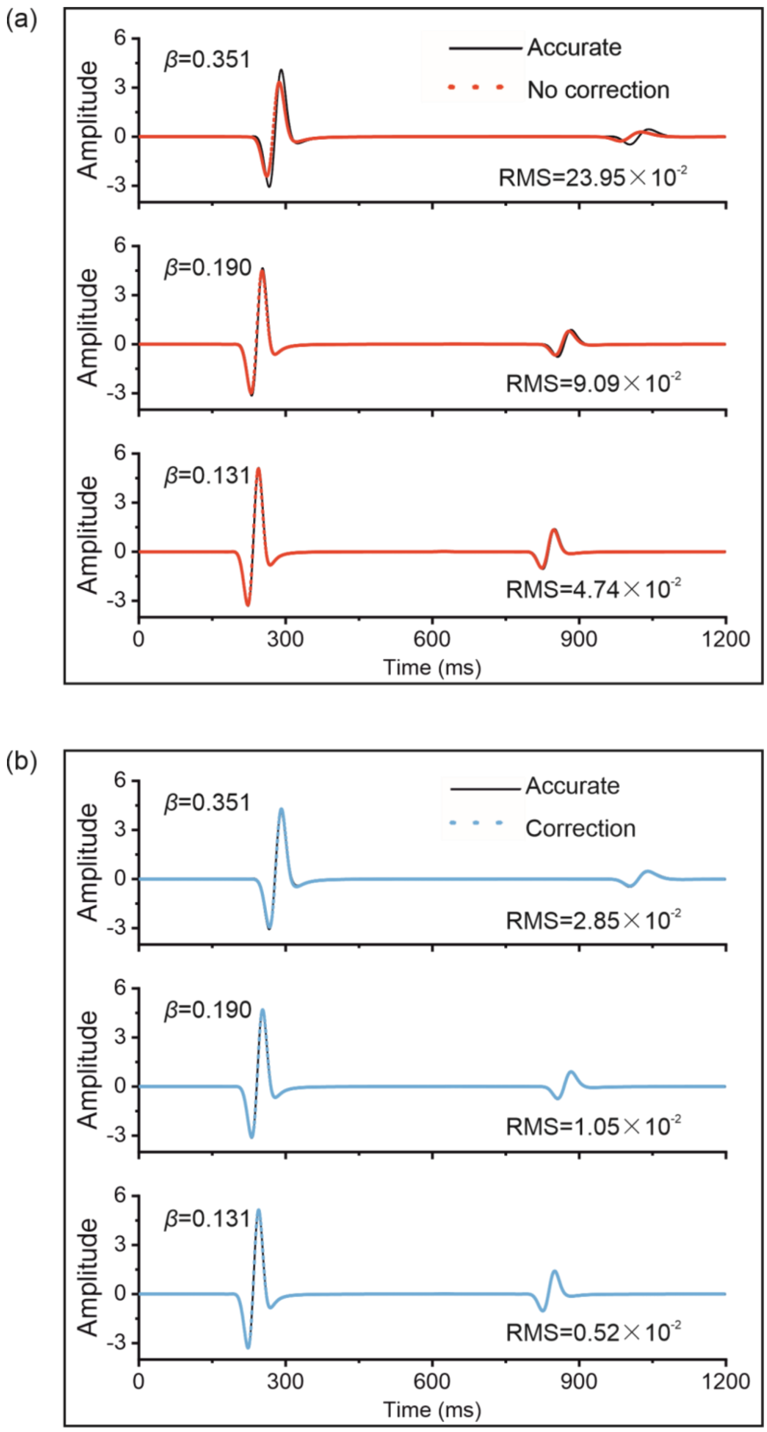


**Figure 4.4** The correction function of wave equation for heterogeneous media. (a) Comparison between the averaging scheme without correction (red dots) and the accurate solution (black solid curves). (b) Comparison between the averaging plus correction scheme (the blue dots) and the accurate solution.

Next, a two-layer model is adopted to validate the scheme. The model is shown in Figure 4.5(a). A reference is set by directly solving Eq. (4.1) using Grünwald-Letnikov expansion (Podlubny 1999) as follows:

$$\frac{\mathrm{d}^{\beta}u}{\mathrm{d}t^{\beta}} \approx \frac{1}{\Delta t^{\beta}} \sum_{m=0}^{t/\Delta t} (-1)^{m} \binom{\beta}{m} u(t - m\Delta t) \tag{4.20}$$

where $\Delta t$ is the time interval. A 20-Hz Ricker wavelet is emitted at the centre of the model. The model is discretized into 801 × 801 grids with grid spacings of 2.5 m. This fine spacing is equivalent to 16 nodes per wavelength ($\lambda_{\min} = v_{\min} / (2.5 f_p)$ = 40 m). The time step is set as $\Delta t$ =0.25 ms, which is also finer than the numerical requirement $\Delta t < \Delta x / (\sqrt{2} v_{\max}) = 0.59$. Fine interval in spatial and temporal axes is set in order to minimize the discrepancy between the Grünwald-Letnikov expansion and the pseudo-spectral method.

Figure 4.5 also displays the wavefield snapshots at 0.35 s of the layered model. The result without correction by the spatial filter (Figure 4.5b) shows significant discrepancy from the reference, which proves that the conventional averaging scheme causes errors. However, after correction (Figure 4.5c), the accuracy is significantly improved. This example further demonstrates the importance of the proposed spatial filter for seismic simulation in heterogeneous media. Any remaining weak residual in Figure 4.5(c) is attributed to the transformation from FTD to FSDs.

In the final example, FSDs of Eq. (4.25) is applied to simulate the wavefield of the Marmousi model. Figure 4.6 displays the acoustic velocity of the Marmousi model, and the $\beta$ model. The $\beta$ model is built based on an analysis of the attenuation versus velocity from a field 3D seismic data in the Tarim basin. The model is discretized into 751 × 301 grid points with regular vertical and horizontal grid spacings of 10 m. The source signature is a 20-Hz Ricker wavelet and is emitted at (3800, 150) m. The receivers are located at a depth of 150 m and in a spatial range of 0~7500 m with 10 m spacing. The time step is 1 ms.

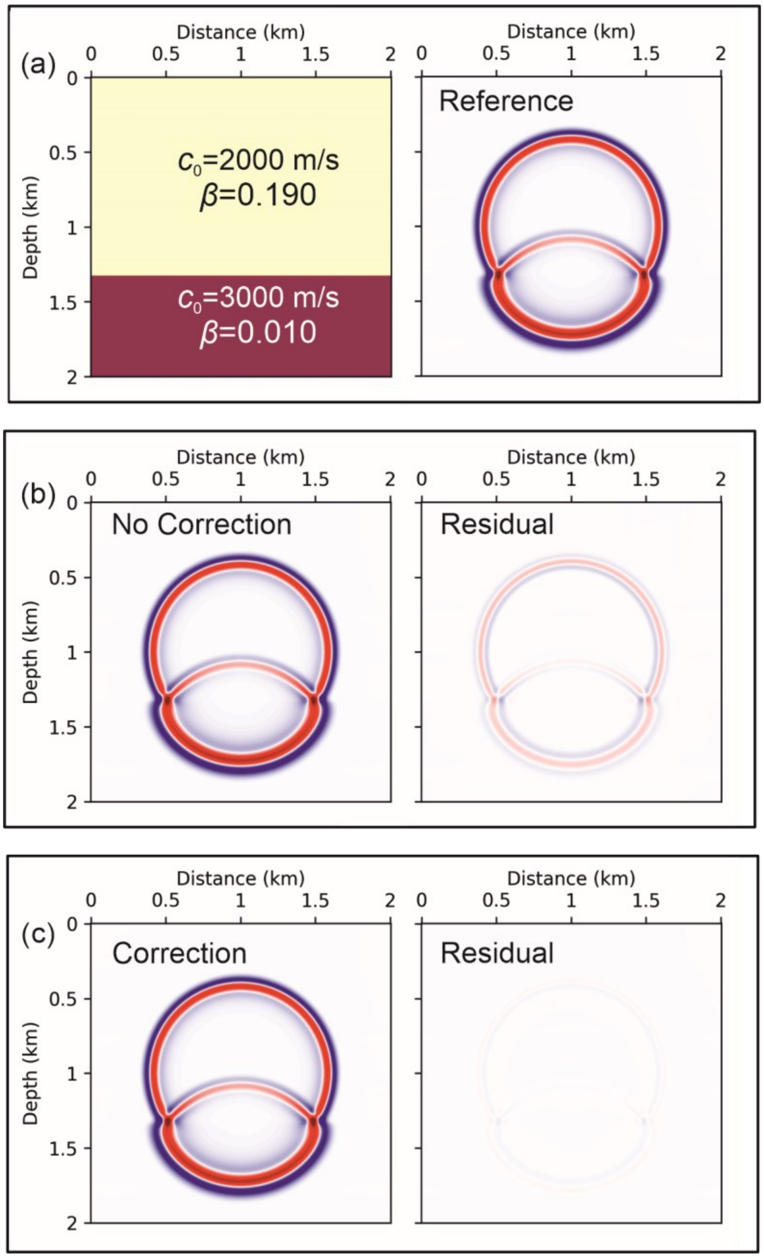


**Figure 4.5** A layered model and wavefield snapshots at 0.35 s. (a) the model parameter and reference wavefield; (b) the wavefield without correction and its residual to reference; (c) the wavefield with correction and its residual to reference.

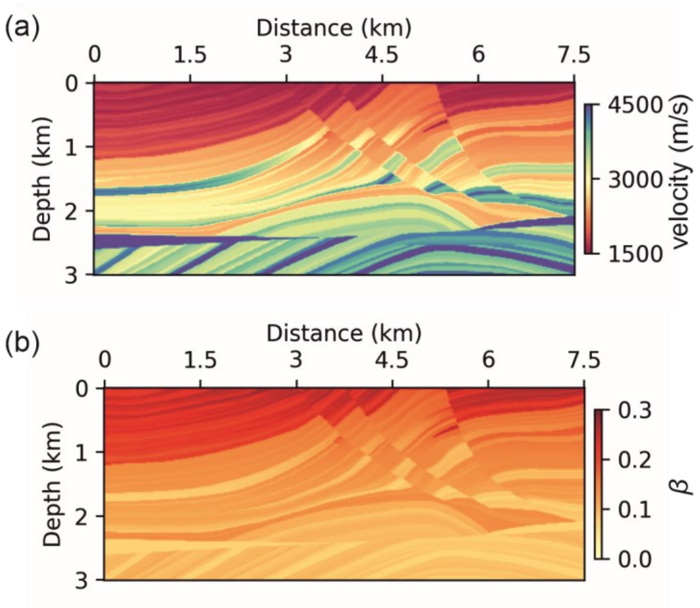


**Figure 4.6** The Marmousi model. (a) The P-wave velocity model. (b) The $\beta$ model, generated through an empirical formula.

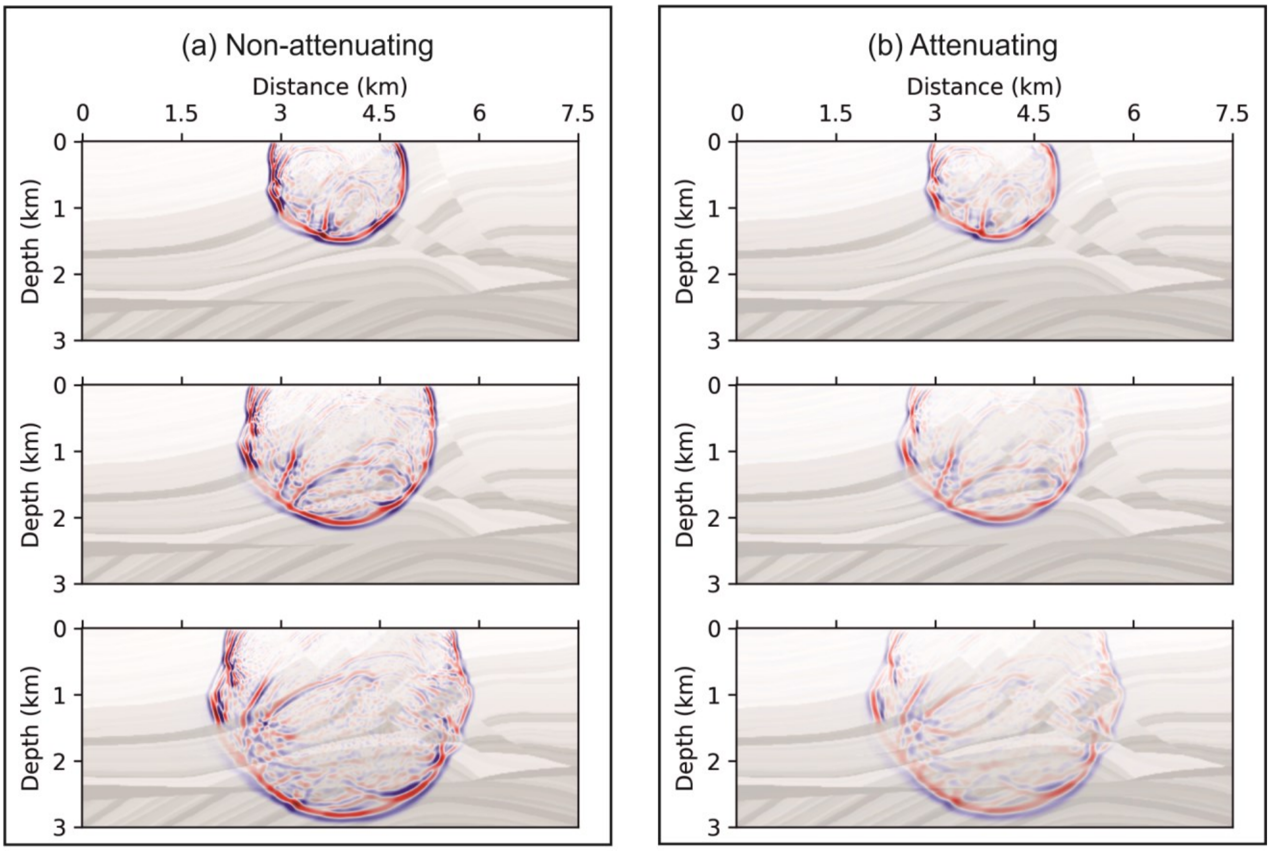


**Figure 4.7** Seismic wave simulation. (a) Snapshots of non-attenuating wavefield at 0.6 s, 0.8 s and 1.0 s. (b) Snapshots of attenuating wavefield at 0.6 s, 0.8 s and 1.0 s.

Figure 4.7 shows snapshots of the wavefield without attenuation and the wavefield with attenuation at 0.6 s, 0.8 s and 1.0 s, respectively. There are no free-surface reflections from the top boundary and other three boundaries, since a convolutional perfectly matched layer (CPML) absorbing condition is adopted in the numerical calculation. However, there are clear reflections from the interfaces within the model, for both cases; this observation indicates the high quality of the simulation with negligible numerical dispersion. More importantly, these snapshots demonstrate that the attenuating wavefields have a clearly delayed wavefront and reduced amplitude, if compared to its non-attenuation counterparts.

Comparison between the non-attenuating and attenuating shot gathers (Figure 4.8a and 4.8b) demonstrates the accumulative effect of attenuation. Moreover, comparison between residuals of the conventional averaging scheme and the corrected scheme with the proposed spatial filter (Figures 4.9a and 4.9b) demonstrates the significance of the spatial filter. The residuals shown in Figure 4.9 are the discrepancy from the Grünwald-Letnikov expansion. Whereas the proposed wave equation is applicable to complex geological models, the reflection events from the interior interfaces are very weak in amplitude.

Table 1 shows the maximum relative error of the layered model and the Marmousi model examples, which again demonstrates that the filtered averaging scheme has better the accuracy than the conventional averaging scheme. The error in Marmousi model is larger than that in layered model, because the Marmousi $\beta$ model is varied in a larger range (from 0.01 to 0.3), thus the average $\bar{\beta}$ approximates all the $\beta(\mathbf{x})$ less effectively. The accurate wave simulation will lead to correct subsurface images from seismic migration, as it leads to correct compensation to the viscoelasticity of the subsurface media

Table 2 compares the computational time of FTD and FSD. The computation time of FTD is increase exponentially along with increasing simulation time, as the wavefield of every timestep needs to be stored and it needs plenty of time saving and reading files. For FSD, the averaging scheme and the correct averaging scheme have the same computational process only with different coefficients, so they have the same computational time. From the comparison, the FSD solver costs much less computational time than the FTD solver, as spatial FFT implementation is extremely efficient, which shows the priority of this method. An efficient numerical solver allows for the application of the generalised viscoelastic wave equation to reverse-time migration.

It should be noted that accounting for viscoelasticity leads to more accurate subsurface images, but only if the correct underlying $Q$ model parameters are specified. Seismic simulation is more sensitive to $Q$ variation in strongly attenuative media. Therefore, further research on building an accurate $Q$ model should be conducted to benefit the seismic simulation and further imaging.

**Table 1** The maximum relative error of the filtered averaging scheme and the conventional averaging scheme

| Model | Conventional | Filtered |
|---|---|---|
| Layered model | 15.12% | 2.94% |
| Marmousi model | 19.38% | 4.11% |

**Table 2** The comparison of computation time in the seismic simulation of the Marmousi model.

| Simulation Time (ms) | FTD | FSD |
|---|---|---|
| 500 | 45 min | 1 min 3 s |
| 1000 | 2 h 51 min | 1min 58 s |
| 2000 | 11 h 48 min | 4 min 1 s |

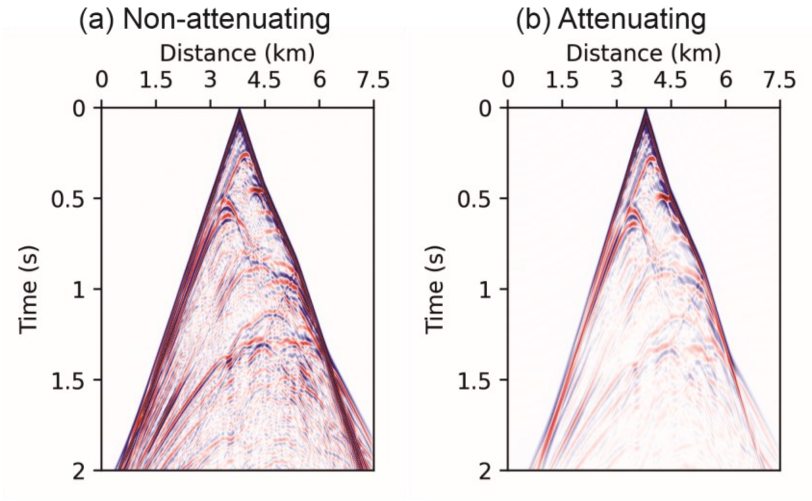


**Figure 4.8** The effect of attenuation in seismic wavefield. (a) The non-attenuating shot gather. (b) The attenuating shot gather, generated by the corrected scheme.

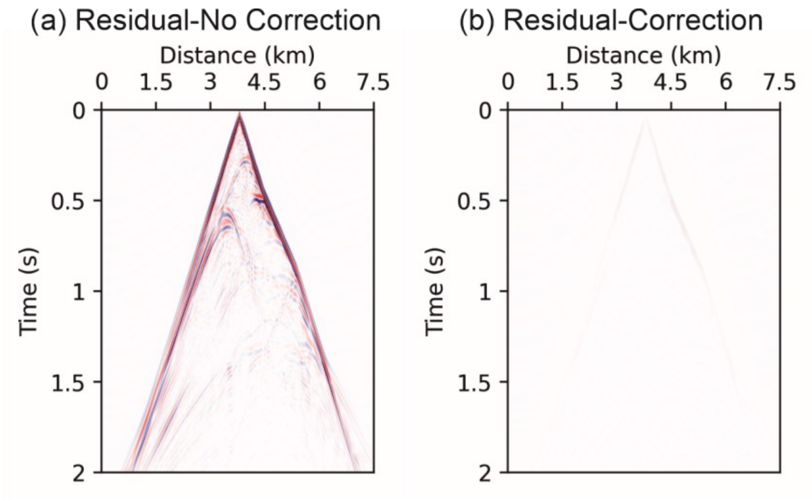


**Figure 4.9** The significance of the correction function. (a) The residual of the conventional averaging scheme. (b) The residual of the corrected averaging scheme. The reference is the solution of Grünwald-Letnikov expansion of FTD.

## 4.6 Attenuation compensation reverse-time migration

Reverse-time migration (RTM) is a seismic imaging technique which produces high quality subsurface images, even in complex geological conditions. The RTM image is generated by cross-correlating the source wavefield and backward propagated receiver wavefield. Due to the associated attenuation effects, velocity dispersion and energy absorption, in real subsurface media, the conventional migration result suffers from weak amplitude and distorted phase, which greatly lowers the resolution and fidelity of the seismic images. Thus, it is important to compensate for these viscoelastic effects during the migration process.

In this section, the proposed viscoelastic wave equation with FSDs is applied to compensate the attenuation effects in RTM. The attenuation-compensated RTM allows the attenuation effect to be mitigated during seismic simulations, to improve the resolution of the seismic images, especially for high-attenuation structures.

In the generalised viscoelastic wave equation with FSDs, Eq. (4.17), the $C_1$ term represent the frequency dispersion and the $C_2$ term represents the amplitude absorption. This decoupled form allows the attenuation compensation to be separated from velocity dispersion. “Switches” to control two effects can be added as:

$$\frac{1}{c^2}\frac{\partial^2 u}{\partial t^2}+\left((-\nabla^2)+S_1(-\nabla^2)^{1+\bar{\beta}/2}C_1 f(\beta)+S_2(-\nabla^2)^{(1+\bar{\beta})/2}C_2 f(\beta)\frac{\partial}{\partial t}\right)u=0\,, \qquad (4.21)$$

where $S_1$ and $S_2$ are two coefficients controlling velocity dispersion and amplitude absorption. If $S_1=0$, Eq. (4.21) becomes absorption-only wave equation, and if $S_2=0$, Eq. (4.21) becomes dispersion-only wave equation.

To intuitively demonstrate the method for compensating the seismic attenuation effects, a simple model with a single horizontal reflector can be considered and seismic rays are adopted to describe the wave propagation.

Velocity dispersion means the high-frequency wave components travel faster than the low-frequency counterparts. As illustrated by Figure 4.10, the high frequencies are recorded earlier than the low frequencies, if they are emitted from the source simultaneously. In backward propagation, the recorded data is reversely ordered, and the low frequencies are propagated prior to high frequencies. If the phase velocity for each frequency is identical to that in the source wavefield propagation, the high frequencies and low frequencies can meet at the source location. This means the $C_1$ term, which controls the phase velocity, should be the same in both source and receiver wavefields, and $S_1 = 1$ should be adopted in both forward and backward propagation.

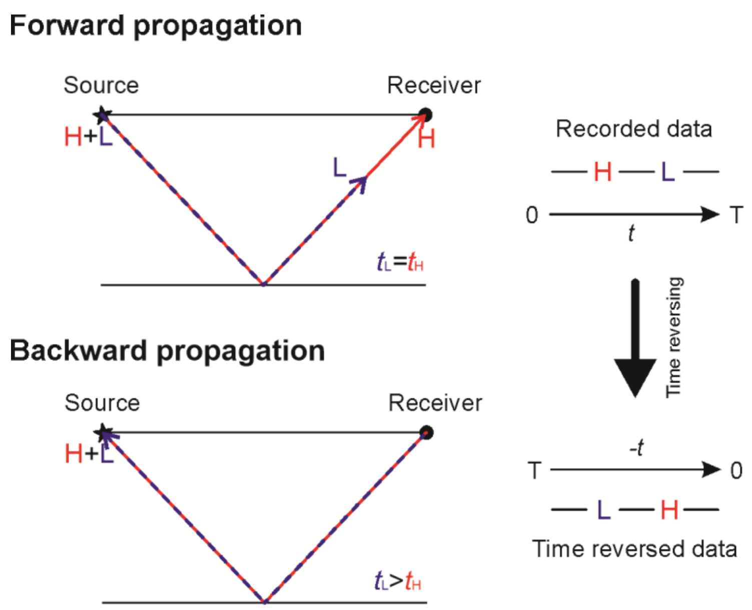


**Figure 4.10** The correction for velocity dispersion. (Top) Forward propagation in attenuating media. (Bottom) Backward propagation with time-reversed data. The labels 'H' and 'L' represent high-frequency and low-frequency waves, and the red solid and blue dashed lines denote the ray path of the high and low frequencies, respectively. "*t*" denotes travel time, and "T" denotes total recording time. To correct the velocity dispersion effects, the dispersion term, controlling the phase velocity of the wave, must remain unchanged.

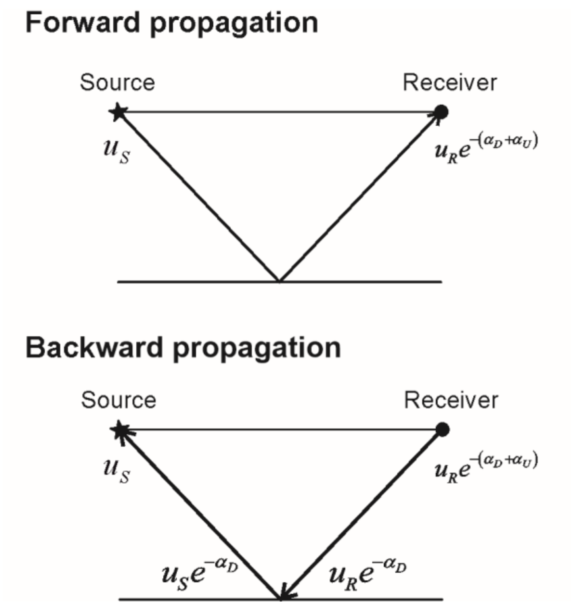


**Figure 4.11** The compensation for energy absorption. (Top) Forward propagation with attenuation. (Bottom) Backpropagation wavefield with compensation. The subscripts '*S*' and '*R*' represent the source and receiver wavefield, and '*U*' and '*D*' represent the down-going and up-going attenuation, respectively. To correct the energy absorption effects, the absorption term must be reversed

Energy absorption represents the intrinsic energy loss in wave propagation. The field and laboratory measurements show that attenuation follows the power law. As illustrated in Figure 4.11, for a single–frequency wave, the attenuation follows a basic power law, and the recorded data contains both down-going and upgoing attenuation. To compensate for the energy loss in the receiver wavefield, the amplitude should be amplified to the exact same scale as the forward propagation, to restore the lost energy. Thus, in the wave equation, the sign of the energy absorption term should be reversed, which means $S_2 = -1$ in backward propagation.

For the simulation of the source wavefield, it is proposed to use the dispersion-only wave equation, $S_2 = 0$, so the wave equation becomes

$$\frac{1}{c^2}\frac{\partial^2 u}{\partial t^2}+\left((-\nabla^2)+(-\nabla^2)^{1+\bar{\beta}/2}C_1 f(\beta)\right)u=0. \tag{4.22}$$

The reason is that this forward modelling does not include attenuation, and it is equivalent to compensating the wavefield. Also, the smaller number of calculations for the fractional spatial derivatives increases the efficiency. It is worth mentioning that some study suggests amplifying the amplitude in the source wavefield, i.e., $S_2=-1$, which means the total wave energy is increasing during the propagation and it is obviously unphysical.

In the receiver wavefield, the amplitude loss in the recorded original data is compensated by setting $S_2=-1$. Therefore, the attenuation-compensation wave equation used in receiver wavefield propagation is written as

$$\frac{1}{c^2}\frac{\partial^2 u}{\partial t^2}+\left((-\nabla^2)+(-\nabla^2)^{1+\bar{\beta}/2}C_1 f(\beta)-(-\nabla^2)^{(1+\bar{\beta})/2}C_2 f(\beta)\frac{\partial}{\partial t}\right)u=0. \tag{4.23}$$

It should be noted that during the attenuation compensation, the high-frequency noise will be exponentially amplified, which will cause numerical instability. So, low-pass filters in the wavenumber domain should be applied to suppress the noise. The imaging condition is the source-normalized cross-correlation between source and receiver wavefields, which has been proven to be capable of illustrating the real reflector and to be numerically stable.

To validate the attenuation compensation, the same Marmousi model (Figure 4.6) is adopted to demonstrate the RTM scheme. There are 70 Ricker wavelet sources with a peak frequency of 20 Hz. The shot interval is 100 m, whereas the receiver spacing is 10 m with a total of 751 receivers. The synthetic data are generated by the forward modelling and recorded for a total time of 4 s, and the sampling rate is 1 ms. The direct waves are muted from the data. A Tukey filter with taper ratio of 0.2 and cut-off frequency of 120 Hz is applied to prevent high-frequency wave component from growing exponentially. Laplacian filters are applied to

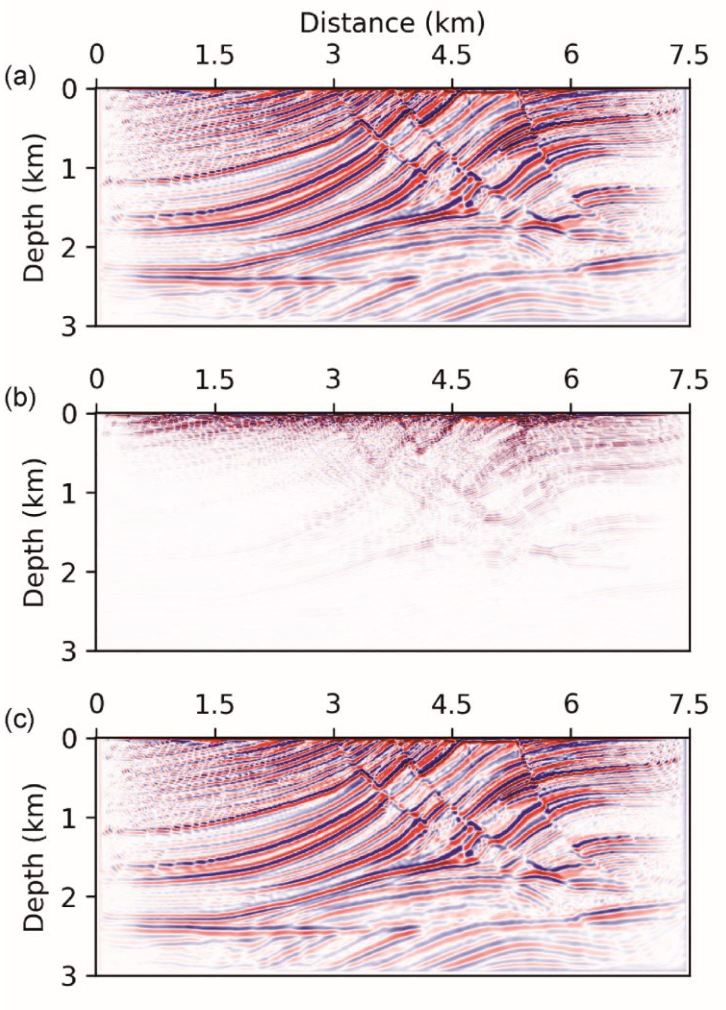


**Figure 4.12** Reverse-time migration (RTM). (a) The reference RTM image (the conventional RTM by using the non-attenuation data). (b) The conventional RTM (without compensation) by using the attenuation data. (c) Attenuation-compensated RTM with the attenuation data.

remove the low-wavenumber artefacts in the final image. The final images are normalized by the maximum value to better compare the results.

Figure 4.12 shows the resultant RTM images. The reference is set as the conventional reverse-time migration by using the non-attenuating data (Figure 4.12a). Compared to the reference image, the overall amplitude in the non-compensated image (Figure 4.12b) is much weaker, the interfaces located at the lower part of the model are poorly illuminated and the anticlined structure beneath the high-attenuation zone is almost invisible in the non-compensated image. With attenuation compensation (Figure 4.12c), the interfaces and structures are correctly located and better illuminated, and this compensated result is very similar to the reference.

Figure 4.13 compares the image traces at difference lateral distance. Compared with the reference (black line), which is the conventional RTM image of the non-attenuation data, directly using conventional RTM to attenuation data (green line) leads to inaccurate phase and low resolution, especially in the deeper part of the result. The attenuation-compensated RTM (red line) can compensate for the weak amplitude and correct phases, appropriately. This example shows the attenuation compensation can effectively compensate for the weakened amplitude and distorted phase in reverse-time migration, leading to the improvement of the resolution of seismic images.

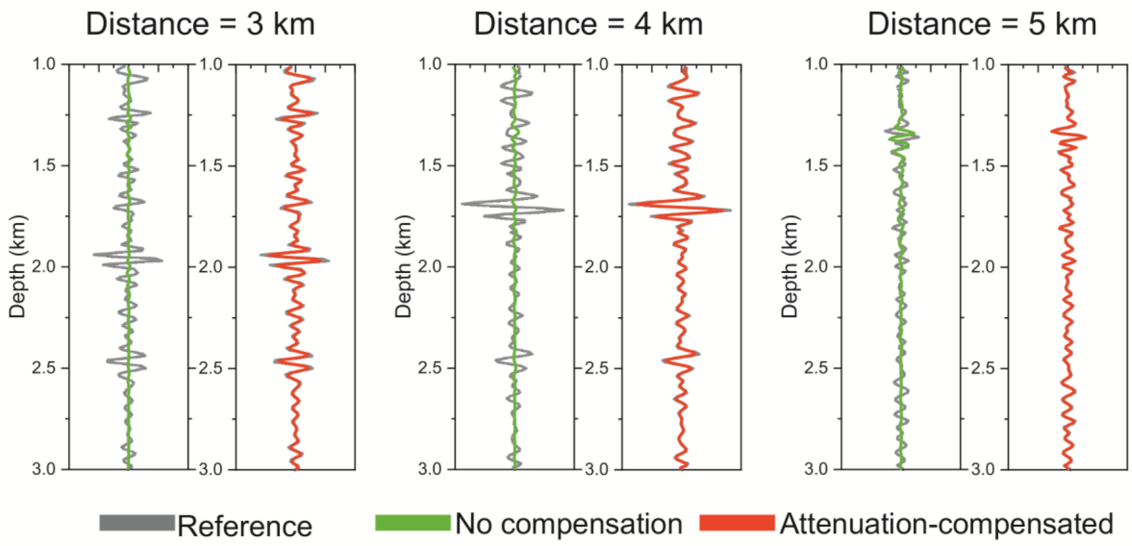


**Figure 4.13** Seismic image traces at 3 km, 4 km, and 5 km. The black line represents the reference traces; the green line is obtained by the conventional RTM of attenuation data, and the red line is obtained by attenuation-compensated RTM of attenuation data.

## 4.7 Conclusion

The generalised wave equation with FTD is numerically challenging to solve and not suitable for reverse-time migration. In this chapter, an efficient implementation strategy is proposed. When transferring the wave equation in the FTD form to the FSDs form, the wave simulation can be implemented via FFT to the wavenumber domain. This FFT implementation greatly improves the computation efficiency, but it causes errors when applied to heterogeneous media. To improve the accuracy of this implementation, it is proposed to insert a frequency-independent correction function into the wave equation as a spatial filter to correct for the error caused by the heterogeneity of the model. This spatial filter can be easily implemented and an equation including the correction improves the accuracy of the simulation. Numerical examples have demonstrated that this strategy may properly represent the dissipation effect of the viscoelasticity on the waveforms, improve accuracy, and maintains the high efficiency of the FFT implementation. With efficient and accurate seismic modelling, the attenuation compensation is implemented in reverse-time migration. Thanks to the decoupling effect of the FSDs, the energy absorption and phase distortion can be compensated separately. The numerical migration result demonstrates that attenuation compensation is capable of amplifying the energy and correcting the distorted phase, subsequently improving the resolution and fidelity of the migration images.

# Chapter 5

# Reverse-time migration by biaxial wavefield decomposition

In the previous chapter, an efficient and accurate equation for viscoelastic waves was derived and used in attenuation compensation in reverse-time migration (RTM). In this chapter, another strategy to improve the resolution of migration images is proposed, namely the reduction of migration artefacts. Conventional RTM images are extremely contaminated by artefacts. Therefore, the main objective of this chapter is to investigate an efficient artefacts elimination method for reverse-time migration to generate high-resolution seismic images. In this chapter, the biaxial wavefield decomposition is introduced, which is based on the analytical wavefield via the Hilbert transform and decomposes seismic wavefields in both lateral and vertical directions. After decomposition, the up-going source wavefield and down-going receiver wavefield are eliminated to reduce shallow artefacts. The remaining four terms can contribute separately to imaging flat layer and tilted interfaces. With the separate terms, the remaining artefacts can be easily identified and reduced. The resolution can be further improved by adjusting the weights of the four terms. This Hilbert transform method has been shown to be suitable for the viscoelastic wave equation with fractional spatial derivatives. Therefore, this biaxial wavefield decomposition method is suitable for decomposing wavefields for the attenuation compensation RTM. The decomposed and recombined migration results can better image the complex structure of the subsurface with high resolution.

## 5.1 Introduction

In the reservoir areas with high attenuation media and complex structures, traditional migration methods based on geometry seismology or one-way wave equations is inadequate to provide high-fidelity seismic images. Reverse-time migration (RTM) (Baysal *et al.* 1983, McMechan 1983), based on two-way wave equation, becomes one of the most popular seismic migration techniques because of its ability to image complex subsurface structure without dip limitation. The quality of the migration result is often characterized by resolution of the image. High-resolution seismic images can provide accurate locations and clear patterns of subsurface structures, which greatly benefit the subsequent seismic interpretation.

Reverse-time migration uses the zero-lag cross correlation between the source wavefield, which is to forward propagate the source signature, and the receiver wavefield, which is to backward propagate the recorded data, and generates the high-resolution image. Conventional RTM images are contaminated by the undesirable high-amplitude, low-spatial frequency artefacts, because it uses a two-way wave equation to propagate both source and receiver wavefields and the cross-correlation between the irrelevant and unphysical waves causes the false images. Especially for fine layers, faults, and small structures where the seismic reflection is relatively weak, the resolution is greatly decreased due to the migration artefacts. Therefore, in recent years, improving the resolution of the migration images and reducing artefacts have drawn more attention.

Many studies have attempted to address this RTM artefact issue. Fletcher *et al.* (2006) introduced a directional damping method to reduce the low-frequency noise by suppressing the internal reflection. Zhang & Sun (2009) proposed the use of angle domain common gathers

(ADCIGs) and to reduce the noise by muting the far angles. A straightforward and practical approach is to apply Laplacian filters to the final image, but this approach is unphysical and damages the true image of structures (Guitton *et al*. 2007). A more physical way is to perform the up-/ down-going wave decomposition during the propagation and only cross-correlate the physical wave components in the imaging condition, such as between the down-going source wavefield and the up-going receiver wavefield.

One category for the up/down going wavefield decomposition is to use the Poynting vector as an indicator for the wave decomposition, as it is represented the direction of wave energy propagation (Yoon & Marfurt 2006). Further, the Poynting vector method has been improved by Horn-Schunck optical flow algorithm (Zhang 2014), and weight function illumination (Kim *et al.* 2019). This type of method achieved good results in simple models, but it fails to generate satisfying results in complex subsurface models, because the discontinuous separated waveforms bring noise to the migration image.

Another category for up/down going wavefield decomposition is based on the sign of the apparent propagation velocity. This involves filtering the wavefield in the frequency-wavenumber domain. This method obtains relatively high-quality migration images, but the computational cost is extremely large because calculating frequency needs storge of the entire wavefield history. Therefore, to avoid this computational memory problem, the analytical wavefield method is developed based on the Hilbert transform that the real part is the original wavefield and the imaginary part is the Hilbert transform of the real part (Fei *et al.* 2015). Because the analytical wavefield only contains non-negative frequency components, the up/down going wavefield decomposition can be conveniently implemented via spatial Fourier transform in terms of depth. In recent years, various studies on this analytical wavefield have been conducted. Shen & Albertin (2015) proposed to construct the imaginary part of the analytical wavefield by applying the temporal Fourier transform to the source term in the acoustic wave equation and following the conventional propagation process. This method has been tested and proved to be effective and efficient in removing low-frequency artefacts.

The existing studies on the wavefield decomposition only focus on the up-down going wave decomposition, which ignores the artefacts caused by incorrect correlation between left-/right-going waves. This chapter introduced the biaxial wavefield decomposition that further decomposed the wavefield into four directions, the four terms have different contributions to imaging the flat and tilted layers, respectively, and the artefacts can be further identified and filtered as the four terms are decoupled. Also, since the tilted faults and layers are separated from nearly flat layers, the resolution can be further improved by adjusting weights. Additionally, it is proven that this biaxial wavefield decomposition method based on the Hilbert transform is suitable for the viscoelastic wave equation with fractional spatial derivatives, and subsequently applicable to attenuation compensation RTM. This strategy may provide further guidance for seismic interpretation and subsequent exploration. This chapter has been submitted to *Geophysics*.

## 5.2 Artefacts in reverse-time migration

RTM is an advanced developed technique for imaging subsurface geological and velocity complexities. The zero-lag cross-correlation between extrapolated source wavefields and back-propagated receiver wavefields is the commonest imaging condition(Claerbout 1971). Since both source and receiver wavefields contain up- and down-going wave components, the cross-correlation imaging condition can be mathematically partitioned in a discrete form:

$$\mathbf{I} = \sum_t \mathbf{S}^T \mathbf{R} = \sum_t S_d R_d + S_d R_u + S_u R_d + S_u R_u \,, \tag{5.1}$$

where $\mathbf{S} = \left(S_d, S_u\right)^T$ and $\mathbf{R} = \left(R_d, R_u\right)^T$ denotes the source and receiver wavefield and subscript *d*, *u* denote the down-going and up-going, respectively. In Eq. (5.1), $S_d R_d$ and $S_u R_u$

produces high-amplitude and low-frequency artefacts in the shallow part, while $S_u R_d$ is the upward-folded ray-path result that has the same travel time of the true physical ray path, which generate incorrect RTM images.(F. Liu *et al.* 2011, W. Wang *et al.* 2016). Therefore, a causal imaging condition (Fei *et al.* 2015, Revelo & Pestana 2019) is proposed by only maintaining a single term in Eq. (5.1) as

$$\mathbf{I}_{\text{causal}} = \sum_t S_d R_u \, . \tag{5.2}$$

However, this causal imaging condition ignores the artefacts produced by the unphysical cross-correlation of the incident and reflected waves from incorrect lateral directions. To demonstrate this statement specifically, the ray path of a horizontal layer reflector (Figure 5.1) may be considered. The cross-correlation imaging condition of RTM will ideally enhance the true reflection point *O*, but cause artefacts *O'* along the ellipse whose focus points are the source and receiver. With the superposition of different receiver wavefields and multiple shots, the artefacts may become large and hinder the true migration image.

If the wavefield decomposition can be performed in terms of both lateral and vertical direction, the artefacts can be further reduced. The zero-lag cross-correlation imaging condition (Eq. 5.1) may be written in a matrix form as:

$$\mathbf{I} = \sum_t \mathbf{S}^{\mathrm{T}} \mathbf{R} = \sum_t \left( S_d^r, S_d^l, S_u^l, S_u^r \right) \left( R_d^r, R_d^l, R_u^l, R_u^r \right)^{\mathrm{T}} , \tag{5.3}$$

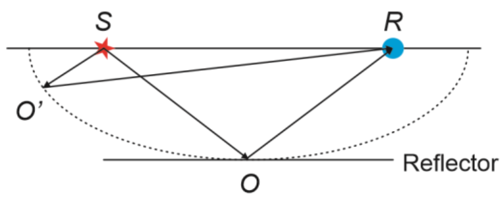


**Figure 5.1** The imaging condition of RTM will ideally enhance the reflection point but cause artefacts along the ellipse. The red star (*S*) represents the source, the blue dot (*R*) denotes the receiver, *O* denotes the true reflection point and *O'* denotes the artefacts.

where $\mathbf{S}=\left(S_d^r, S_d^l, S_u^l, S_u^r\right)^{\mathrm{T}}$ and $\mathbf{R}=\left(R_d^r, R_d^l, R_u^l, R_u^r\right)^{\mathrm{T}}$ denotes the source and receiver wavefield and the superscript *l*, *r* denote the left-, right- going waves and the subscript *d*, *u* denote the down- and up- respectively. This form of imaging condition is equivalent to the summation of 16 terms. To adjust the flexibility, a coefficient matrix **W** may be added as

$$\mathbf{I}=\sum_t \mathbf{S}^{\mathrm{T}}\mathbf{W}\mathbf{R}=\sum_t\left(S_d^r, S_d^l, S_u^l, S_u^r\right)\begin{pmatrix} w_{S1}w_{R1} & w_{S1}w_{R2} & w_{S1}w_{R3} & w_{S1}w_{R4} \\ w_{S2}w_{R1} & w_{S2}w_{R2} & w_{S2}w_{R3} & w_{S2}w_{R4} \\ w_{S3}w_{R1} & w_{S3}w_{R2} & w_{S3}w_{R3} & w_{S3}w_{R4} \\ w_{S4}w_{R1} & w_{S4}w_{R2} & w_{S4}w_{R3} & w_{S4}w_{R4} \end{pmatrix}\begin{pmatrix} R_d^r \\ R_d^l \\ R_u^l \\ R_u^r \end{pmatrix}, \quad (5.4)$$

where in the coefficient matrix **W**, the subscripts *S*, *R* denote the source and receiver and the subscripts 1,2,3 and 4 denote the right-down, left-down, left-up and right-up going waves, respectively. Conventional cross-correlation imaging condition is equivalent to that all the elements in **W** are 1/16. The causal imaging condition (Eq. 5.2) is equivalent to “switching off” the up-going source wavefield and the down-going receiver wavefield, and the coefficient matrix becomes:

$$\mathbf{W}_{\text{causal}}=\frac{1}{4}\begin{pmatrix} 0 & 0 & 1 & 1 \\ 0 & 0 & 1 & 1 \\ 0 & 0 & 0 & 0 \\ 0 & 0 & 0 & 0 \end{pmatrix}. \quad (5.5)$$

The coefficient 1/4 in Eq. (5.5) is for normalization. To add extra flexibility, the weights of four term may be introduced, and the coefficient matrix can be revised as

$$\mathbf{W}_{\text{deco}}=\begin{pmatrix} 0 & 0 & W_3 & W_4 \\ 0 & 0 & W_1 & W_2 \\ 0 & 0 & 0 & 0 \\ 0 & 0 & 0 & 0 \end{pmatrix}, \quad (5.6)$$

where $W_i$ denotes the weight coefficient to balance the four terms, with the constraint $\sum_{i=1}^{4} W_i = 1$.

Assigning weights to different terms may illuminate some fine structures. The imaging condition Eq. (5.6) can be simplified as:

$$I_{\text{deco}}(\mathbf{x}) = W_1 \sum_t S_d^l(\mathbf{x}) R_u^l(\mathbf{x}) + W_2 \sum_t S_d^l(\mathbf{x}) R_u^r(\mathbf{x}) + W_3 \sum_t S_d^r(\mathbf{x}) R_u^l(\mathbf{x}) + W_4 \sum_t S_d^r(\mathbf{x}) R_u^r(\mathbf{x}) \quad (4.7)$$

where $S_d^l(\mathbf{x})R_u^l(\mathbf{x})$ and $S_d^r(\mathbf{x})R_u^r(\mathbf{x})$ denotes the single-directional terms, as the source wavefield and receiver wavefield propagate to the same lateral direction; $S_d^l(\mathbf{x})R_u^r(\mathbf{x})$ and $S_d^r(\mathbf{x})R_u^l(\mathbf{x})$ denotes the cross-directional term, as the source and receiver wavefield propagate to the opposite lateral directions. The decomposition term images can provide a further reference in addition to the conventional RTM. Noted that the imaging condition Eq. (5.7) is suitable for the source and receivers placed on the near surface, and the coefficient matrix (5.6) may be revised according to the acquisition design.

In Eq. (5.7), the weights $W_i$ can be assigned based on numerical inversion. In this chapter, it is proposed to match the structural similarity index of the combined image (Eq. 5.7) with that of the conventional RTM image (Eq. 5.1). Structural similarity index is a statistical property of a image, which is based on the distribution and overall variation. If directly matching the overall residual with the conventional RTM which presents large amplitude artefacts, the weights of the artefact terms will be large and the amplitude of the remaining artefacts will be greatly amplified.

To demonstrate the artefacts produced by the wrong cross-correlation between irrelevant wave components, a simple flat-layer model (Figure 5.2a) is constructed. The 24 shots and the receivers are in the depth of 300m. The wavefield decomposition method is discussed in the next section. Figure 5.2(b) is the conventional RTM image from the cross-correlation of full source and receiver wavefield, where there are large artefacts in the shallow part of the image. After decomposition, the artefacts in Figure 5.2(c) are greatly reduced compared with the conventional RTM algorithm. More importantly, this example shows that only the single-directional terms contribute to the true image of the layer, while the cross-directional terms ($S_d^r R_u^l + S_d^l R_u^r$) introduce artefacts in the flat-layer case. This example demonstrates that for the horizontal reflectors, the single-directional terms are able to show the flat layer, while the artefacts are often presented in the cross-directional terms. Therefore, by selecting appropriate terms for the imaging condition, the biaxial wavefield decomposition can further reduce the RTM artefacts and subsequently improve the resolution of the images.

Even though the cross-directional terms are the artefacts in the flat-layer area, they contribute to better image faults and tilted layers. As shown in the schematic diagram of the ray path of a tilted layer (Figure 5.3), for small offset data where the quality of the migration image is better, the cross-correlation between left-down going source wavefield $S_d^l$ and right-up going receiver wavefield $R_u^r$ in this case can show the true layer. By separating these terms, the fault and tilted layers may be separated from the flat layers.

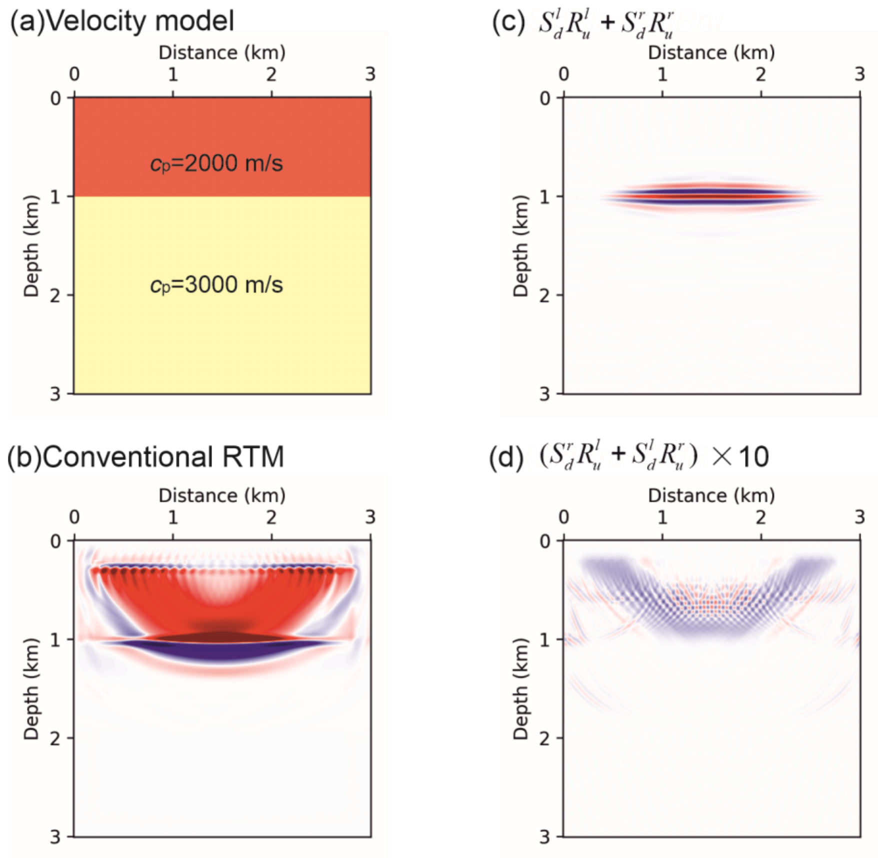


**Figure 5.2** A flat layer example. (a) The velocity model; (b) conventional RTM with cross correlation imaging condition; (c) $S_d^l R_u^l + S_d^r R_u^r$ image; (c) $S_d^r R_u^l + S_d^l R_u^r$ image.

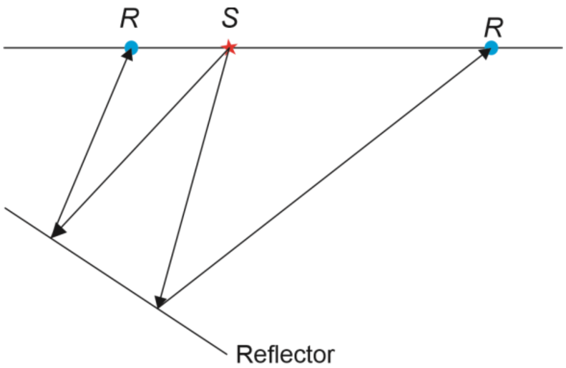


**Figure 5.3** Seismic wave ray path of a tilted reflector at small offset receivers. The correlation between down-left going source wavefield and up-right going receiver wavefield represent accurate reflection points. *S* denotes the source, and *R* denotes the receiver.

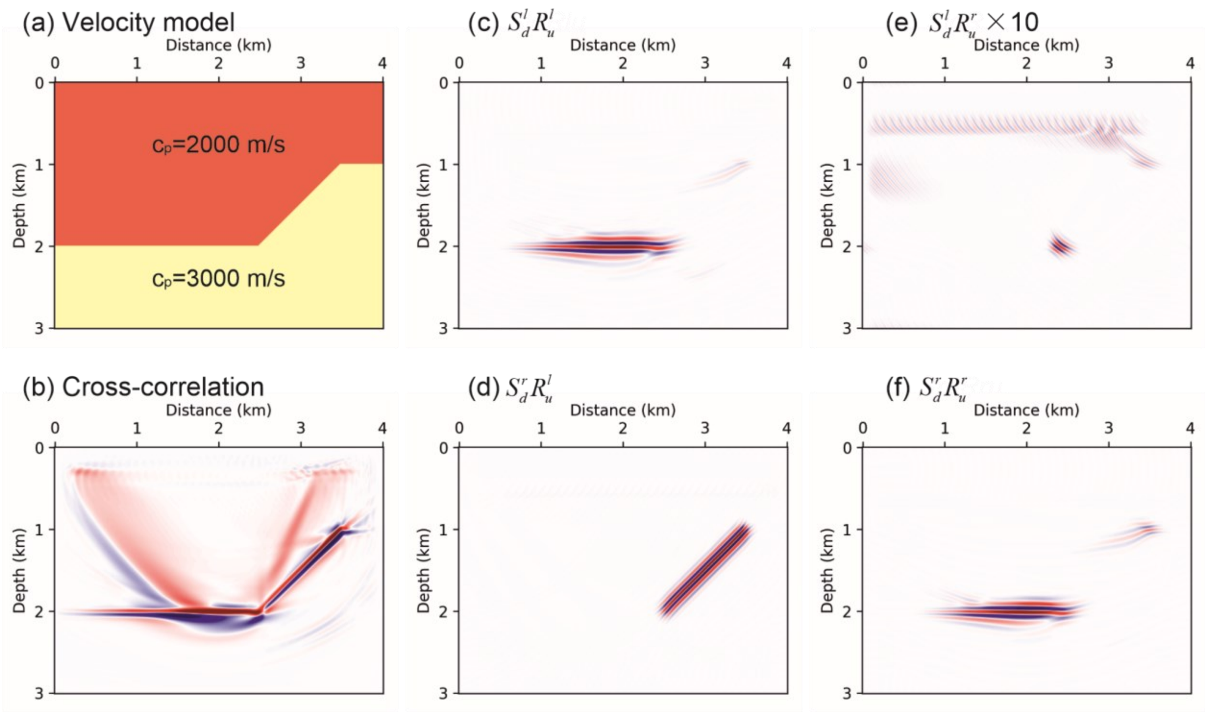


**Figure 5.4** A simple fault example. (a)The velocity model; (b) conventional RTM with cross-correlation imaging condition; (c) $S_d^l R_u^l$ image; (d) $S_d^r R_u^l$ image; (e) $S_d^l R_u^r$ image; (f) $S_d^r R_u^r$ image.

To demonstrate the contribution of each term in Eq. (5.7), a simple fault model is built (Figure 5.4a). The large artefacts in the conventional RTM image (Figure 5.4b) are not shown in the decomposition results (Figures 5.4c-5.4f). Additionally, the single-directional images, $S_d^l R_u^l$ and $S_d^r R_u^r$ (Figures 5.4c and 5.4f), show the correct image of the flat layer, and the upper-left part of the image is from the scattering waves of the corner. The $S_d^r R_u^l$ term (Figure 5.4d) shows the tilted fault with high resolution, while the $S_d^l R_u^r$ term (Figure 5.4e) is mainly artefact. This example shows that the four terms in the imaging condition play different roles in presenting the subsurface layers. The single-directional terms are capable of imaging the nearly flat layers, while the cross terms can image the faults and large tilted layers.

## 5.3 Biaxial wavefield decomposition

The decomposed wave components in Eq. (5.7) are separated according to the apparent propagation velocities along both $x$ and $z$ axis (Hu & McMechan 1987). The apparent velocities are calculated using the dispersion relation, which requires frequency and corresponding wavenumber components. However, calculating the frequency requires to complete wave propagation and the whole wavefield snapshot being stored, which is computationally intensive.

Building the analytical wavefield is an effective way to avoid calculating frequency in wavefield decomposition. An analytical signal is constructed by using the original real-valued seismic trace as the real part, and the Hilbert transform of the original trace as the imaginary part. Figure 5.5 shows a 20-Hz Ricker wavelet, which has a symmetric amplitude spectrum in the frequency domain (Figure 5.5a). After the Hilbert transform, the amplitude spectrum keeps unchanged, with only a 90° phase shift to the original trace (Figure 5.5b). The complex trace is built by the original wavelet and its Hilbert transform (Figure 5.5c), whose amplitude spectrum is zero at the negative frequency and double at positive frequency.

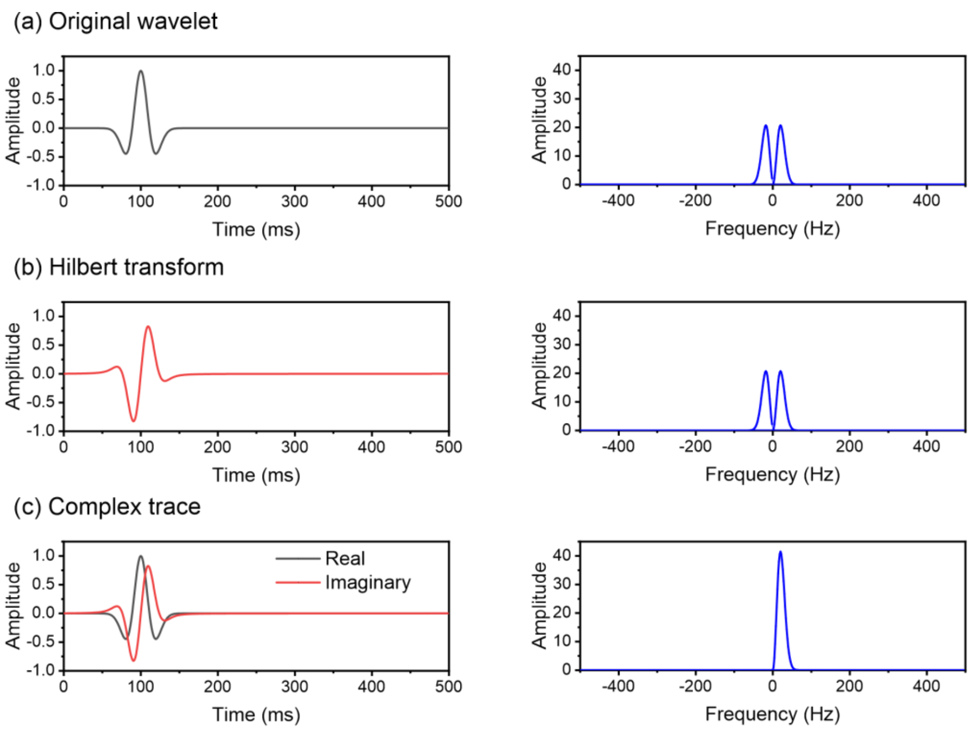


**Figure 5.5** Complex trace and its spectrum. (a) The original 20-Hz Ricker wavelet and its amplitude spectrum; (b) the Hilbert transform of (a) and its corresponding amplitude spectrum; (c) the complex trace and its amplitude spectrum.

To build the analytic wavefield, the scalar viscoelastic wave equation (Xu & Wang 2022) with source term can be considered as

$$\frac{1}{c^2}\frac{\partial^2 p}{\partial t^2}+\left((-\nabla^2)+(-\nabla^2)^{1+\beta/2}C_1+(-\nabla^2)^{(1+\beta)/2}C_2\frac{\partial}{\partial t}\right)p=f(t)\delta(x-x_0)\delta(z-z_0) \tag{5.8}$$

where $p$ is the scalar wavefield, $\beta$ is the viscoelastic parameter, $c$ is the viscoelastic velocity, $(x_0, z_0)$ is the source location, and $f(t)$ is the source function, and the two coefficients are

$$\begin{aligned} C_1 &= \beta\left(\frac{c_0}{\omega_0}\right)^{\beta}\cos\frac{\beta\pi}{2}, \\ C_2 &= \frac{\beta}{\omega_0}\left(\frac{c_0}{\omega_0}\right)^{\beta-1}\sin\frac{\beta\pi}{2}, \end{aligned} \tag{5.9}$$

and $c_0$ is the reference velocity which usually set as pure acoustic velocity, $\omega_0$ is the reference frequency which set as highest frequency of the frequency band normally (Y. Wang & Guo 2004b).

Performing the Hilbert transform along the time axis for both sides in Eq. (5.8), it becomes:

$$\frac{1}{c^2}\mathcal{H}_t\left(\frac{\partial^2 p}{\partial t^2}\right)+\mathcal{H}_t\left[\left((-\nabla^2)+(-\nabla^2)^{1+\beta/2}C_1+(-\nabla^2)^{(1+\beta)/2}C_2\frac{\partial}{\partial t}\right)p\right]=\mathcal{H}_t\left(f(t)\delta(x-x_0)\delta(z-z_0)\right), \tag{5.10}$$

where $\mathcal{H}_t(\cdot)$ denotes the Hilbert transform in terms of time. Using the linear property of Hilbert transform and derivatives and the independence of different variables, the above equation becomes:

$$\frac{1}{c^2}\frac{\partial^2\mathcal{H}_t(p)}{\partial t^2}+\left((-\nabla^2)+(-\nabla^2)^{1+\beta/2}C_1+(-\nabla^2)^{(1+\beta)/2}C_2\frac{\partial}{\partial t}\right)\mathcal{H}_t(p)=\mathcal{H}_t\left(f(t)\right)\delta(x-x_0)\delta(z-z_0), \tag{5.11}$$

Combining Eqs. (5.8) and (5.11) together, it satisfies a similar equation:

$$\frac{1}{c^2}\frac{\partial^2\hat{p}}{\partial t^2}+\left((-\nabla^2)+(-\nabla^2)^{1+\beta/2}C_1+(-\nabla^2)^{(1+\beta)/2}C_2\frac{\partial}{\partial t}\right)\hat{p}=\hat{f}(t)\delta(x-x_0)\delta(z-z_0). \tag{5.12}$$

where $\hat{p}=p+\mathcal{H}_t(p)$ is the analytic wavefield, and $\hat{f}(t)=f(t)+\mathcal{H}_t\left[f(t)\right]$ is the analytic source. Thus, the analytical wavefield can be built at every time step, where the frequency is non-negative.

The physical meaning of Eq. (5.12) is that for a certain frequency of wave, the velocity dispersion effect for the real and imaginary part of the wavefield is the same and the real and imaginary wavefields have a constant 90-degree phase shift during the propagation. The attenuation compensation in RTM of Eq. (5.12) is straightforward, which keeps the frequency dispersion term ($C_1$ term) unchanged but reverses the sign of the energy absorption term ($C_2$

term) (Zhu, *et al.*, 2014). Since the imaginary wavefield is a constant phase-shifted propagation process, it can also be compensated via the same approach.

Since the calculation of the fractional spatial derivatives requires 2D Fourier transforms in terms of $x$ and $z$ directions, it is convenient to separate the wavefield in both lateral and vertical direction as:

$$P_d^r\left(t,k_x,k_z\right)=\begin{cases}\hat{P}\left(t,k_x,k_z\right) & \text{if } k_z \geq 0 \ \&\& \ k_x \geq 0 \\ 0 & \text{otherwise}\end{cases}, \tag{5.13a}$$

$$P_d^l\left(t,k_x,k_z\right)=\begin{cases}\hat{P}\left(t,k_x,k_z\right) & \text{if } k_z \geq 0 \ \&\& \ k_x < 0 \\ 0 & \text{otherwise}\end{cases}, \tag{5.13b}$$

$$P_u^r\left(t,k_x,k_z\right)=\begin{cases}\hat{P}\left(t,k_x,k_z\right) & \text{if } k_z < 0 \ \&\& \ k_x \geq 0 \\ 0 & \text{otherwise}\end{cases}, \tag{5.13c}$$

$$P_u^l\left(t,k_x,k_z\right)=\begin{cases}\hat{P}\left(t,k_x,k_z\right) & \text{if } k_z < 0 \ \&\& \ k_x < 0 \\ 0 & \text{otherwise}\end{cases}. \tag{5.13d}$$

where $P$ denote the scalar wavefield in the wavenumber domain, $\hat{P}$ is the analytical wavefield in the wavenumber domain, and $(k_x, k_z)$ are wavenumber components.

To test the performance of the wavefield decomposition, a homogeneous model with the centre-located source is built (Figure 5.6). The wavefield is decomposed into four directions according to Eq. (5.13). A Hann window is applied in the wavenumber domain to avoid the Gibbs phenomenon. One potential problem of the decomposed wave is the limited aperture, as the vertically propagated waves are weakened. This problem can be solved by the superposition of multi-shots, and only effects the deep boundary area of the migration image. This limited aperture problem may be compensated by the gradient of the conventional RTM results, which is the secondary product of decomposition RTM.

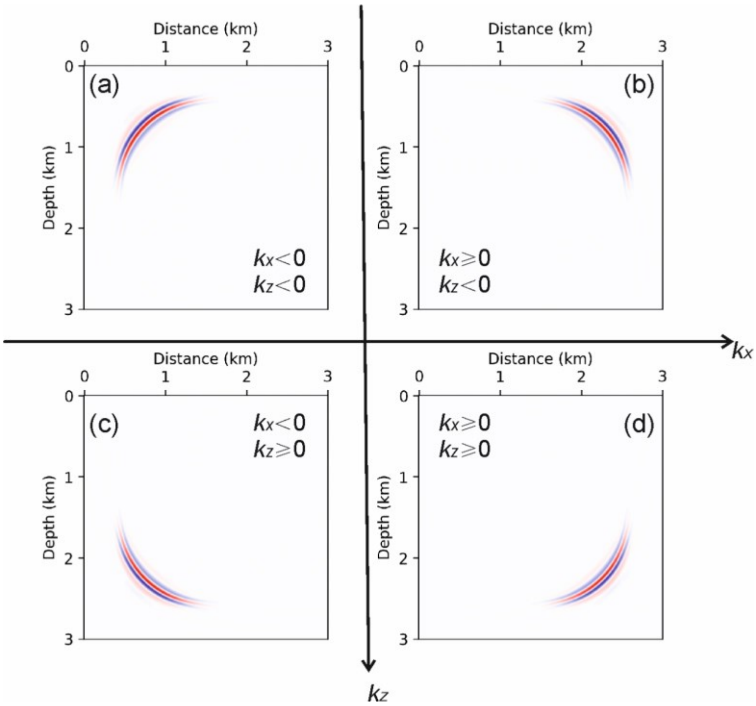


**Figure 5.6** The wavefield decomposition results based on the sign of the wavenumber. (a) Left-up going wave; (b) right-up going wave; (c) left-down going wave; (d) right-down going wave.

## 5.4 Synthetic non-attenuating RTM in Marmousi model

This section aims to test the validity of the biaxial wavefield decomposition reverse-time migration. The purely acoustic data is generated to eliminate the potential effect of viscoelasticity, for validation of the applicability of this method itself.

Figure 5.7(a) shows the velocity model of the fault area in the Marmousi model. Based on a profile through the North Quenguela, the Marmousi model contains multiple fine layers and large faults. Therefore, this model is chosen for testing the biaxial wavefield decomposition RTM method, which is proposed to better image fine layers and large tilted faults. There are 70 shots and 710 receivers both located in the depth of 300m. The migration model is obtained by smoothing the true velocity model.

Figure 5.7(b) presents the conventional RTM result, where the large artefacts significantly hinder the presentation of thin layers and faults. Applying the Laplacian filter (Figure 5.7c) can greatly reduce the low-frequency artefact, but it is only a nonphysical imaging process, and the continuous layers are damaged and broken. Also, the Laplacian filter changes the phase information of the migration image.

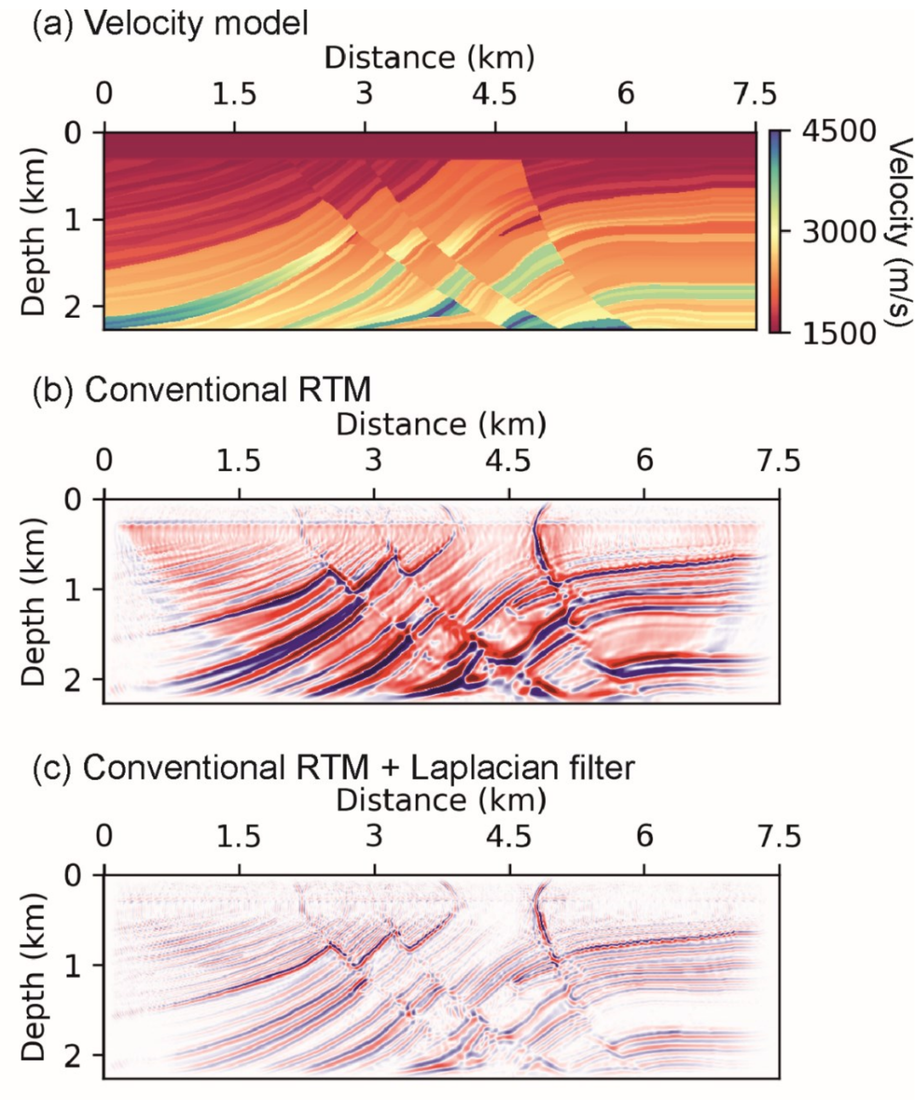


**Figure 5.7** The fault area in the Marmousi model. (a) The velocity model; (b) the conventional RTM image; (c) the conventional RTM image with a Laplacian filter.

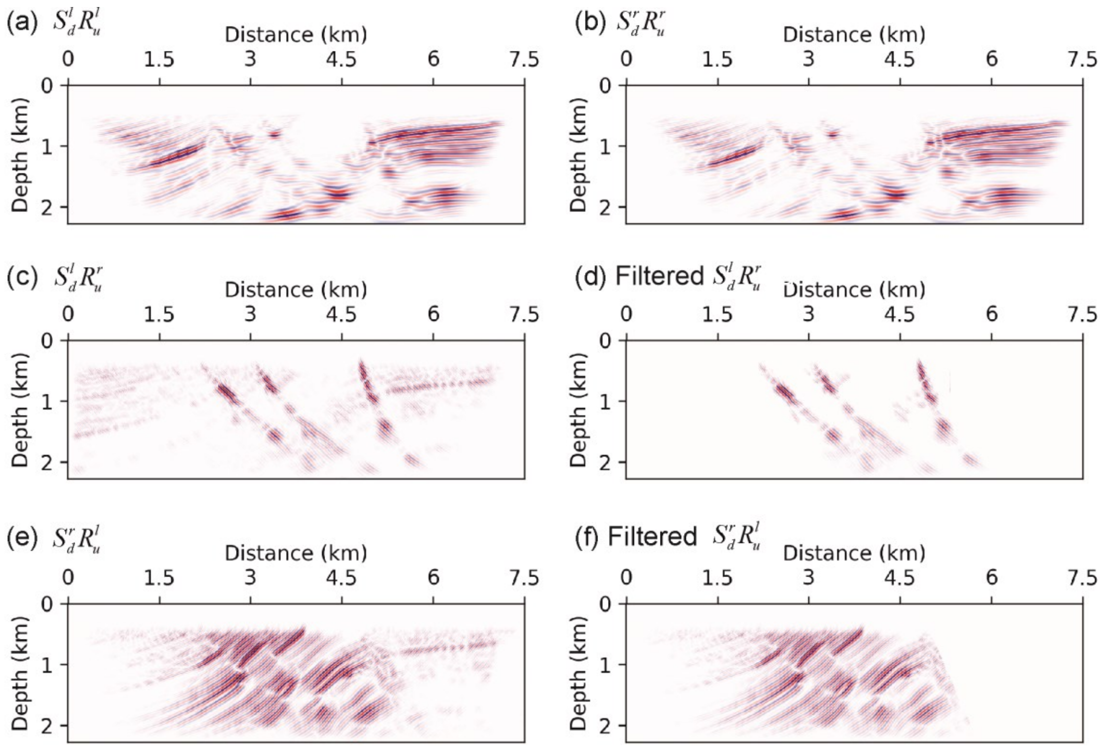


**Figure 5.8** The four decomposed terms in the Marmousi example. (a) $S_d^l R_u^l$ ; (b) $S_d^r R_u^r$ ; (c) $S_d^l R_u^r$ ; (d) filtered $S_d^l R_u^r$ ; (e) $S_d^r R_u^l$ ; (f) filtered $S_d^r R_u^l$ .

After the wavefield decomposition, the separated four term images are shown in Figure 5.8. The single-directional terms (Figure 5.8a and 5.8b) show the image of nearly flat layers with few artefacts. The $S_d^r R_u^l$ term (Figure 5.8c) shows the clear three faults with high resolution, and the $S_d^l R_u^r$ term (Figure 5.8e) presents the tilted layers in the fault area. The artefacts in the Figure 5.8(c) and 5.8(e) are easy to be identified as they are located in the flat layer zone corresponding to the single-directional terms, and the directional filter can be applied to eliminate these artefacts, which are shown in Figures 5.8(d) and 5.8(f).

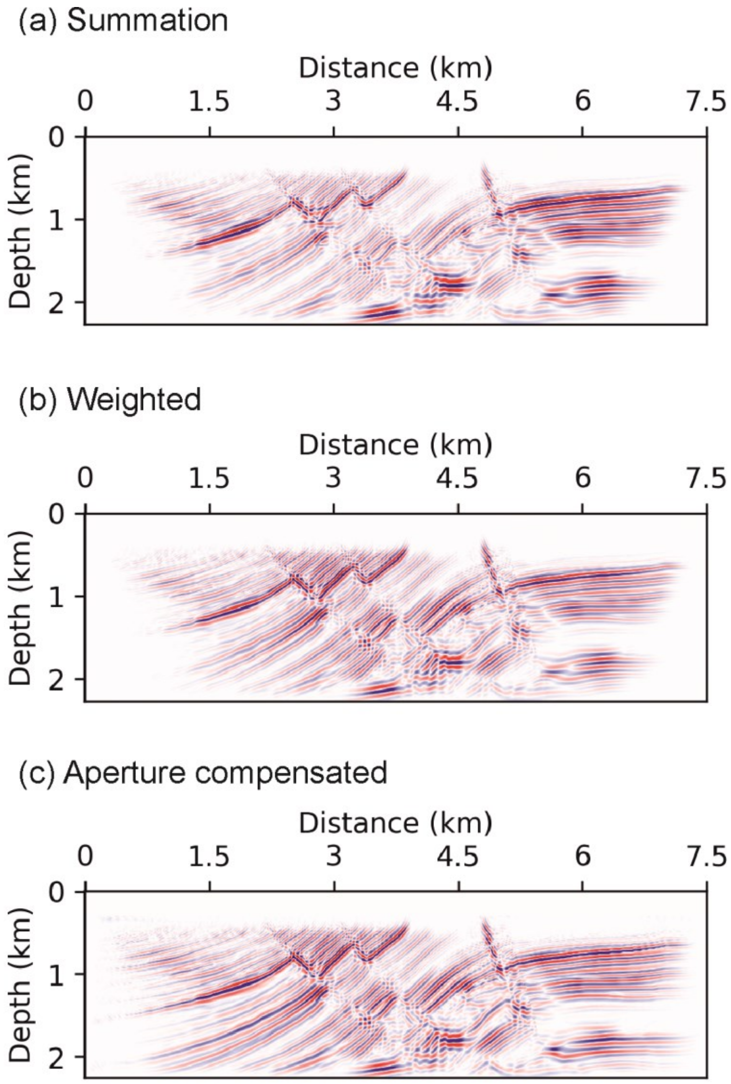


**Figure 5.9** The RTM images of the fault area of the Marmousi model. (a) The summation of the four filtered terms in Figure 5.8; (b) the weighted summation of Eq. (5.7); (c) after aperture compensation by the gradient of conventional RTM images (Figure 5.7b).

Figure 5.9 shows the recombination and further processing of the migration images based on the filtered four terms. Figure 5.9(a) shows the direct summation of the four terms, where the artefacts are greatly reduced, and the thin layers are much clearer than the conventional RTM results. Theoretically, the simple summation of these four terms is identical to the simple up/down going wave decomposition result. However, the simple up/down decomposition result lacks flexibility, as it is incapable of filtering each term and further reducing the artefacts.

Figure 5.9(b) shows the weighted images (Eq. 5.7), where the four weights are obtained numerically by inversion, which is to match the structural similarity index with the conventional RTM results:

$$\left(W_1,\ W_2,\ W_3,\ W_4\right)=\left(0.160,\ 0.293,\ 0.387,\ 0.160\right).$$

In the weighted image, the thin layers and faults are further illuminated. Figure 5.9(c) shows the aperture-compensated image, which is obtained from Figure 5.9(b) compensated by the gradient of the conventional RTM image to solve the limited aperture problem. This limited aperture problem is due to the weakened amplitude of the vertically propagated waves in wavefield decomposition. This aperture-compensated image exhibits high resolution and less artefacts than the conventional RTM results, and the thin layers and faults are clearly illuminated. This example demonstrates that this decomposition method is suitable for improving the resolution of the fault and thin layers and removing the artefacts.

## 5.5 Synthetic attenuating RTM in Sigsbee model

This section aims to test the performance of the biaxial wavefield decomposition method in attenuative media. The synthetic data is generated by the seismic simulation in attenuative media using the wave equation with fractional spatial derivatives (Eq. 5.8).

The Sigsbee model was created according to the geology of the Gulf of Mexico. It contains a series of sedimentary layers and an attenuating salt body. This example is difficult due to the complexed salt body and several normal and thrust faults contained in the model. This model is chosen for testing the effectiveness (of the proposed method) of attenuation compensation in fine layers and structures imaging. The true velocity and quality factor *Q* models are displayed in Figure 5.10. The salt body is a highly attenuative medium compared with its surrounding rocks. There are 135 shots, and 1320 receivers located at the depth of 300m. There are small structures (dots) in the depth of 3 km and 4.5 km in the true velocity model, which are unidentifiable in the migration model. The migration model is smoothed from the true velocity model.

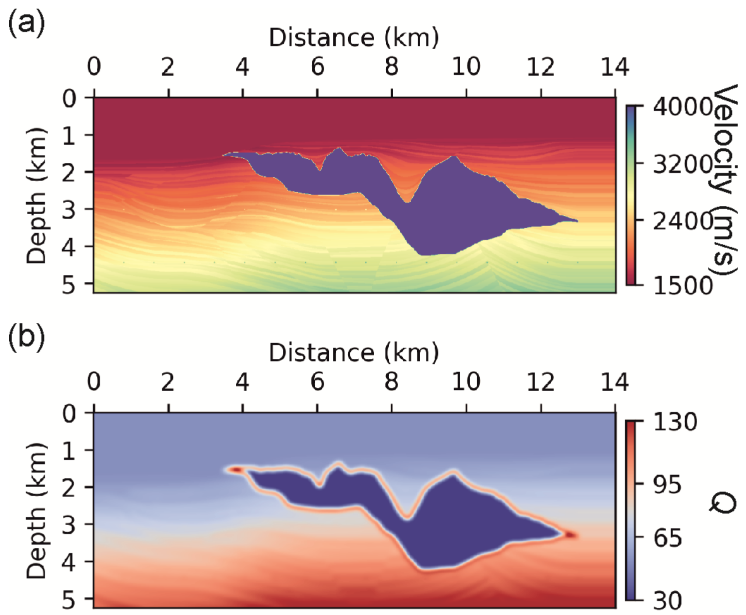


**Figure 5.10** The Sigsbee models. (a) The P-wave velocity model; (b) $Q$ model.

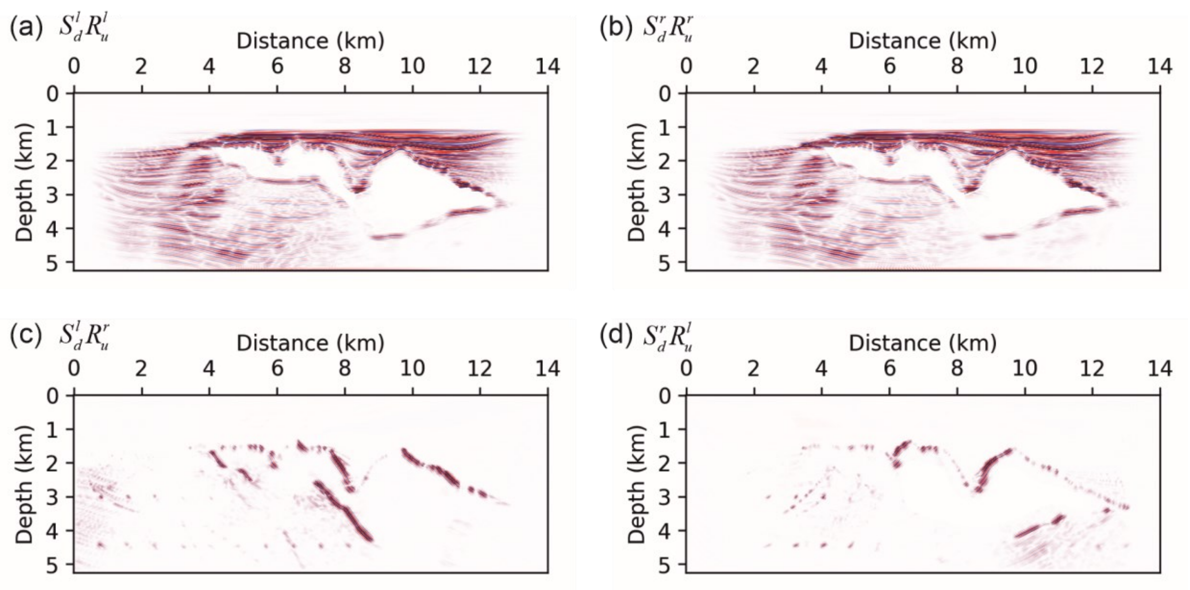


**Figure 5.11** The filtered four decomposed terms in the Sigsbee model. (a) $S_d^l R_u^l$; (b) $S_d^r R_u^r$. (c) $S_d^l R_u^r$; (d) $S_d^r R_u^l$.

Figure 5.11 presents the filtered four terms after attenuation compensation and wavefield decomposition. These four terms do not contain any strong artefacts in the shallow zone, and the layers and structures are highly illuminated in all terms. The single-directional terms (Figure 5.11a and 5.11b) show the image of nearly flat layers with little artefacts. The $S_d^l R_u^r$ term (Figure 5.11c) and $S_d^r R_u^l$ (Figure 5.11d) present the tilted boundaries of the salt body, the tilted interfaces, and the small structure in the depth of 3 km and 4.5 km.

Figure 5.12 shows the comparison of several RTM images. When directly using the conventional RTM to the attenuating data, only the top interfaces are shown but located at the wrong position (Figure 5.12a). There are strong artefacts in the shallow zone, the dense sedimentary layers are not identifiable, and the whole salt body cannot be appropriately imaged. Even after applying the Laplacian filter (Figure 5.12b), only the shallow part layers are presented, and the top boundary of the salt body is obviously distorted.

After attenuation compensation (Figure 5.12c), the whole salt body is clearly identifiable, and the boundaries are located in the correct position. However, it is impossible to ignore the formidable strong artefacts in the shallow part, and the layer interfaces are indistinct. This unfavourable artefacts issue can be eased by the Laplacian filter (Figure 5.12d), which illuminates the thin layers and the faults, and the small structures (the dots) can be identified.

Figure 5.12(e) shows the wavefield decomposition RTM images (Eq. 5.7), the four weights are obtained numerically as:

$$\left(W_1,\ W_2,\ W_3,\ W_4\right) = \left(0.142,\ 0.359,\ 0.357,\ 0.142\right).$$

This decomposed image eliminates the large artefacts and produces clear boundaries of the salt body. Surprisingly, underneath the salt body, the faults, interfaces, and small structures are also visible. After compensation for the limited aperture issue, the final migration images (Figure 5.12f) present distinct layers and structures. This example shows that the proposed wavefield decomposition method can successfully apply to attenuation compensation RTM.

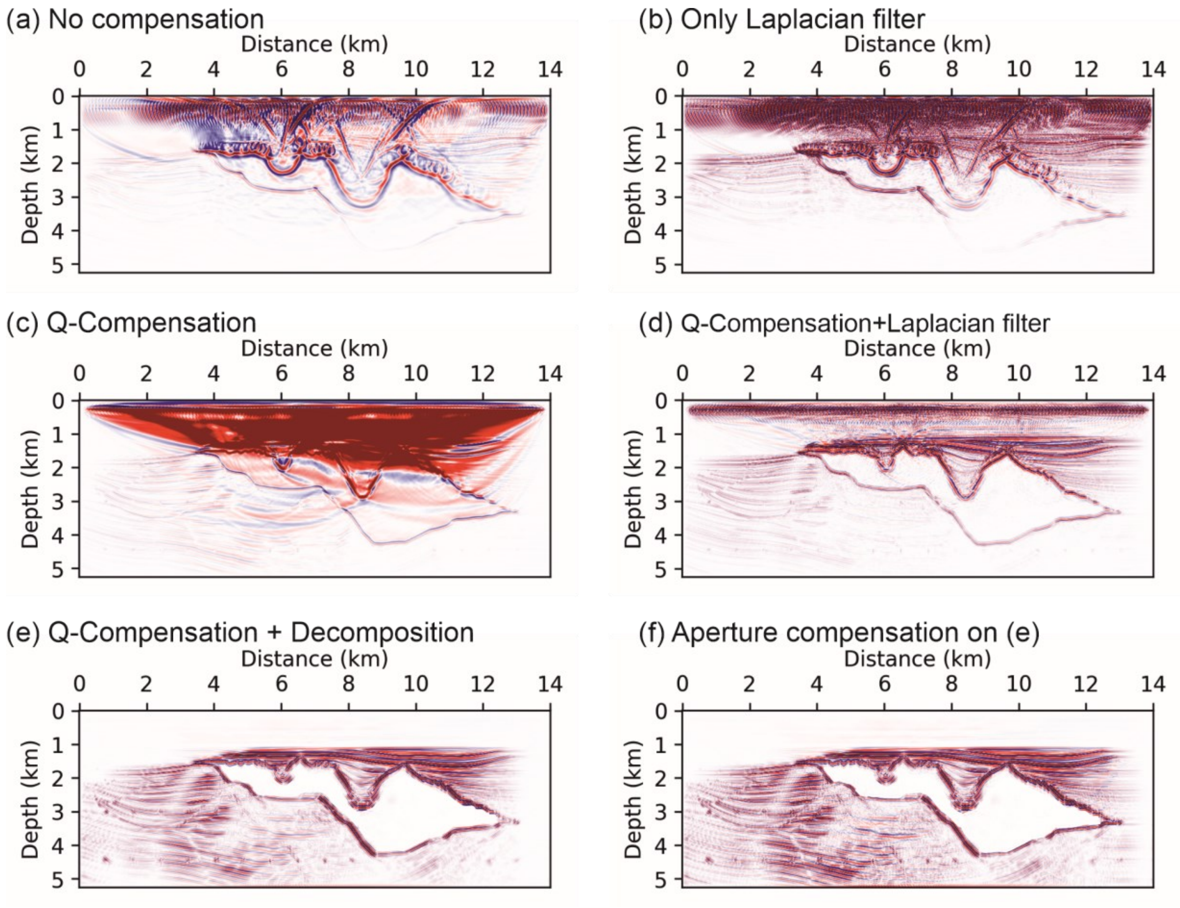


**Figure 5.12** The RTM images of Sigsbee model, the attenuated data is generated by viscoelastic wave Eq. (5.8). (a) Conventional RTM images; (b) applying the Laplacian filter to Figure (a); (c) $Q$ compensated RTM images; (d) applying the Laplacian filter to Figure (c); (e) RTM image with $Q$ compensated RTM images and wavefield decomposition; (f) aperture compensation for the boundary areas of Figure (e).

## 5.6 Conclusion

Migration artefacts greatly impact the quality of seismic images. In this chapter, the biaxial wavefield decomposition is introduced to decomposed wavefields in both lateral and vertical directions to reduce the artefact caused by the cross-correlation of unphysical waves. After eliminating the up-going source wavefield and down-going receiver wavefield, the remaining four terms have different contributions to the migration results: the single-directional terms are capable of imaging the flat layer, while the cross-directional terms can well present the tilted interfaces and faults. Another advantage is that the artefacts can be identified much easier and reduced as the four terms are decoupled. The weight can also be adjusted to illuminate the thin and delicate subsurface structures, as the tilted layers and faults are separated. The decomposition method can be implemented efficiently by the Hilbert transform method, which builds the analytical wavefield and eliminates the negative frequency components. Additionally, this wavefield decomposition method can be applied to attenuation compensation RTM by exploiting the viscoelastic wave equation with fractional spatial derivatives. The synthetic examples demonstrate that the artefacts are effectively reduced after wavefield decomposition, and the resultant four decomposed images and final RTM images better present the complex subsurface structure, and the resolution is greatly improved compared with conventional RTM results.

# Chapter 6

# Practical application

In the previous chapters, the biaxial wavefield decomposition method is introduced and implemented to attenuation compensation reverse-time migration. The synthetic examples present effective artefact elimination after performing the wavefield decomposition. This chapter presents a field data migration example. First, the migration settings and data processing methods are introduced, and the migration results are compared. Further, the potential problems are discussed.

## 6.1 Survey configuration

The field data is a 2D line extracted from a 3D survey dataset in the area of a solid salt body. This dataset includes 93 shots with the interval of 150m. Each shot is followed by a streamer with 324 hydrophones, with a trace interval of 25 m. The depth of the source and hydrophones are 10 m and 12 m. The total record length is cut to 6 seconds to save computational time. The true velocity model is displayed in Figure 6.1(a), and the migration velocity model is obtained by smoothing the true model. The $Q$ model is generated from the empirical formula (Figure 6.1b):

$$Q = 11.49\left(\frac{c_0}{1000}\right)^{1.879} - 10.57\,, \tag{6.1}$$

where $c_0$ is the pure acoustic velocity. The water is assumed to be purely acoustic, and the $Q$ value is given as 1000. The density model is calculated by Gardner's equation as $\rho = 0.31c_0^{0.25}$ (Gardner *et al.* 1974), except for the density of the water layer setting as 1000 kg/m$^3$.

It should be noted that the quality factor model (Figure 6.1b) may not be accurate, as the empirical formula Eq. (6.1) is based on Tarim basin China. However, several projects have proven that this model is applicable to field data. Also, as the salt body is solid and weakly attenuative, the quality factor is relatively large, so the seismic data is less sensitive to the small perturbation of the quality factor, making the compensation of the attenuation relatively reasonable.

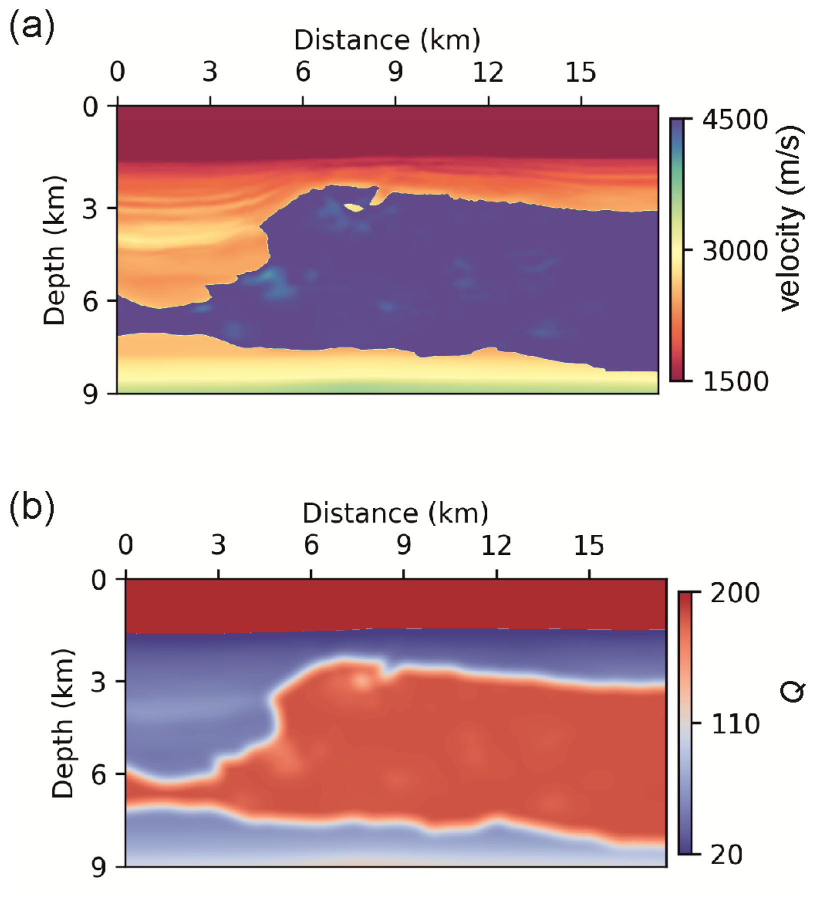


**Figure 6.1** The models used in field data example. (a) The P-wave velocity model; (b) $Q$ model.

## 6.2 Data processing

The chosen dataset is a pre-processed dataset. Although this data set has already been denoised, de-bubbled, and de-multiples, and the direct wave has been cut, considering the large time interval and 3D survey, the following process is performed.

### 1. Data interpolation

First, the original data is interpolated from 8 ms to 1 ms in time interval. The original data is resampled by sinc interpolation to avoid numerical instability. The sinc interpolation is equivalent to applying the low-pass filter in the frequency domain. The following is an example of the interpolated trace section. The original time interval of the field data is 8 ms, and the interpolated time interval is 1 ms. Figure 6.2 shows a segment of the data series before and after sinc interpolation, which demonstrates that the interpolated data have great continuity and match well with the original data.

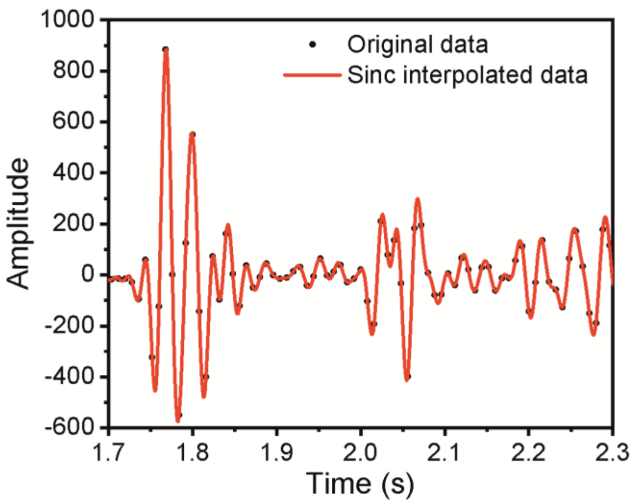


**Figure 6.2** A segment of the original recorded data with time interval of 8 ms and the sinc interpolated data with time interval of 1 ms.

**2. Data compensation from 3D to 2D**

Second, the 3D data is transferred to 2D. The original 3D survey dataset cannot be directly applicable to the 2D migration algorithm, because not only the amplitude is inconsistent due to geometric spreading, but also the phase shift. Therefore, partial compensation should be adopted to transfer the 3D data to 2D before migration. This data compensation from 3D to 2D can be implemented based on the Green's function of the wave equation (Y. Wang & Rao 2009). Considering the viscoelastic wave equation with fractional time derivative in the frequency domain:

$$\nabla^2\left(1+\beta\left(\frac{i\omega}{\omega_0}\right)^{\beta}\right)\tilde{u}(\omega,\mathbf{x})+\frac{\omega^2}{c^2}\frac{\partial^2}{\partial t^2}u=\frac{1}{\sqrt{2\pi}}\delta(\mathbf{x}-\mathbf{x}_0)\,, \tag{6.2}$$

Eq. (6.2) may be rewritten as a Helmholtz equation as

$$\nabla^2\tilde{u}(\omega,\mathbf{x})+\frac{\omega^2}{c^2}\left(1+\beta\left(\frac{i\omega}{\omega_0}\right)^{\beta}\right)^{-1}\tilde{u}(\omega,\mathbf{x})=\frac{1}{\sqrt{2\pi}}\left(1+\beta\left(\frac{i\omega}{\omega_0}\right)^{\beta}\right)^{-1}\delta(\mathbf{x}-\mathbf{x}_0)\,. \tag{6.3}$$

The Green's function of the 2D and 3D cases is

$$G_{2D}(\omega,\mathbf{x})=-\frac{\mathrm{i}}{4}H_0^{(2)}\left(\frac{\omega}{c}\left(1+\beta\left(\frac{\mathrm{i}\omega}{\omega_0}\right)^{\beta}\right)^{-1/2}|\mathbf{x}-\mathbf{x}_0|\right)\frac{1}{\sqrt{2\pi}}\left(1+\beta\left(\frac{\mathrm{i}\omega}{\omega_0}\right)^{\beta}\right)^{-1}, \tag{6.4}$$

$$G_{3D}(\omega,\mathbf{x})=-\frac{e^{-\mathrm{i}\frac{\omega}{c}\left(1+\beta\left(\frac{\mathrm{i}\omega}{\omega_0}\right)^{\beta}\right)^{-1/2}|\mathbf{x}-\mathbf{x}_0|}}{4\pi|\mathbf{x}-\mathbf{x}_0|}\frac{1}{\sqrt{2\pi}}\left(1+\beta\left(\frac{\mathrm{i}\omega}{\omega_0}\right)^{\beta}\right)^{-1}, \tag{6.5}$$

where $H_0^{(2)}(\bullet)$ denote the zero-order Hankel function of second kind. The compensation operator can be formulated as

$$
\begin{aligned}
W &= \frac{G_{2D}(\omega,\mathbf{x})}{G_{3D}(\omega,\mathbf{x})} \\
&\approx \mathrm{i}\pi\left|\mathbf{x}-\mathbf{x}_0\right| e^{\mathrm{i}z}\sqrt{\frac{2}{\pi z}}e^{-\mathrm{i}\left(z-\frac{\pi}{4}\right)} \\
&= \mathrm{i}\left|\mathbf{x}-\mathbf{x}_0\right|\sqrt{\frac{2\pi}{z}}e^{\mathrm{i}\frac{\pi}{4}} \\
&= \sqrt{2\pi}\left|\mathbf{x}-\mathbf{x}_0\right| z^{-1/2} e^{\mathrm{i}\frac{3\pi}{4}},
\end{aligned}
\tag{6.6}
$$

where

$$
z = \frac{\omega}{c}\left(1+\beta\left(\frac{\mathrm{i}\omega}{\omega_0}\right)^{\beta}\right)^{-1/2}\left|\mathbf{x}-\mathbf{x}_0\right|. \tag{6.7}
$$

In the derivation above, the asymptotic form for the Hankel function is applied:

$$
H_{\alpha}^{(2)}(z) \approx \sqrt{\frac{2}{\pi z}}e^{-\mathrm{i}\left(z-\frac{\alpha\pi}{2}-\frac{\pi}{4}\right)}, \tag{6.8}
$$

It can be assumed that the travel distance is proportion to the travel time: $\left|\mathbf{x}-\mathbf{x}_0\right| = Av(\omega)t$, where $v(\omega)$ is the phase velocity, and $A$ is a scaling factor. Therefore, the compensation operator (Eq. 6.6) may be rewritten as:

$$
W = \frac{G_{2D}(\omega,\mathbf{x})}{G_{3D}(\omega,\mathbf{x})} = \sqrt{\frac{2\pi A v(t,\omega) c(\beta) t}{\omega}}\left(1+\beta\left(\frac{\mathrm{i}\omega}{\omega_0}\right)^{\beta}\right)^{1/4} e^{\mathrm{i}\frac{3\pi}{4}}. \tag{6.9}
$$

When $\beta = 0$, the above compensation operator is the purely elastic transform compensator, which is consistent with Y. Wang & Rao (2009)

$$
W = \frac{G_{2D}(\omega,\mathbf{x})}{G_{3D}(\omega,\mathbf{x})} = \sqrt{\frac{2\pi A t}{\omega}c}\,e^{\mathrm{i}\frac{3\pi}{4}}. \tag{6.10}
$$

In the seismic profile, the viscoelastic velocity is time/depth dependent, therefore, this compensator is dependent on both time $t$ and frequency $f$. Therefore, the time-frequency spectrum of the data series is required to do the partial compensation. The Gabor transform can be used to obtain the time-frequency spectrum (Y. Wang 2008b; 2022). Figure 6.3 shows the time-frequency spectrum of a selected data series in Figure 6.4(a). During the compensation,

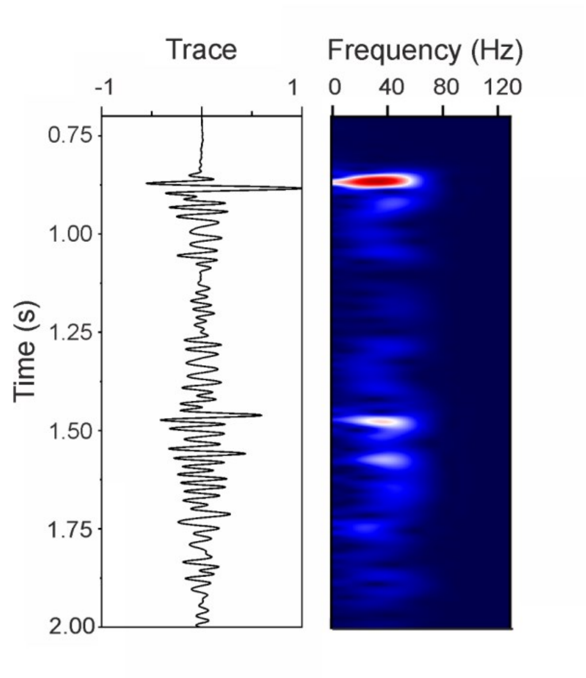


**Figure 6.3** A segment of recorded data and its time-frequency spectrum by Gabor transform.

the RMS value of the viscoelastic velocity and viscoelastic parameter is used. Figure 6.4 shows the comparison between the original 3D trace and compensated 2D trace. There are both amplitude changes and phase shifts in the two traces.

## 6.3 Wavelet estimation

Wavelet estimation is significant for reverse-time migration. An unsuitable seismic wavelet may cause severe noise and distortion in migration images. For the marine seismic survey, the water can be viewed as purely acoustic material. And the wavelet can be obtained from the direct wave. The direct wave is initially cut from the recorded data of the smallest offset receiver, for the preparation of the wavelet extraction.

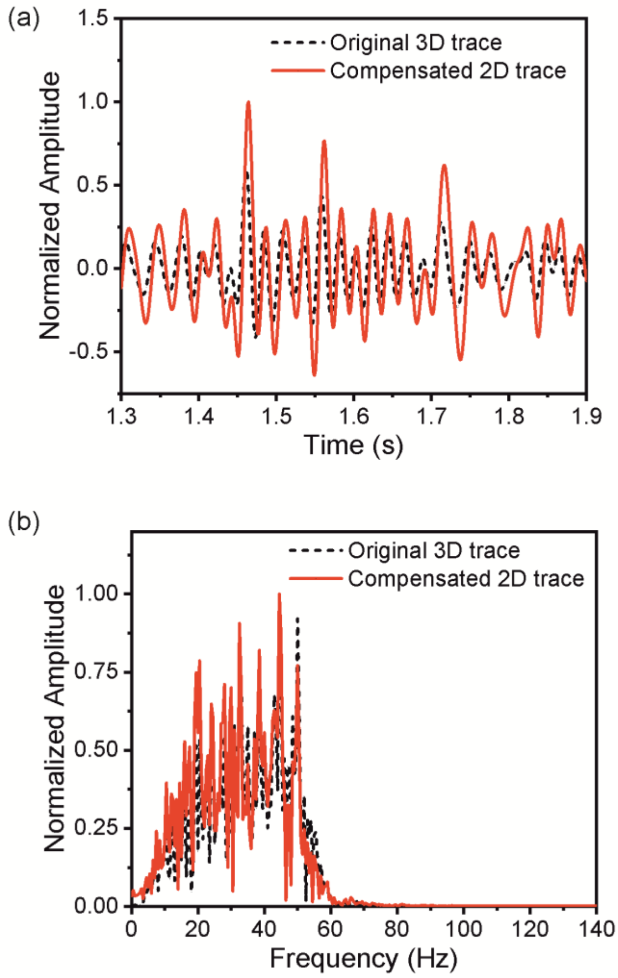


**Figure 6.4** The effect of the partial compensation. (a) A trace section; (b) the amplitude spectrum.

A mature method for wavelet estimation is the Weiner filtering method (Gray *et al.* 2019). Weiner filtering method is to build a filter function between the predicted data and the real data, which is corresponding with the relationship between the predicted wavelet and the true wavelet. A filter $\mathbf{f}$ is defined that satisfies the following approximation

$$\mathbf{d}_{\text{pred}} * \mathbf{f} \approx \mathbf{d}_{\text{real}}, \tag{6.11}$$

where $\mathbf{d}_{\text{pred}}$ is the predicted data from propagating a known source wavelet $\mathbf{w}_0$, $\mathbf{d}_{\text{real}}$ is the real seismic data, and the operator "$*$" denotes for convolution. In this example, the direct wave is considered. An initial known wavelet $\mathbf{w}_0$, is used to generate predicted data, and it is a 20-Hz Ricker wavelet. This source wavelet is then propagated through the water layer to generate a direct wave to the receiver. The filter $\mathbf{f}$ is then calculated by solving the equation:

$$\mathbf{f} \approx \mathbf{d}_{\text{pred}}^{-1} * \mathbf{d}_{\text{real}} . \tag{6.12}$$

The estimated wavelet can be obtained from the filter and the predicted wavelet as:

$$\mathbf{w}_{\text{est}} = \mathbf{f} * \mathbf{w}_0 , \tag{6.13}$$

where $\mathbf{w}_{\text{est}}$ is the estimated wavelet. The estimated wavelet $\mathbf{w}_{\text{est}}$ is shown in Figure 6.5.

The direct Weiner-filtered wavelet (Figure 6.5) has a long-time duration, which is not favourable for reverse-time migration, as a long-lasting wavelet will cause severe artefacts, further greatly lowering the resolution of the final images. The reason for this unfavourable wavelet is that the direct wave contains large noise, which cannot be fully eliminated.

To reform the wavelet, the frequency spectrum of traces is considered, which is plotted as the black solid line in Figure 6.6(b). The amplitude spectrum contains notches, which are generally caused by anomalies (Y. Wang 2008a). Therefore, a shaping filter is applied to modify the amplitude as a smoothed curve (the red solid line in Figure 6.6b), with the total energy remaining unchanged. The phase information is identical to the previous wavelet. The final filtered wavelet is shown in Figure 6.6(a). The reshaped wavelet is relatively smooth and short, thus suitable for seismic migration.

The direct Wiener-filter wavelet (Figure 6.5) is based on the direct wave, and due to the noise and multiples, this wavelet presents several peaks and an unsmooth spectrum. This will greatly harm the final migration result. On the contrary, the final wavelet (Figure 6.6a) has less time duration and a smooth spectrum, which will generate higher-resolution images. Additionally, the final wavelet has an explicit peak and trough, making it easier to identify of the layers and boundaries. The final wavelet is also consistent with the result obtained from the first arrival.

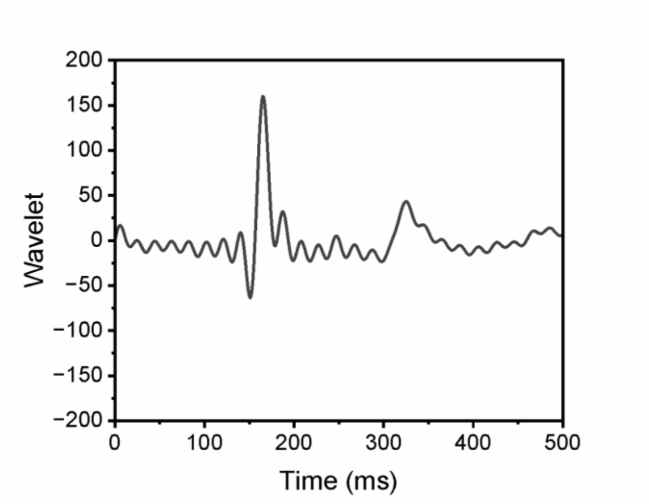


**Figure 6.5** The wavelet estimated directly form the Wiener filter.

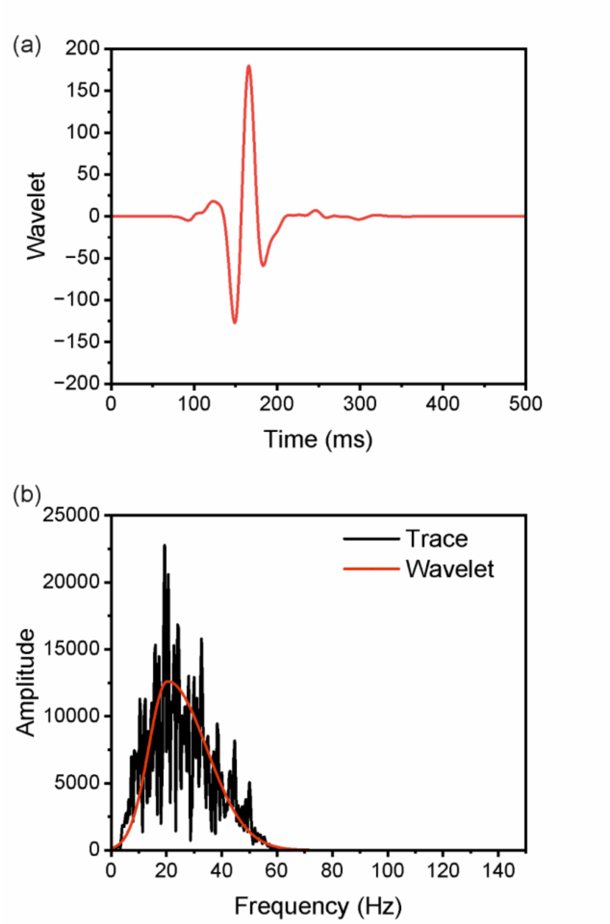


**Figure 6.6** Reshaping the wavelet. (a) The reshaped wavelet using for migration; (b) Amplitude spectrum comparison between the selected trace and reshaped wavelet. The energies of these two spectra are identical.

## 6.4 Migration results

This section presents the migration results using the field data and source wavelet obtained above. The conventional RTM is first performed and then the attenuation compensation and wavefield decomposition are implemented.

The conventional RTM result is shown in Figure 6.7(a). Although the top boundary of the salt body can be roughly identified, the extremely strong artefacts in the shallow part are non-ignorable. The image of the deep zone is extremely weak, which is not only due to the geometric spreading, but also the attenuation. To reduce the large-amplitude low-frequency artefacts, the Laplacian filter is applied (Figure 6.7b). However, only the water bottom and top boundary of the salt body are visible, and its lower boundary is too weak to be identified.

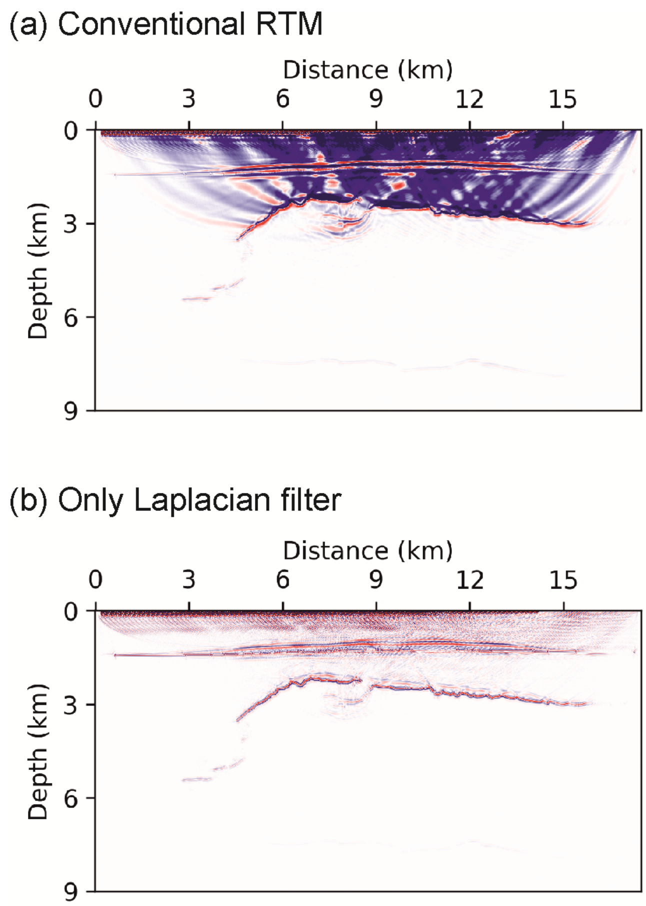


**Figure 6.7** The conventional RTM results of field data. (a) Conventional RTM results; (b) after applying the Laplacian filter to (a).

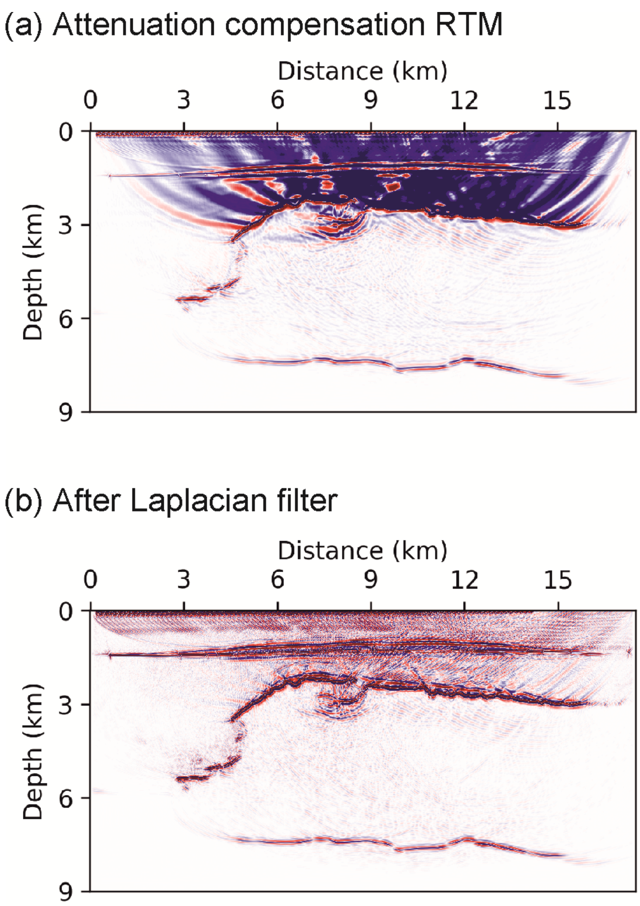


**Figure 6.8** The attenuation compensation RTM results. (a) Attenuation compensation RTM; (b) after applying the Laplacian filter to (a).

After attenuation compensation, as shown in Figure 6.8(a), the amplitude in the deep part is greatly amplified and the lower boundary of the salt body is identifiable. Not surprisingly, there are still a large number of artefacts in the shallow part. After the Laplacian filtering (Figure 6.8b), the low-wavenumber artefacts are partly reduced, and become scattered and dense dotted noise on the top of the salt body, hindering the presentation of the structures.

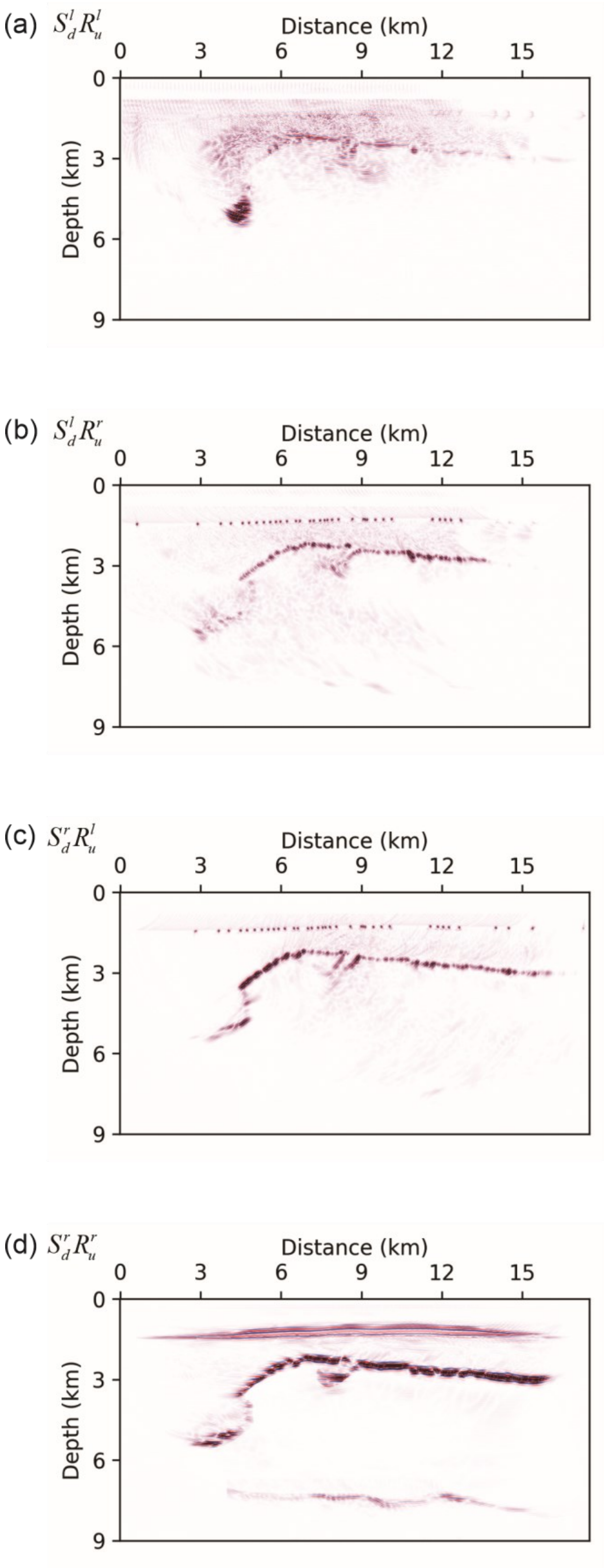


**Figure 6.9** The four decomposed terms in field data example. (a) $S_d^l R_u^l$; (b) $S_d^l R_u^r$; (c) $S_d^r R_u^l$; (d) $S_d^r R_u^r$.

Figure 6.9 shows the filtered four terms after attenuation compensation and wavefield decomposition. The $S_d^l R_u^l$ (Figure 6.9a) term is entire artefacts that need to be discarded, as the source is on the left-hand side of the receiver groups and thus this combination is unphysical. The image in the depth of 5 km, approximately, is probably due to the scattering waves. The $S_d^l R_u^r$ image (Figure 6.9b) presents the roughly top boundary of the salt body. However, the remaining artefacts cannot be effectively reduced. The $S_d^r R_u^l$ image (Figure 6.9c) contains similar information as the $S_d^l R_u^r$ image but presents a much clearer boundary and less artefacts. Significantly, the $S_d^r R_u^r$ image (Figure 6.9d) is the main contribution in this example, which demonstrate clear water bottom, top and lower boundaries.

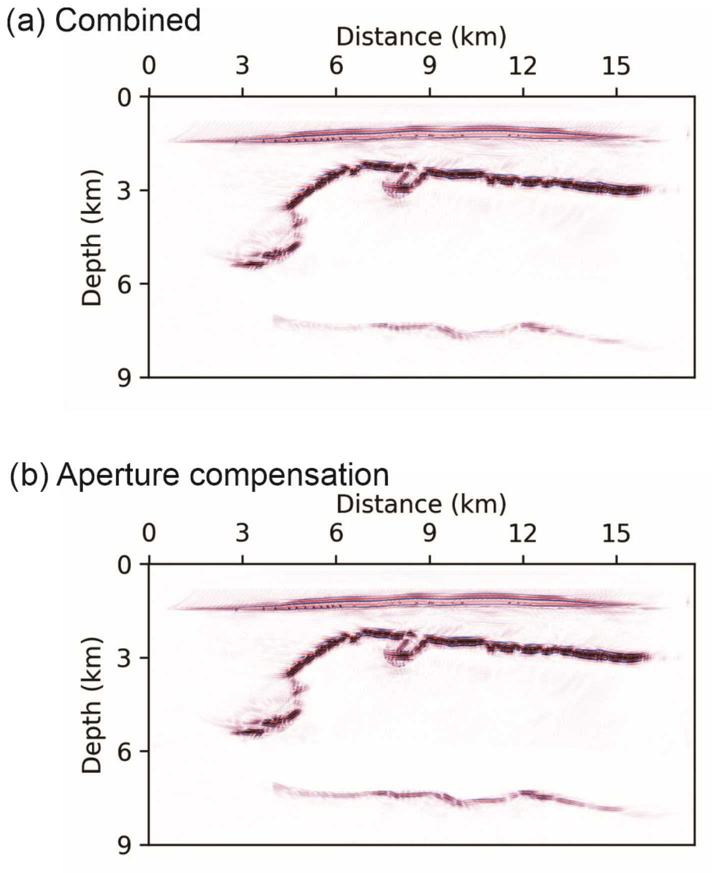


**Figure 6.10** The wavefield decomposition migration images. (a) The combination of the four wavefield decomposition terms.; (b) after aperture compensation.

Figure 6.10(a) shows the wavefield decomposition RTM images, the four weights are assigned as $\left(W_1,\ W_2,\ W_3,\ W_4\right)=\left(0,\ 0,\ 0.750,\ 0.250\right)$, as $S_d^l R_u^l$ is the artefacts and also $S_d^l R_u^r$ and $S_d^r R_u^l$ shows similar boundaries but $S_d^r R_u^l$ outperforms. The remaining two coefficients are obtained by numerically matching with attenuation compensation RTM result. This decomposed image eliminates the large artefacts in the shallow area and illuminates the salt boundaries. After compensation for the limited aperture issue, the final migration image (Figure6.11b) clearly shows the layers and structures. This example demonstrates that the proposed method is suitable for generating high-resolution RTM images for field data.

## 6.5 Discussion

The main objective of the biaxial wavefield decomposition is to reduce the artefacts in the migration image, which achieves satisfying results in this field data example. For eliminating the shallow strong artefacts, this method is very effective. Especially in this example, the Laplacian filter fails to remove the shallow artefacts, and brings new noise to the image. By decomposing the wavefield, and only considering the down-going source wavefield and the up-going receiver wavefield, the shallow artefacts can be reduced. The decomposition of left- and right-going waves allows for further identifying the artefacts. Filtering the four decomposed terms and adding weights provide flexibility for removing the artefacts and improving the resolution. In this sense, the biaxial wavefield decomposition method can improve the resolution of the migration image by removing the artefacts.

Although in this example, the attenuation compensation and the wavefield decomposition improve the resolution of the migration result, the layers between the salt body and the water bottom are almost invisible, as shown in the true velocity model (Figure 6.1a). If zooming in the layer zone of the $S_d^r R_u^r$ term (Figure 6.9d), which is the main contribution of the migration image, and increasing its amplitude, as shown in Figure 6.11, the migration result is still consistent with the true layers, however, severely hindered by the remaining artefacts. There are two reasons. First, the impedance contrast between the layers is small and the variation is very smooth, contrary to the sharp and rigid boundary of the salt body. This leads to weak reflected waves and subsequent weak images. Also, due to the large impedance contrast between the salt body and its surrounding rock, there are strong reflected waves between the salt body and the water bottom, leading to strong artefacts in that area. Therefore, the strong artefacts lead to difficulty in the clear presentation of these layers. Still, the decomposed images can distinguish these layers from the artefacts. On the contrary, these layers are entirely invisible in the attenuation compensation RTM result. Figure 6.11 also presents a general consistency between the image and the model, which can be observed at the interfaces between the salt body and the surrounding rocks. However, the image and the interface are not perfectly matching to each other. This is due to the inaccuracy of models and processed data.

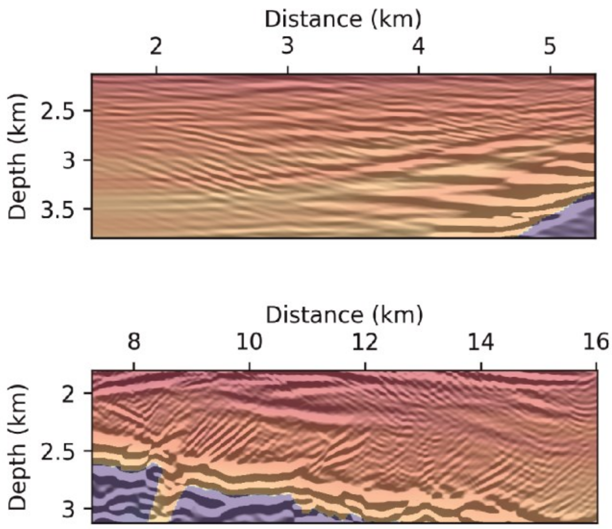


**Figure 6.11** Two layered zones of the migration result in the $S_d^r R_u^r$ term. The background colour is the true velocity model, and the front grey figure is the corresponding migration image in Figure 6.9(d).

Additionally, the aperture compensation in this field data example, as shown in Figure 6.10(b), does not improve the visible range of the image significantly, as it functions in the synthetic data examples. This is due to the relative shot-receiver location and the small number of shots and receivers. In the synthetic example, the shots cover the whole model, and the receivers are located on almost every grid of the specific depth. However, in this field data example, the shot is always on the left side of the receivers, and the coverage of the receivers is also limited, resulting in useful information being missing. This can be verified by Figure 6.9, as $S_d^l R_u^l$ and $S_d^l R_u^r$ images do not provide any useful structure information, thus being discarded.

Also, considering the setting of this example, the following aspects may lower the resolution of the migration image:

1. The field data applied in this example is the simplified version, which has been significantly truncated to save computational memory. The density of the hydrophone is reduced, which causes useful information to be lost.
2. The number of shots is insufficient, and the range of the shots is limited. This limited range of shots and receivers leads to poor illumination of some parts of the image, especially the left boundary side. To obtain better migration results, more shots and recorded data should be included.
3. The migration wavelet is estimated from the direct wave and reshaped according to the amplitude spectrum of the trace, and it may be inaccurate from the true source signature. An accurate source function for the seismic survey may greatly improve the quality of the migration result.

It should be noted that reverse-time migration significantly depends on the reliability of the velocity model. In this example, the migration velocity is obtained by smoothing the true velocity model, so the migration model is accurate. In practical engineering, the migration velocity model can be less accurate. The inaccuracy of the velocity model would cause severe deterioration of migration results.

# Chapter 7

# Conclusion and future work

The previous chapters examined the theories and methods of seismic simulation and subsequent reverse-time migration in attenuating media. This chapter summarises the main conclusions of previous work and provides an outlook for future work.

## 7.1 Conclusion

Viscoelasticity is an essential property of the subsurface media, which brings attenuation effects to the seismic data. Attenuated seismic data have distorted phase and weakened amplitude, which significantly lowers the resolution and fidelity of reverse-time migration images.

The main innovative contribution of this thesis is to develop the understanding of seismic wave propagation in viscoelastic media, investigate attenuation compensation, and reduce the artefacts in reverse-time migration. My contribution presented in this thesis includes:

1. Established the viscoelastic parameters in the generalised viscoelastic model, and implemented it in seismic simulation. The generalised viscoelastic wave equation unifies the pure elasticity and viscoelasticity into a compacted form and follows the basic power-law attenuation. The explicit form of the rate-of-relaxation function is derived first, and it is proven that this viscoelastic model is causal and stable, and as a

result, suitable for seismic simulation. Then, the two key parameters, viscoelastic parameter and viscoelastic velocity are formulated with the commonly used parameters, quality factor $Q$ and reference velocity. The seismic simulation results show that the proposed formulae can well represent the energy absorption and velocity dispersion effects in viscoelastic media.

2. Developed an effective and accurate implementation method for the generalised viscoelastic wave equation. This work aims to solve the numerically challenging fractional time derivatives in the generalised viscoelastic wave equation in seismic wave simulation. The fractional time derivative is transferred into fractional spatial derivatives, which can be solved by the pseudo-spectral implementation, and introduced a spatial filter to correct the simulation error caused by averaging during this implementation in heterogeneous media. After accurately simulating the seismic wave propagation, the proposed wave equation is subsequently applied to attenuation compensation reverse-time migration, to compensate for the weakened amplitude and distorted phase in the seismic migration image, thus improving the resolution of the migration images.
3. Developed the biaxial wavefield decomposition method in reverse-time migration. This work aims to reduce the artefacts in reverse-time migration, which are caused by the cross-correlation of unphysical waves. It is proposed to decompose the wavefield both horizontally and vertically, and separate it into four directional waves. The up-going wavefield and down-going receiver wavefields are initially discarded, and the remaining cross-correlation terms may separate the flat layers and tilted layers. Then, weight coefficients are introduced when combining the terms, which may illuminate the thin and delicate layers. In the implementation of this decomposition, the Hilbert transform method is proved to be compatible with the viscoelastic wave equation,

demonstrating that this method is suitable for attenuation compensation in reverse-time migration. The synthetic data and field data examples indicate that the combination of attenuation compensation and wavefield decomposition greatly improves the resolution of the seismic images.

## 7.2 Future work 1: fractional spatial derivatives in viscoelastic media

In previous chapters, all discussion is focused on scalar wavefields, which is suitable for marine seismic surveys. For land seismic surveys, the seismic wavefield (particle velocity or displacement) should be a vector, which contains horizontal and vertical components (for 2D case). It would be straightforward to expand the current scalar theory to the vector wavefield.

To determine the vector wavefield in viscoelastic media, considering its stress-strain relation for one-dimensional deformation of the media, the generalised viscoelastic stress-strain relation is in a form of a fractional time differential equation (Y. Wang 2016) as

$$\sigma(t) = E\left(\varepsilon(t) + \beta\tau^{\beta}\frac{\mathrm{d}^{\beta}\varepsilon(t)}{\mathrm{d}t^{\beta}}\right), \tag{7.1}$$

where $\sigma(t)$ is the stress, $E$ is Young's modulus, $\varepsilon(t)$ is the strain, $\tau$ is the retardation time, and $\beta$ is the viscoelastic parameter, which is a constant in homogeneous media. In the wavenumber-frequency domain, Eq. (7.1) becomes

$$\tilde{\sigma}(\omega) = E\left[1 + \beta\left(\mathrm{i}\omega\right)^{\beta}\omega_0^{-\beta}\right]\tilde{\varepsilon}(\omega)\,, \tag{7.2}$$

where $\omega$ is the angular frequency, $\omega_0 = 1/\tau$ is the reference frequency, and $\tilde{\sigma}(\omega)$, $\tilde{\varepsilon}(\omega)$ are the stress and strain in the frequency domain. Making the weak attenuation assumption $k \approx \omega / c_0$, where $k$ is the wavenumber and $c_0$ is the reference velocity, Eq. (7.2) may be rewritten as

$$\tilde{\sigma}(\omega) = E\left[1 + \cos\left(\frac{\pi\beta}{2}\right)\beta\omega_0^{-\beta}k^{\beta}c_0^{\beta} + \mathrm{i}\omega\sin\left(\frac{\pi\beta}{2}\right)\beta\omega_0^{-\beta}k^{\beta-1}c_0^{\beta-1}\right]\tilde{\varepsilon}(\omega)\,. \tag{7.3}$$

Applying an inverse Fourier transform, Eq. (7.3) becomes

$$\sigma(t) = E\left(1 + \left(-\nabla^2\right)^{\beta/2} C_1 + \left(-\nabla^2\right)^{(\beta-1)/2} C_2 \frac{\partial}{\partial t}\right)\varepsilon(t)\,, \tag{7.4}$$

with

$$\begin{aligned} C_1 &= \beta\left(\frac{c_0}{\omega_0}\right)^{\beta} \cos\left(\frac{\pi\beta}{2}\right), \\ C_2 &= \frac{\beta}{c_0}\left(\frac{c_0}{\omega_0}\right)^{\beta} \sin\left(\frac{\pi\beta}{2}\right). \end{aligned} \tag{7.5}$$

Eq. (7.4) defines the generalised viscoelastic stress-strain relation in terms of fractional spatial derivatives, instead of the fractional time derivative in Eq. (7.1), to avoid the numerical challenge for fractional time derivatives.

For the 2D isotropic media, the stress-stain relation (Eq. 7.4) may be written explicitly as

$$\begin{bmatrix} \sigma_{xx} \\ \sigma_{zz} \\ \sigma_{xz} \end{bmatrix} = \begin{bmatrix} (\lambda+2\mu)a_P & (\lambda+2\mu)a_P - 2\mu a_S & 0 \\ (\lambda+2\mu)a_P - 2\mu a_S & (\lambda+2\mu)a_P & 0 \\ 0 & 0 & 2\mu a_S \end{bmatrix} \begin{bmatrix} \varepsilon_{xx} \\ \varepsilon_{zz} \\ \varepsilon_{xz} \end{bmatrix}, \tag{7.6}$$

where $\sigma_{ij}$ and $\varepsilon_{ij}$ are the components of the stress and strain tensor, respectively, $\lambda$ , $\mu$ are Lamé parameters, the subscript for *P* and *S* denotes P- and S- wave ,respectively, and the two operators are

$$\begin{aligned} a_P &= 1 + (-\nabla^2)^{\beta_P/2} C_{1P} + (-\nabla^2)^{(\beta_P-1)/2} C_{2P} \frac{\partial}{\partial t}, \\ a_S &= 1 + (-\nabla^2)^{\beta_S/2} C_{1S} + (-\nabla^2)^{(\beta_S-1)/2} C_{2S} \frac{\partial}{\partial t}. \end{aligned} \tag{7.7}$$

Combing the stress-strain relation Eq. (7.6) with the velocity-strain relation and momentum conservation equation, the generalised viscoelastic wave equation with fractional spatial derivatives for vector wavefields can be obtained.

According to Chapter 4, the fractional spatial derivatives operator in Eq. (7.7) cannot be directly applied to heterogeneous media, where the viscoelastic parameters $\beta_P$ and $\beta_S$ are spatially varied. In order to maintain the high efficiency of the averaging method, the correction function $f(\beta(\mathbf{x}))$, as derived in Eq. (4.19) can also be introduced to the operator as:

$$a_P = 1 + (-\nabla^2)^{\bar{\beta}_P(\mathbf{x})/2} f(\beta_P(\mathbf{x}))C_{1P} + (-\nabla^2)^{[\bar{\beta}_P(\mathbf{x})-1]/2} f(\beta_P(\mathbf{x}))C_{2P}\frac{\partial}{\partial t},$$
$$a_S = 1 + (-\nabla^2)^{\bar{\beta}_S(\mathbf{x})/2} f(\beta_S(\mathbf{x}))C_{1S} + (-\nabla^2)^{[\bar{\beta}_S(\mathbf{x})-1]/2} f(\beta_S(\mathbf{x}))C_{2S}\frac{\partial}{\partial t}, \tag{7.8}$$

where the correction function is formulated as

$$f(\beta_I(\mathbf{x})) \approx \left(\frac{\omega_m}{c}\right)^{\beta_I(\mathbf{x})-\bar{\beta}_I}\left(1+\frac{\beta_I(\mathbf{x})}{8}\cos\left(\frac{\pi\beta_I(\mathbf{x})}{2}\right)\right)^{\beta_I(\mathbf{x})-\bar{\beta}_I}. \tag{7.9}$$

where $\omega_m$ is the central frequency of the seismic band and the subscript "$I$" represent $P$ or $S$ waves.

To validate the proposed wave equation, here the comparison of the numerical solution of Eq. (7.6) and the analytical solution of the original elastic wave equation with fractional time derivative is conducted. The analytical solution of the fractional time derivative wave equation can be obtained by the Green's function method (Carcione 2014) as

$$u_1(r,\omega) = \left(\frac{F_0}{2\pi\rho}\right)\frac{xz}{r^2}[G_1(r,\omega)+G_3(r,\omega)], \tag{7.10}$$

$$u_3(r,\omega) = \left(\frac{F_0}{2\pi\rho}\right)\frac{1}{r^2}[z^2G_1(r,\omega)-x^2G_3(r,\omega)], \tag{7.11}$$

where $u$ is the displacement solution, $F_0$ is a constant controlling the magnitude of the force which acts in the positive $z$ direction, $r=\sqrt{x^2+z^2}$ ,

$$G_1(r,\omega) = -\frac{i\pi}{2}\left[\frac{1}{\tilde{c}_P^2}H_0^{(2)}\left(\frac{\omega r}{\tilde{c}_P}\right)+\frac{1}{\omega r\tilde{c}_S}H_1^{(2)}\left(\frac{\omega r}{\tilde{c}_S}\right)-\frac{1}{\omega r\tilde{c}_P}H_1^{(2)}\left(\frac{\omega r}{\tilde{c}_P}\right)\right], \tag{7.12}$$

$$G_3(r,\omega) = \frac{i\pi}{2}\left[\frac{1}{\tilde{c}_S^2}H_0^{(2)}\left(\frac{\omega r}{\tilde{c}_S}\right)-\frac{1}{\omega r\tilde{c}_S}H_1^{(2)}\left(\frac{\omega r}{\tilde{c}_S}\right)+\frac{1}{\omega r\tilde{c}_P}H_1^{(2)}\left(\frac{\omega r}{\tilde{c}_P}\right)\right], \tag{7.13}$$

where $\tilde{c}_P$ and $\tilde{c}_S$ are the complex velocities for P wave and S wave, respectively.

A seismic simulation is performed with the P- and S-wave quality factors $Q_P = 50$ and $Q_S = 30$, with the respective velocities 2500 and 1500 m/s, and the reference frequency is 500 Hz. The model is discretized into 400 × 400 grids with the spatial interval of 5 m and the time step of 0.5 ms. A 20-Hz Ricker wavelet source is emitted at the origin and a receiver is placed at (600 m, 600 m). From Figure 7.1, the numerical solutions of wave equation Eq. (7.6) perfectly match the analytical solution, which demonstrates the accuracy of the proposed wave equation.

Then, to intuitively present the viscoelastic effects, the proposed viscoelastic wave equation is applied to the Marmousi model. The P-wave velocity and $Q_P$ are shown in Figure 7.2. The S-wave velocity and $Q_S$ are obtained by $c_{0S} = c_{0P}/1.73$ and $Q_s = Q_P/1.2$. The model is discretized into 1501 ×601 grid points with 5 m spacing. A 15-Hz Ricker wavelet is emitted at (5000 m, 250 m). The time step is 0.5 ms.

Figures 7.3 shows snapshots of elastic and viscoelastic wavefields at 1.0s. It demonstrates that the viscoelastic wavefields have clearly delayed wavefront and reduced amplitude compared with their elastic counterparts. This example shows that the proposed viscoelastic wave equation for vector wavefields is applicable to complex geological models.

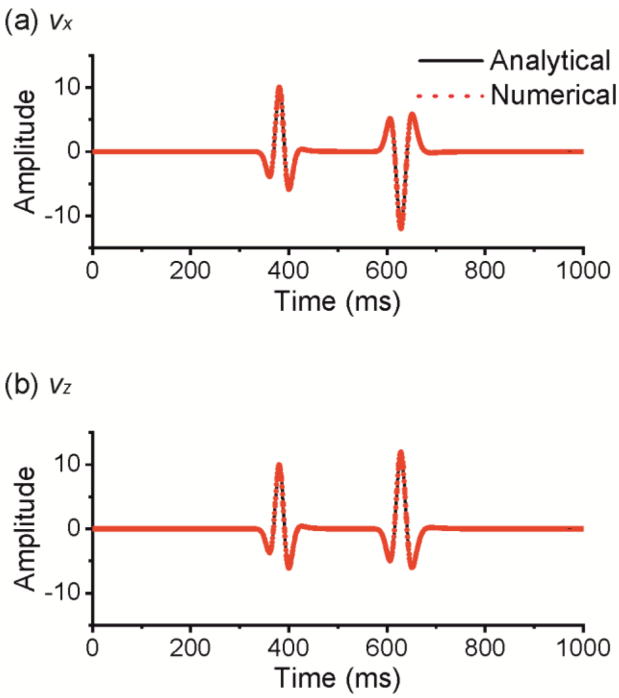


**Figure 7.1** Comparison of numerical results with analytical solutions in attenuating media. (a) Horizontal component of particle velocity. (b) Vertical component of particle velocity.

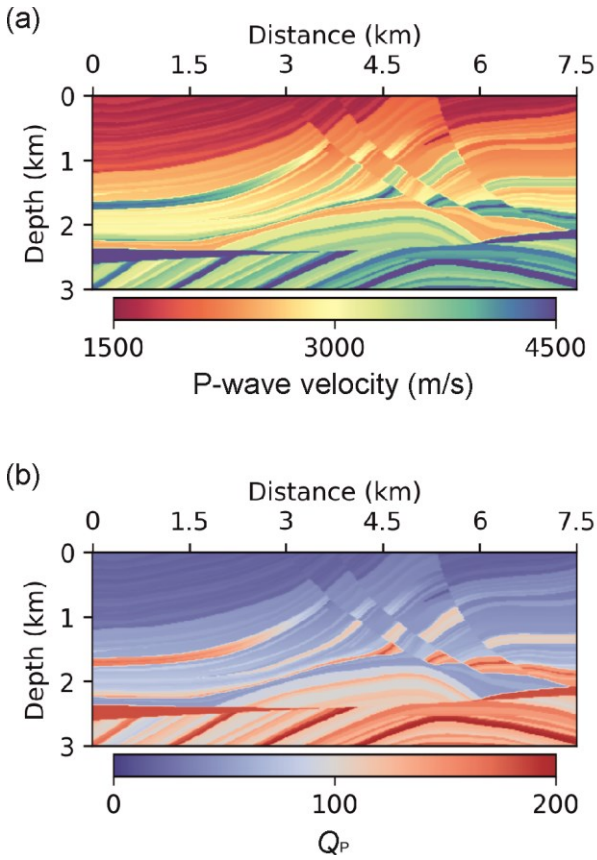


**Figure 7.2** P-wave velocity and $Q_P$ of Marmousi model.

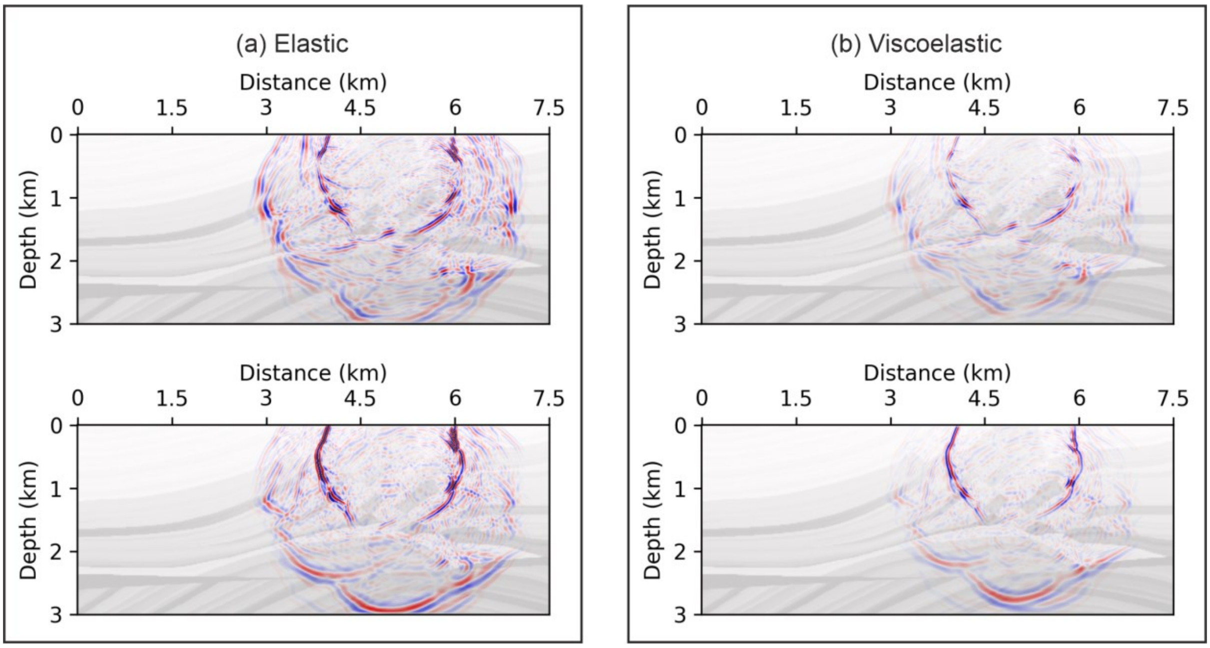


**Figure 7.3** Snapshots of the particle velocity wavefields at 1.0 s. (a) The elastic wavefield; (b) the viscoelastic wavefield. The first row is the horizontal component, and the second row is the vertical component.

## 7.3 Future work 2: fractional spatial derivatives in anisotropy attenuating media

In the previous chapters, only the isotropic media is considered. However, in practical application, anisotropy is also a very important property of earth media. Seismic anisotropy is the variation of the wave velocity with propagation direction. The analysis of anisotropy has drawn more and more attention as it is regarded as one of the indicators of potential karst, sedimentation, and fracture distribution. Ignoring the anisotropy of the media will also cause distorted and low-resolution migration images. Therefore, the viscoelastic theory proposed in this thesis may be further developed in anisotropic media, as follows.

First, let's consider the stress-strain relation in purely elastic anisotropic media, which can be written in a matrix form as:

$$\begin{pmatrix} \sigma_{11} \\ \sigma_{22} \\ \sigma_{33} \\ \sigma_{23} \\ \sigma_{13} \\ \sigma_{12} \end{pmatrix} = \begin{pmatrix} C_{11} & C_{12} & C_{13} & C_{14} & C_{15} & C_{16} \\ C_{12} & C_{22} & C_{23} & C_{24} & C_{25} & C_{26} \\ C_{13} & C_{23} & C_{33} & C_{34} & C_{35} & C_{36} \\ C_{14} & C_{24} & C_{34} & C_{44} & C_{45} & C_{46} \\ C_{15} & C_{25} & C_{35} & C_{45} & C_{55} & C_{55} \\ C_{16} & C_{26} & C_{36} & C_{46} & C_{56} & C_{66} \end{pmatrix} \begin{pmatrix} \varepsilon_{11} \\ \varepsilon_{22} \\ \varepsilon_{33} \\ \varepsilon_{23} \\ \varepsilon_{13} \\ \varepsilon_{12} \end{pmatrix}, \tag{7.14}$$

where $\sigma_{ij}$ and $\varepsilon_{ij}$ are the stress and strain component, respectively, $C_{ij}$ is the stiffness matrix. The quality factor $Q$ is an intrinsic property of the subsurface media, and it is closely linked with the property of the material, so it is reasonable to assume that have an identical formation with the stiffness matrix $C_{ij}$ as

$$Q_{ij} = \begin{pmatrix} Q_{11} & Q_{12} & Q_{13} & Q_{14} & Q_{15} & Q_{16} \\ Q_{12} & Q_{22} & Q_{23} & Q_{24} & Q_{25} & Q_{26} \\ Q_{13} & Q_{23} & Q_{33} & Q_{34} & Q_{35} & Q_{36} \\ Q_{14} & Q_{24} & Q_{34} & Q_{44} & Q_{45} & Q_{46} \\ Q_{15} & Q_{25} & Q_{35} & Q_{45} & Q_{55} & Q_{55} \\ Q_{16} & Q_{26} & Q_{36} & Q_{46} & Q_{56} & Q_{66} \end{pmatrix}. \tag{7.15}$$

Using the correspondence principle, the elastic modulus matrix $C_{ij}$ can be substituted by the viscoelastic modulus matrix $D_{ij}$, which results in the following stress-strain relation as

$$\begin{pmatrix} \sigma_{11} \\ \sigma_{22} \\ \sigma_{33} \\ \sigma_{23} \\ \sigma_{13} \\ \sigma_{12} \end{pmatrix} = \begin{pmatrix} D_{11} & D_{12} & D_{13} & D_{14} & D_{15} & D_{16} \\ D_{12} & D_{22} & D_{23} & D_{24} & D_{25} & D_{26} \\ D_{13} & D_{23} & D_{33} & D_{34} & D_{35} & D_{36} \\ D_{14} & D_{24} & D_{34} & D_{44} & D_{45} & D_{46} \\ D_{15} & D_{25} & D_{35} & D_{45} & D_{55} & D_{55} \\ D_{16} & D_{26} & D_{36} & D_{46} & D_{56} & D_{66} \end{pmatrix} \begin{pmatrix} \varepsilon_{11} \\ \varepsilon_{22} \\ \varepsilon_{33} \\ \varepsilon_{23} \\ \varepsilon_{13} \\ \varepsilon_{12} \end{pmatrix}, \tag{7.16}$$

where the fractional operator is

$$D_{ij} = C_{ij}\left(1 + \beta_{ij}\omega_0^{-\beta_{ij}} \frac{\partial^{\beta_{ij}}}{\partial t^{\beta_{ij}}}\right). \tag{7.17}$$

Considering the relationship between the fractional time derivatives and fractional spatial derivatives (Chapter 4), the viscoelastic matrix can be further written as

$$D_{ij} = C_{ij}\left(1 + \beta_{ij}\left(\frac{c_{ij,0}}{\omega_0}\right)^{\beta_{ij}} \cos\left(\frac{\pi\beta_{ij}}{2}\right)(-\nabla^2)^{\beta_{ij}/2} + \frac{\beta_{ij}}{c_{ij,0}}\left(\frac{c_{ij,0}}{\omega_0}\right)^{\beta_{ij}} \sin\left(\frac{\pi\beta_{ij}}{2}\right)(-\nabla^2)^{(\beta_{ij}-1)/2} \frac{\partial}{\partial t}\right). \tag{7.18}$$

For 2D modelling of P-SV waves in the *x-z* plane, the corresponding viscoelastic velocity can be defined as $c_{1,0} = \sqrt{C_{11}/\rho}$, $c_{2,0} = \sqrt{C_{33}/\rho}$ and $c_{S,0} = \sqrt{C_{55}/\rho}$, respectively. The stress-strain relation is derived from Eq. (7.16) as follows:

$$\begin{aligned} \sigma_{11} &= D_{11}(\varepsilon_{11} + \varepsilon_{33}) + (D_{13} - \tilde{D}_{11})\varepsilon_{33}, \\ \sigma_{33} &= D_{33}(\varepsilon_{11} + \varepsilon_{33}) + (D_{13} - \tilde{D}_{33})\varepsilon_{11}, \\ \sigma_{13} &= 2D_{55}\varepsilon_{13}, \end{aligned} \tag{7.19}$$

where the fractional spatial derivative operators are

$$D_{11} = C_{11}\left(1 + \beta_{11}\left(\frac{c_{1,0}}{\omega_0}\right)^{\beta_{11}} \cos\left(\frac{\pi\beta_{11}}{2}\right)(-\nabla^2)^{\beta_{11}/2} + \frac{\beta_{11}}{c_{1,0}}\left(\frac{c_{1,0}}{\omega_0}\right)^{\beta_{11}} \sin\left(\frac{\pi\beta_{11}}{2}\right)(-\nabla^2)^{(\beta_{11}-1)/2} \frac{\partial}{\partial t}\right), \tag{7.20a}$$

$$D_{13} = C_{13}\left(1 + \beta_{13}\left(\frac{c_{s,0}}{\omega_0}\right)^{\beta_{13}} \cos\left(\frac{\pi\beta_{13}}{2}\right)(-\nabla^2)^{\beta_{13}/2} + \frac{\beta_{13}}{c_{s,0}}\left(\frac{c_{s,0}}{\omega_0}\right)^{\beta_{11}} \sin\left(\frac{\pi\beta_{13}}{2}\right)(-\nabla^2)^{(\beta_{13}-1)/2} \frac{\partial}{\partial t}\right), \tag{7.20b}$$

$$D_{33}=C_{33}\left(1+\beta_{33}\left(\frac{c_{2,0}}{\omega_0}\right)^{\beta_{33}}\cos\left(\frac{\pi\beta_{33}}{2}\right)(-\nabla^2)^{\beta_{33}/2}+\frac{\beta_{33}}{c_{2,0}}\left(\frac{c_{2,0}}{\omega_0}\right)^{\beta_{33}}\sin\left(\frac{\pi\beta_{33}}{2}\right)(-\nabla^2)^{(\beta_{33}-1)/2}\frac{\partial}{\partial t}\right),\quad(7.20c)$$

$$D_{55}=C_{55}\left(1+\beta_{55}\left(\frac{c_{S,0}}{\omega_0}\right)^{\beta_{55}}\cos\left(\frac{\pi\beta_{55}}{2}\right)(-\nabla^2)^{\beta_{55}/2}+\frac{\beta_{55}}{c_{S,0}}\left(\frac{c_{S,0}}{\omega_0}\right)^{\beta_{55}}\sin\left(\frac{\pi\beta_{55}}{2}\right)(-\nabla^2)^{(\beta_{55}-1)/2}\frac{\partial}{\partial t}\right),\quad(7.20d)$$

and two corresponding fractional derivative operators are

$$\tilde{D}_{11}=C_{11}\left(1+\beta_{11}\left(\frac{c_{S,0}}{\omega_0}\right)^{\beta_{11}}\cos\left(\frac{\pi\beta_{11}}{2}\right)(-\nabla^2)^{\beta_{11}/2}+\frac{\beta_{11}}{c_{S,0}}\left(\frac{c_{S,0}}{\omega_0}\right)^{\beta_{11}}\sin\left(\frac{\pi\beta_{11}}{2}\right)(-\nabla^2)^{(\beta_{11}-1)/2}\frac{\partial}{\partial t}\right),\quad(7.20e)$$

$$\tilde{D}_{33}=C_{33}\left(1+\beta_{33}\left(\frac{c_{S,0}}{\omega_0}\right)^{\beta_{33}}\cos\left(\frac{\pi\beta_{33}}{2}\right)(-\nabla^2)^{\beta_{33}/2}+\frac{\beta_{33}}{c_{S,0}}\left(\frac{c_{S,0}}{\omega_0}\right)^{\beta_{33}}\sin\left(\frac{\pi\beta_{33}}{2}\right)(-\nabla^2)^{(\beta_{33}-1)/2}\frac{\partial}{\partial t}\right).\quad(7.20f)$$

The above stress-strain relation, combining the momentum conservation equation and velocity/displacement-strain relation, constitutes the full viscoelastic wave equation in anisotropic attenuating media. Using the Thomsen's notation of the anisotropic elastic media (Thomsen 1986), the coefficients in the stiffness matrix (7.16) are:

$$\begin{aligned}C_{33}&=\rho c_P^2(\beta_{33}),\\C_{55}&=\rho c_S^2(\beta_{55}),\\C_{11}&=(2\varepsilon+1)C_{33},\\C_{13}&=\sqrt{2\delta C_{33}(C_{33}-C_{55})+(C_{33}-C_{55})^2}-C_{55},\end{aligned}\quad(7.21)$$

where $\delta$ and $\varepsilon$ are Thomsen anisotropic parameters. For weak anisotropic media, Y. Zhu & Tsvankin (2006) proposed the relation of the element in the anisotropic $Q$ matrix (7.15) as:

$$\begin{aligned}Q_{33}&=Q_{P0},\\Q_{55}&=Q_{S0},\\Q_{11}&=Q_{33}/(\varepsilon_Q+1),\\\delta_Q&=4\frac{Q_{33}-Q_{55}}{Q_{55}}g+2\frac{Q_{33}-Q_{13}}{Q_{13}}(1+2\delta-2g),\end{aligned}\quad(7.22)$$

where $\delta_Q$ and $\varepsilon_Q$ are two parameters similar to Thomsen parameters to represent the $Q$ anisotropy, and $g=C_{55}/C_{33}$.

Figure 7.4 shows the wavefield snapshot in 0.3 s in an anisotropic model, with quality factors $Q_{P0} = 50$ and $Q_{S0} = 30$, with the respective velocities 3000 and 2000 m/s, and the reference frequency is 500 Hz. The Thomsen parameters are $\delta = 0.2$, $\varepsilon = 0.1$, $\delta_Q = 0.2$ and $\varepsilon_Q = 0.1$. The model is discretized into 500 × 500 grids with the spatial interval of 5 m and the time step of 0.5 ms. The wave travels much faster horizontally than vertically, which shows the correctness of the anisotropy. The comparison between the elastic and viscoelastic case shows clear delayed wavefront and reduced amplitude in the attenuating media.

Although the wave equations for anisotropic attenuating media are derived as above, these formulae are not yet verified with the analytical results due to the limited research time. As seismic wave simulation in anisotropy media requires additional Thomsen parameters, how to establish the appropriate anisotropic parameter models from seismic data is also a promising research topic.

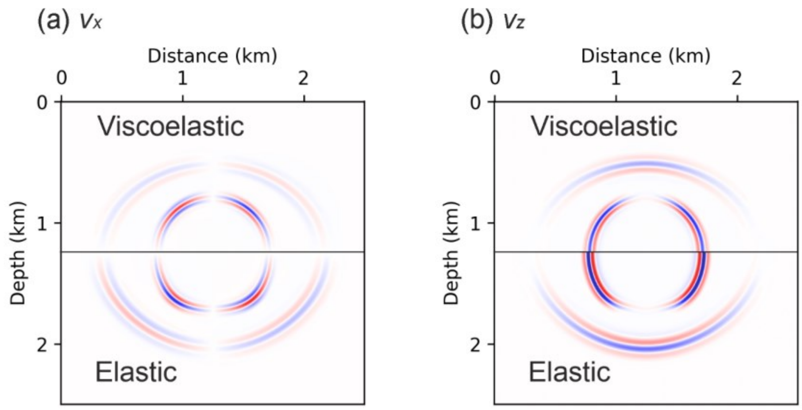


**Figure 7.4** Wavefields Snapshots at 0.3 s. (a) Horizontal component of particle velocity; (b) vertical component of particle velocity. The upper panel is the viscoelastic case, and the lower panel is the elastic case.

## 7.4 Suggestions for future work

This thesis focuses on the viscoelastic theory development and its implementation in reverse-time migration. Viscoelasticity is an intrinsic property of earth media, so the investigation of the viscoelastic theory will benefit a wide range of geophysical research and application. Expect for the ongoing future work mentioned above, many meaningful aspects are not involved due to the limited research time. Some potential future works are listed as follows.

1. In the seismic simulation, the top boundary generally is set to the straight and uniform grids. This setting is reasonable for marine seismic surveys as the variation of the water surface is trivial compared with geological structures. However, in land seismic surveys, especially in areas with strongly varying topography, this regular setting is no longer suitable, as the varying surface causes scattered waves and converted waves, leading to distorted seismic records. Therefore, how to solve the fractional spatial derivatives in irregular meshes is a practical topic.
2. In the implementation of reverse-time migration, I only consider the primary waves (compression waves) in this thesis. For land seismic data, the P-wave and S-wave decomposition should be conducted before the biaxial wavefield decomposition. The cross-correlation of the P wave and S wave will also produce artefacts. Currently, the decomposition of P and S wave depends on the divergence and curl of the wavefield. Efficient and effective P/S waves decomposition methods should be investigated when implementing the land seismic reverse-time migration.
3. The generalised viscoelastic model can also be applied to $Q$ analysis or other reservoir analysis, such as AVO analysis, in exploration geophysics.

# Appendix A: the analytical solution for the wave equation with fractional time derivative

For the wave equation formed with fractional time derivative (FTD), I consider a homogeneous case and derive its analytical solution. Considering the source term on the right-hand side of the wave equation, the generalised wave equation is written as:

$$c^2\nabla^2\left(1+\beta\tau^\beta\frac{\mathrm{d}^\beta}{\mathrm{d}t^\beta}\right)u-\frac{\partial^2 u}{\partial t^2}=-f(t)\delta(\mathbf{x}-\mathbf{x}_0)\,, \tag{A.1}$$

where $f(t)$ is a source term at position $\mathbf{x}_0$. In the frequency domain, Eq. (A.1) becomes a Helmholtz equation (Carcione 2014)

$$\left[\nabla^2+\Omega_1^2\omega^2\right]\hat{U}(\omega)=-\Omega_1^2\hat{f}(\omega)\delta(\mathbf{x}-\mathbf{x}_0)\,, \tag{A.2}$$

where $\hat{U}(\omega)$ is the wavefield in the frequency domain, and

$$\Omega_1=\frac{1}{c}\left(1+\beta\left(\frac{\mathrm{i}\omega}{\omega_0}\right)^\beta\right)^{-1/2}. \tag{A.3}$$

For 1D case, the above Helmholtz equation Eq. (A.3) has an analytical solution as

$$\hat{U}(\omega)=-\frac{\mathrm{i}e^{\mathrm{i}\omega\Omega_1\|\mathbf{x}-\mathbf{x}_0\|}}{2\omega}\Omega_1\hat{f}(\omega)\,, \tag{A.4}$$

and for 2D case, the solution is:

$$\hat{U}(\omega)=-\mathrm{i}\frac{\Omega_1^2}{4}H_0^{(2)}\left(\omega\Omega_1\|\mathbf{x}-\mathbf{x}_0\|\right)\hat{f}(\omega) \tag{A.5}$$

where $H_0^{(2)}$ denotes the zero-order Hankel function of the second kind. The solution for FTD in time domain can be obtained by applying the inverse Fourier transform to Eqs. (A.4) or (A.5).

# Appendix B: the analytical solution for the wave equation with fractional spatial derivatives

For the equation with fractional spatial derivatives (FSD), I apply Green's function method to obtain the analytical solution. Here, I only consider 1D case where the wavenumber is a scalar.

In the wavenumber domain, the generalised wave equation with FSD becomes:

$$\frac{\partial^2 U(t,k)}{\partial t^2} + c^2 k^{1+\beta} C_2 \frac{\partial U(t,k)}{\partial t} + c^2 \left(k^2 + k^{2+\beta} C_1\right) U(t,k) = 0 \,, \tag{B.1}$$

where $U(t,k)$ is the wavefield in the wavenumber domain.

Setting a unit force at time $\tau$, and rewrite Eq. (B.1) as (Constanda 2018):

$$\frac{\partial^2 G(t,k;\tau)}{\partial t^2} + c^2 k^{1+\beta} C_2 \frac{\partial G(t,k;\tau)}{\partial t} + c^2 \left(k^2 + k^{2+\beta} C_1\right) G(t,k;\tau) = \delta(t-\tau) \,, \tag{B.2}$$

where $G(t,k;\tau)$ is the Green's function. When $t > \tau$, Eq. (B.2) is a homogeneous partial differential equation as

$$\frac{\partial^2 G(t,k;\tau)}{\partial t^2} + c^2 k^{1+\beta} C_2 \frac{\partial G(t,k;\tau)}{\partial t} + c^2 \left(k^2 + k^{2+\beta} C_1\right) G(t,k;\tau) = 0 \,, \tag{B.3}$$

and the solution is

$$G(t,k;\tau) = e^{-c^2 k^{1+\beta} C_2 (t-\tau)/2} \left\{ D_1 \cos[\Omega_2 (t-\tau)] + D_2 \sin[\Omega_2 (t-\tau)] \right\} , \tag{B.4}$$

where

$$\Omega_2 = \frac{ck}{2} \sqrt{4 + 4k^\beta C_1 - c^2 k^{2\beta} C_2^2} \,. \tag{B.5}$$

When $t < \tau$, $G(t,k;\tau) = 0$. Considering the continuity of $G(t,k;\tau)$ at $t = \tau$, Eq. (B.4) leads to

$D_1 = 0$. Therefore, the Green' function may be expressed as

$$G(t,k;\tau) = H(t-\tau) D_2 e^{-c^2 k^{1+\beta} C_2 (t-\tau)/2} \sin[\Omega_2 (t-\tau)] \tag{B.6}$$

where $H(\bullet)$ is the Heaviside step function. To determine $D_2$, Eq. (B.6) can be integrated with respect to *t* over an interval $[t_1, t_2]$, where $0 \le t_1 < \tau < t_2$, as following

$$G_t(t,k;\tau)\Big|_{t_1}^{t_2} + c^2 k^{1+\beta} C_2 \, G(t,k;\tau)\Big|_{t_1}^{t_2} + \left(c^2 k^2 + c^2 k^{2+\beta} C_1\right) \int_{t_1}^{t_2} G \mathrm{d}t = 1, \tag{B.7}$$

where $G_t(t,k;\tau)$ is the first time derivative of the Green's function. In Eq. (B.7), $G(t_1,k;\tau) = 0$, $G_t(t_1,k;\tau) = 0$, and

$$\begin{aligned} G(t_2,k;\tau) &= D_2 e^{-c^2 k^{1+\beta} C_2 (t_2-\tau)/2} \sin[\Omega_2 (t_2-\tau)], \\ G_t(t_2,k;\tau) &= D_2 e^{-c^2 k^{1+\beta} C_2 (t_2-\tau)/2} \left( \frac{-c^2 k^{1+\beta} C_2}{2} \sin[\Omega_2 (t_2-\tau)] + \Omega_2 \cos[\Omega_2 (t_2-\tau)] \right). \end{aligned} \tag{B.8}$$

Let $t_1, t_2 \to \tau$, according to the continuity of *G* at $t = \tau$, it follows that

$$\lim_{\substack{t_1 \to \tau \\ t_2 \to \tau}} \int_{t_1}^{t_2} G \mathrm{d}t = 0. \tag{B.9}$$

Substituting these quantities into Eq. (B.7), the coefficient $D_2 = 1/\Omega_2$. Hence, the green function can be written as:

$$G(t,k;\tau) = H(t-\tau) \frac{\sin\left[\Omega_2 \left(t-\tau\right)\right]}{\Omega_2} e^{-\frac{c^2 k^{1+\beta} C_2 (t-\tau)}{2}}. \tag{B.10}$$

Considering the source signature $f(t)$, the analytical solution in time-wavenumber domain is

$$U(k,t) = \int_0^t G(k,t,\tau) f(\tau) \mathrm{d}\tau \, . \tag{B.11}$$

Performing inverse Fourier transform of $U(k,t)$, the analytical solution for FSD in the time-space domain can be obtained.

# Appendix C: stability analysis of wave equation with fractional spatial derivatives

The stability condition for the FSD can be derived by transferring Eq. (4.6) into wavenumber domain and using central finite difference method to approximate the second-order time derivative. The relation between forward pressure field $u^{n+1}$, current stress field $u^n$ and the previous stress field $u^{n-1}$ may be expressed as

$$\frac{u^{n+1}-2u^n+u^{n-1}}{\Delta t^2}=-c^2k^2u^n-c^2C_1k^{\beta+2}u^n-c^2C_2k^{\beta+1}\frac{u^n-u^{n-1}}{\Delta t}. \tag{C.1}$$

where $n$ is the step index. Eq. (C.1) may be expressed in a matrix form:

$$\begin{bmatrix} u^{n+1} \\ u^n \end{bmatrix}=\begin{bmatrix} 2+D_1\Delta t^2+D_2\Delta t & -1-D_2\Delta t \\ 1 & 0 \end{bmatrix}\begin{bmatrix} u^n \\ u^{n-1} \end{bmatrix}, \tag{C.2}$$

where $D_1=-c^2k^2-c^2C_1k^{\beta+2}$ , $D_2=-c^2C_2k^{\beta+1}$ . According to the eigenvalue theory, the absolute value of the eigenvalue of coefficient matrix (the square matrix of the right-hand side) should be no larger than 1 (Gazdag 1981, Zhu & Harris 2014). Therefore, the following condition can be obtained:

$$\Delta t\le\left|\frac{D_2+\sqrt{-2D_1}}{D_1}\right|, \tag{C.3}$$

Substitute $D_1$, $D_2$ into Eq. (C.3), the above condition becomes

$$\Delta t\le\left|\frac{-c^2C_2k^{\beta+1}}{c^2k^2+c^2C_1k^{\beta+2}}+\frac{\sqrt{2}}{\sqrt{c^2k^2+c^2C_1k^{\beta+2}}}\right|, \tag{C.4}$$

To guarantee the stability for all frequency waves, the wavenumber may be set as $k = k_{\mathrm{Ny}} = \pi / \Delta h$, where $k_{\mathrm{Ny}}$ is the Nyquist spatial wavenumber, and $\Delta h = \min\left(\Delta x, \Delta z\right)$ is the minimum spatial grid interval. For purely acoustic case, $\beta = 0$, $C_1$ and $C_2$ become zero and $c$ becomes pure acoustic velocity $c_0$, so condition (C.4) becomes the stability condition of acoustic wave equation (Gazdag 1981):

$$\Delta t \leq \frac{\sqrt{2}\Delta h}{\pi c_0} \quad . \tag{C.5}$$

This stability condition for proposed viscoelastic wave Eq. (C.4) is slightly stricter than condition (C.5), which demonstrates that the attenuation effect brings the constraint to stability condition.

# Reference

Adam, L., Batzle, M., Lewallen, K.T. & Wijk, K. van. (2009) Seismic wave attenuation in carbonates. *J. Geophys. Res*., **114**, B06208. doi:10.1029/2008JB005890.

Aki, K. & Richards, P.G. (1980) *Quantitative Seismology, Theory and Methods*. Freeman, San Francisco: University Science Books.

Baysal, E., Kosloff, D.D. & Sherwood, J.W.C. (1983) Reverse time migration. *Geophysics*, **48**, 1514–1524. doi:10.1190/1.1441434.

Borgomano, J.V.M., Pimienta, L., Fortin, J. & Guéguen, Y. (2017) Dispersion and attenuation measurements of the elastic moduli of a dual-porosity limestone. *J. Geophys. Res. Solid Earth*, **122**, 2690–2711. doi:10.1002/2016JB013816.

Caputo, M. (1967) Linear Models of Dissipation whose Q is almost Frequency Independent--II. *Geophys. J. Int*., **13**, 529–539. doi:10.1111/j.1365-246X.1967.tb02303.x.

Carcione, J.M., Cavallini, F., Mainardi, F. & Hanyga, A. (2002) Time-domain modeling of constant- q seismic waves using fractional derivatives. *Pure Appl. Geophys*., **159**, 1719–1736. doi:10.1007/s00024-002-8705-z.

Carcione, J.M. (2009) Theory and modeling of constant- Q P- and S-waves using fractional time derivatives. *Geophysics*, **74**, T1–T11. doi:10.1190/1.3008548.

Carcione, J.M. (2010) A generalization of the Fourier pseudospectral method. *Geophysics*, **75**, A53–A56. doi:10.1190/1.3509472.

Carcione, J.M. (2014) *Wave Fields in Real Media: Wave Propagation in Anisotropic, Anelastic, Porous and Electromagnetic Media*: Third Edition. doi:10.1016/C2013-0-18893-9.

Chen, H., Zhou, H., Li, Q. & Wang, Y. (2016) Two efficient modeling schemes for fractional Laplacian viscoacoustic wave equation. *Geophysics*, **81**, T233–T249. doi:10.1190/geo2015-0660.1.

Chen, W. & Holm, S. (2004) Fractional Laplacian time-space models for linear and nonlinear lossy media exhibiting arbitrary frequency power-law dependency. *J. Acoust. Soc. Am.*, **115**, 1424–1430. doi:10.1121/1.1646399.

Claerbout, J.F. (1971) Toward a unified theory of reflector mapping. *Geophysics*, **36**, 467–481. doi:10.1190/1.1440185.

Cole, K.S. & Cole, R.H. (1941) Dispersion and absorption in dielectrics i. alternating current characteristics. *J. Chem. Phys*., **9**, 341–351. doi:10.1063/1.1750906.

Constanda, C. (2018) *Solution Techniques for Elementary Partial Differential Equations*: Third edition. CRC Press, doi:10.1201/9781315381442.

Dutta, G. & Schuster, G.T. (2014) Attenuation compensation for least-squares reverse time migration using the viscoacoustic-wave equation. *Geophysics*, **79**, S251–S262. doi:10.1190/geo2013-0414.1.

Emmerich, H. & Korn, M. (1987) Incorporation of attenuation into time - domain computations of seismic wave fields. *Geophysics*, **52**, 1252 – 1264. doi:10.1190/1.1442386.

Fei, T.W., Luo, Y., Yang, J., Liu, H. & Qin, F. (2015) Removing false images in reverse time migration: The concept of de-primary. *Geophysics*, **80**, S237–S244. doi:10.1190/geo2015-0289.1.

Fichtner, A. & Driel, M. van. (2014) Models and Fréchet kernels for frequency-(in)dependent Q. *Geophys. J. Int.*, **198**, 1878–1889. doi:10.1093/gji/ggu228.

Fletcher, R.P., Fowler, P.J., Kitchenside, P. & Albertin, U. (2006) Suppressing unwanted internal reflections in prestack reverse-time migration. *Geophysics*, **71**, E79–E82. doi:10.1190/1.2356319.

Futterman, W.I. (1962) Dispersive body waves. *J. Geophys. Res.*, **67**, 5279–5291. doi:10.1029/JZ067i013p05279.

Gazdag, J. (1981) Modeling of the acoustic wave equation with transform methods. *Geophysics*, **46**, 854–859. doi:10.1190/1.1441223.

Gradshteyn, I.S. & Ryzhik, I.M. (2000) *Table of Integrals, Series, and Products. Math. Comput.,* 6th ed., Academic Press, New York.

Gray, M., Bell, R.E., Morgan, J. V., Henrys, S. & Barker, D.H.N. (2019) Imaging the shallow subsurface structure of the north hikurangi subduction zone, new zealand, using 2‐d full‐waveform inversion. *J. Geophys. Res. Solid Earth*, **124**, 9049–9074. doi:10.1029/2019JB017793

Guitton, A., Kaelin, B. & Biondi, B. (2007) Least-squares attenuation of reverse-time-migration artifacts. *Geophysics*, **72**, S19–S23. doi:10.1190/1.2399367.

Hu, L. & McMechan, G.A. (1987) Wave‐field transformations of vertical seismic profiles. *Geophysics*, **52**, 307–321. doi:10.1190/1.1442305.

Kailath, T., Sayed, A.H. & Hassibi, B. (2000*) Linear estimation. Geostatistics Pet. Geol*., Prentice Hall.

Kim, J., Kim, K.-Y. & Kim, J. (2019) Generalized Poynting vector model to calculate the spatial and spectral profiles of the electric field intensity, optical power flow, and optical absorption for all optical modes of organic light-emitting diodes. *Opt. Express*, **27**, A1261. doi:10.1364/OE.27.0A1261.

Kjartansson, E. (1979) Constant Q -wave propagation and attenuation. *J. Geophys. Res*., **84**, 4737. doi:10.1029/JB084iB09p04737.

Kolsky, H. (1953) *Stress waves in solids.* Clarendon Press, Oxford.

Komatitsch, D. & Martin, R. (2007) An unsplit convolutional perfectly matched layer improved at grazing incidence for the seismic wave equation. *Geophysics*, **72**, SM155–SM167. doi:10.1190/1.2757586.

Liu, F., Zhang, G., Morton, S.A. & Leveille, J.P. (2011) An effective imaging condition for reverse-time migration using wavefield decomposition. *Geophysics*, **76**, S29–S39. doi:10.1190/1.3533914.

Liu, H.P., Anderson, D.L. & Kanamori, H. (1976) Velocity dispersion due to anelasticity; implications for seismology and mantle composition. *Geophys. J. Int*., **47**, 41–58. doi:10.1111/j.1365-246X.1976.tb01261.x.

Liu, X. & Greenhalgh, S. (2019) Fitting viscoelastic mechanical models to seismic attenuation and velocity dispersion observations and applications to full waveform modelling. *Geophys. J. Int*., **219**, 1741–1756. doi:10.1093/gji/ggz395.

Lu, J.F. & Hanyga, A. (2004) Numerical modelling method for wave propagation in a linear viscoelastic medium with singular memory. *Geophys. J. Int*., **159**, 688–702. doi:10.1111/j.1365-246X.2004.02409.x.

Mason, W.P. (1956) Physical acoustics and the properties of solids. *J. Acoust. Soc. Am*., **28**, 1197–1206. doi:10.1121/1.1908593.

Matheney, M.P. & Nowack, R.L. (1995) Seismic attenuation values obtained from instantaneous-frequency matching and spectral ratios. *Geophys. J. Int*., **123**, 1–15. doi:10.1111/j.1365-246X.1995.tb06658.x.

Mavko, G., Mukerji, T., & Dvorkin, J.P. (1998) *The Rock Physics Handbook: Tools for Seismic Analysis of Porous Media*. Cambridge University Press, Cambridge. doi:10.1017/9781108333016.

McDonal, F.J., Angona, F.A., Mills, R.L., Sengbush, R.L., Nostrand, R.G. Van & White, J.E. (1958) Attenuation of shear and compressional waves in pierre shale. *Geophysics*, **23**, 421–439. doi:10.1190/1.1438489.

McMechan, G.A. (1983) Migration by extrapolation of time-dependent boundary values. *Geophys. Prospect.*, **31**, 413–420. doi:10.1111/j.1365-2478.1983.tb01060.x.

Mittet, R., Sollie, R. & Hokstad, K. (1995) Prestack depth migration with compensation for absorption and dispersion. *Geophysics*, **60**, 1485–1494. doi:10.1190/1.1443882.

Moczo, P. (2005) On the rheological models used for time-domain methods of seismic wave propagation. *Geophys. Res. Lett.*, **32**, L01306. doi:10.1029/2004GL021598.

Moczo, P., Jozef, K. & Martin, G. (2014) *The Finite-Difference Modelling of Earthquake Motions: Waves and Ruptures*, Cambridge University Press, Cambridge.

Molyneux, J.B. & Schmitt, D.R. (2000) Compressional-wave velocities in attenuating media: A laboratory physical model study. *Geophysics*, **65**, 1162–1167. doi:10.1190/1.1444809.

Morozov, I.B., Deng, W. & Cao, D. (2020) Mechanical analysis of viscoelastic models for Earth media. *Geophys. J. Int.,* **220**, 1762–1773. doi:10.1093/gji/ggz445.

Mu, X., Huang, J., Yang, J., Li, Z. & Ssewannyaga Ivan, M. (2022) Viscoelastic wave propagation simulation using new spatial variable-order fractional Laplacians. *Bull. Seismol. Soc. Am.*, **112**, 48–77. doi:10.1785/0120210099.

Ning, C. (2016) Seismic wavefield modelling and application in viscoelastic media. PhD thesis, Imperial College London, London. doi: doi.org/10.25560/46160.

Ning, C. & Wang, Y. (2016) Reverse-time migration with spatially variable Q. *78th EAGE Conf. Exhib.* 2016. 1–5, European Association of Geoscientists & Engineers. doi:10.3997/2214-4609.201601211.

Operto, S., Virieux, J., Amestoy, P., L'Excellent, J.-Y., Giraud, L. & Ali, H.B.H. (2007) 3D finite-difference frequency-domain modeling of visco-acoustic wave propagation using a massively parallel direct solver: A feasibility study. *Geophysics*, **72**, SM195–SM211. doi:10.1190/1.2759835.

Podlubny, I. (1999) *Fractional differential equations: an introduction to fractional derivatives, fractional differential equations, to methods of their solution and some of their applications*. Academic press, New York.

Qiao, Z., Sun, C. & Wu, D. (2019) Theory and modelling of constant- Q viscoelastic anisotropic media using fractional derivative. *Geophys. J. Int.,* **217**, 798–815. doi:10.1093/gji/ggz050.

Revelo, D.E. & Pestana, R.C. (2019) Up/down acoustic wavefield decomposition using a single propagation and its application in reverse time migration. *Geophysics*, **84**, S341–S353. doi:10.1190/geo2018-0305.1.

Sams, M.S., Neep, J.P., Worthington, M.H. & King, M.S. (1997) The measurement of velocity dispersion and frequency - dependent intrinsic attenuation in sedimentary rocks. *Geophysics*, **62**, 1456–1464. doi:10.1190/1.1444249.

Shen, P. & Albertin, U. (2015) Up-down separation using Hilbert transformed source for causal imaging condition. *SEG Tech. Progr. Expand. Abstr.* 2015, 4175–4179. doi:10.1190/segam2015-5862960.1.

Sun, J., Zhu, T. & Fomel, S. (2015) Viscoacoustic modeling and imaging using low-rank approximation. *Geophysics*, **80**, A103–A108. doi:10.1190/geo2015-0083.1.

Tarantola, A. (1988) Theoretical background for the inversion of seismic waveforms including elasticity and attenuation. *Pure Appl. Geophys*., 128, 365–399. doi:10.1007/BF01772605

Thomsen, L. (1986) Weak elastic anisotropy. *Geophysics*, **51**, 1954–1966. doi:10.1190/1.1442051.

Treeby, B.E. & Cox, B.T. (2010) Modeling power law absorption and dispersion for acoustic propagation using the fractional Laplacian. *J. Acoust. Soc. Am*., **127**, 2741–2748. doi:10.1121/1.3377056.

Vasilyeva, M., Basabe, J.D. De, Efendiev, Y. & Gibson, R.L. (2019) Multiscale model reduction of the wave propagation problem in viscoelastic fractured media. *Geophys. J. Int.*, **217**, 558–571. doi:10.1093/gji/ggz043.

Wang, W., McMechan, G.A. & Xie, F. (2016) Analysis of up/down decomposed acoustic reverse time migration images. *Geophysics*, **81**, S253–S259. doi:10.1190/geo2015-0612.1.

Wang, Y. (2004) Q analysis on reflection seismic data. *Geophys. Res. Lett*., **31**(17). doi:10.1029/2004GL020572.

Wang, Y. (2008a) *Seismic inversion.* Wiley-Blackwell Press, Oxford. ISBN: 978-1-1192-5789-0.

Wang, Y. (2008b) *Seismic inverse Q filtering.* Wiley-Blackwell Press, Oxford. ISBN: 978-1-4051-8540-0.

Wang, Y. (2015) Frequencies of the Ricker wavelet. *Geophysics*, **80**, A31–A37. doi:10.1190/geo2014-0441.1.

Wang, Y. (2016) Generalized viscoelastic wave equation. *Geophys. J. Int*., **204**, 1216–1221. doi:10.1093/gji/ggv514.

Wang, Y. (2019) A constant-Q model for general viscoelastic media. *Geophys. J. Int*., **219**, 1562–1567. doi:10.1093/gji/ggz387.

Wang, Y. (2022) *Time-frequency analysis of seismic signals.* Wiley Press, Chichester. ISBN: 978-1-119-89234-2.

Wang, Y. & Guo, J. (2004a) Seismic migration with inverse Q filtering. *Geophys. Res. Lett.*, 31. doi:10.1029/2004GL020525.

Wang, Y. & Guo, J. (2004b) Modified Kolsky model for seismic attenuation and dispersion. *J. Geophys. Eng.*, **1**, 187–196. doi:10.1088/1742-2132/1/3/003.

Wang, Y. & Rao, Y. (2009) Reflection seismic waveform tomography. *J. Geophys. Res.*, **114**, B03304. doi:10.1029/2008JB005916.

Wang, Y., Zhou, H., Chen, H., & Chen, Y. (2018). Adaptive stabilization for Q-compensated reverse time migration. *Geophysics*, **83**(1), S15-S32. doi: 10.1190/GEO2017-0244.1.

Xing, G. & Zhu, T. (2018) Fractal mechanical network based time domain viscoacoustic wave equation. *SEG Tech. Progr. Expand. Abstr. 2018*, 3994–3998, doi:10.1190/segam2018-2995782.1.

Xing, G. & Zhu, T. (2019) Modeling frequency-independent Q viscoacoustic wave propagation in heterogeneous media. *J. Geophys. Res. Solid Earth*, **124**, 11568–11584. doi:10.1029/2019JB017985.

Xu, Q. & Wang, Y. (2022) Spatial filter for the pseudo-spectral implementation of fractional derivative wave equation. *Pure Appl. Geophys*. **179**, 2831–2840. doi:10.1007/s00024-022-03083-z.

Xu, Q. & Wang, Y. (2023) Determination of the viscoelastic parameters for the generalized viscoelastic wave equation. *Geophys. J. Int*., **233**(2), 875–884. doi: 10.1093/gji/ggac488.

Yao, J., Zhu, T., Hussain, F. & Kouri, D.J. (2017) Locally solving fractional Laplacian viscoacoustic wave equation using Hermite distributed approximating functional method. *Geophysics*, **82**, T59–T67. doi:10.1190/geo2016-0269.1.

Yoon, K. & Marfurt, K.J. (2006) Reverse-time migration using the Poynting vector. *Explor. Geophys.*, **37**, 102–107. doi:10.1071/EG06102.

Zener, C.M. (1948) *Elasticity and Anelasticity of Metals*. Univ. Chicago Press.

Zhang, Q. (2014) RTM angle gathers and Specular Filter (SF) RTM using optical flow. *SEG Tech. Progr. Expand. Abstr. 2014*, 3816–3820, doi:10.1190/segam2014-0792.1.

Zhang, Y. & Sun, J. (2009) Practical issues of reverse time migration: True amplitude gathers, noise removal and harmonic-source encoding. *Beijing 2009 Int. Geophys. Conf. Expo.*, 204–204. doi:10.1190/1.3603729.

Zhu, T. (2014) Time-reverse modelling of acoustic wave propagation in attenuating media. *Geophys. J. Int.*, **197**, 483–494. doi:10.1093/gji/ggt519.

Zhu, T. (2016) Implementation aspects of attenuation compensation in reverse-time migration. *Geophys. Prospect.*, **64**, 657–670. doi:10.1111/1365-2478.12301.

Zhu, T. (2017) Numerical simulation of seismic wave propagation in viscoelastic-anisotropic media using frequency-independent Q wave equation. *Geophysics*, **82**, WA1–WA10. doi:10.1190/geo2016-0635.1.

Zhu, T. & Bai, T. (2019) Efficient modeling of wave propagation in a vertical transversely isotropic attenuative medium based on fractional Laplacian. *Geophysics*, **84**, T121–T131. doi:10.1190/geo2018-0538.1.

Zhu, T. & Carcione, J.M. (2014) Theory and modelling of constant-Q P- and S-waves using fractional spatial derivatives. *Geophys. J. Int.*, **196**, 1787–1795. doi:10.1093/gji/ggt483.

Zhu, T., Carcione, J.M. & Harris, J.M. (2013) Approximating constant- Q seismic propagation in the time domain. *Geophys. Prospect.*, **61**, 931–940. doi:10.1111/1365-2478.12044.

Zhu, T. & Harris, J.M. (2014) Modeling acoustic wave propagation in heterogeneous attenuating media using decoupled fractional Laplacians. *Geophysics*, **79**, T105–T116. doi:10.1190/geo2013-0245.1.

Zhu, Y. & Tsvankin, I. (2006) Plane-wave propagation in attenuative transversely isotropic media. *Geophysics*, **71**, T17–T30. doi:10.1190/1.2187792.

# Publications

## Journal Papers

1. Xu, Q. & Wang, Y. (2022) Spatial Filter for the Pseudo-spectral Implementation of Fractional Derivative Wave Equation. *Pure Appl. Geophys*. **179**, 2831–2840. doi:10.1007/s00024-022-03083-z.
2. Xu, Q. & Wang, Y. (2023) Determination of the viscoelastic parameters for the generalized viscoelastic wave equation. *Geophys. J. Int*., **233**(2), 875–884. doi: 10.1093/gji/ggac488.
3. Xu, Q. & Wang, Y. (2023) Seismic reverse-time migration based on biaxial wavefield decomposition. *Geophysics*, under review.

## Conference papers

1. Xu, Q. & Wang, Y. (2022). Seismic wave simulation using a fractional spatial derivative equation: Fourier transform implementation with spatial correction function, 83rd EAGE Conference & Exhibition 2022.
2. Xu, Q. & Wang, Y. (2021). Seismic wave simulation using generalized viscoelastic wave equation, 82nd EAGE Conference & Exhibition 2021.